UNIVERSITY OF CALIFORNIA, SAN DIEGO

The Dynamics of Entangled DNA Networks using Single-Molecule Methods

A Dissertation submitted in partial satisfaction of the
requirements for the degree Doctor of Philosophy

in

Physics

by

Cole David Chapman

Committee in charge:

Professor Douglas E. Smith, Chair
Professor Gaurav Arya
Professor Michael Gilson
Professor Alex Groisman
Professor Rae M. Robertson-Anderson
Professor Oleg Shpyrko

2015

The Dissertation of Cole David Chapman is approved, and it is acceptable in quality and form for publication on microfilm and electronically:

_____

_____

_____

_____

_____

_____

Chair

University of California, San Diego

2015

TABLE OF CONTENTS

Signature Page……. iii

Table of Contents……. iv

List of Figures…….. v

Acknowledgments…… viii

Vita…….. x

Abstract of the Dissertation…….…… xi

Chapter 1 Polymers, Single-Molecule Studies……... 1

Chapter 2 Rheology and Microrheology …… 11

Chapter 3 Complex Effects of Molecular Topology on Diffusion in Entangled Biopolymer Blends…….. 19

Chapter 4 Crowding Induces Complex Ergodic Diffusion and Dynamic Elongation of Large DNA Molecules…….. 38

Chapter 5 Onset of Non-Continuum Effects in Microrheology of Entangled Polymer Solutions……..…….. 66

Chapter 6 Nonlinear Microrheology Reveals Entanglement-driven Molecular-level Viscoelasticity of Concentrated DNA……. 86

Chapter 7 Conclusions, Future Work…….. 102

References ……... 107

LIST OF FIGURES

Figure 1.1 The Gaussian chain model, where a polymer is composed of N rigid rods of length b. The random orientation of the joints results in an approximately spherical coil, of radius R_g…….. 2

Figure 1.2 (a.) A polymer entangled in a concentrated network of surrounding polymers. (b.) The surrounding polymers may be modeled as simple obstacles, restricting the polymer to a tube-like region, along which the polymer may reptate…… 5

Figure 1.3 A 115 kbp DNA molecule, labeled with YOYO-1 dye…… 8

Figure 2.1 Active microrheology schematic. An embedded microsphere is captured and oscillated sinusoidally at a fixed frequency and amplitude. The displacement of the microsphere from trap center is used to calculate the force felt by the microsphere……. 14

Figure 2.2 Schematic for dual-force optical tweezers setup with epi-fluorescence microscopy……. 16

Figure 3.1 Schematic of experimental parameter space probed for ring-linear DNA blends. To track the center-of-mass motion of single linear molecules (to determine D_L) in ring-linear blends, a trace amount of fluorescent-labeled (green) linear tracer chains are embedded in entangled solutions of ring……... 25

Figure 3.2 Measured self-diffusion coefficients vs. fraction of linear DNA (f_L) in ring-linear blends. Self-diffusion coefficients for ring (blue) and linear (red) DNA in ring-linear blends at three overall solution concentrations, 0.1 mg/ml (triangles), 0.5 mg/ml (circles), and 1.0 mg/ml (squares)…… 28

Figure 3.3 Comparison between experiment and simulation results for self-diffusion coefficients vs. linear fraction f_L in ring-linear blends. Experiment (solid lines) and simulation (dashed lines) results are normalized by $D_L^* = D_L(f_L = 1, c = 1 \text{ mg/ml}) = D_L(f_L = 1, f = 0.5)$. Symbols and colors……..…….. 30

Figure 3.4 The decorrelation of the end-to-end vector of the linear chains at $f = 0.5$ for different f_L values (specified in the legend). The relaxation of the end-to-end vector initially slows down as f_L increases from 0.10 to 0.50, and then accelerates as f_L increases from 0.50 to 1.00. These non-monotonic…..… 32

Figure 3.5 The solution of equations (1) and (2) (see text) for $\tau_L(f_L)$ (red) and $\tau_R(f_L)$ (blue), for the 45-kbp, 1 mg/ml case with $c_1 = 0.008$, and $c_2 = 0.012$, exhibits non-monotonic variation in $\tau_L(f_L)$…….. 35

Figure 4.1 Mean squared displacements vs. time for both the 11 kbp (top) and 115 kbp (bottom) DNA diffusing in both 10 kDa (Sd) and 500 kDa (Ld) dextran from (A) 0-10 seconds and (B) 10-50 seconds. The concentration, C, and crowder size (Sd or Ld) for each MSD is indicated in the legend…… 45

Figure 4.2 Non-Gaussianity parameter, G vs. time for 11 kbp (purple) and 115 kbp (orange) DNA diffusing in 10 kDa (open squares) and 500 kDa (closed squares) dextran. Note G tends to zero (dashed line), indicating an ergodic diffusion process. Inset shows calculated ergodicity-breaking……..... 47

Figure 4.3 (A) Normalized DNA diffusion coefficients, D/D_0, and inverse normalized dextran solution viscosities, h_0/h, vs. dextran concentration C for DNA diffusing in dextran solutions. Color and symbol scheme is as in Figure 4.2, with inverse viscosity shown in gray. The reduction in D…… 50

Figure 4.4 Probability distributions for elongation parameter E for 11 kbp DNA in 500 kDa dextran (top), 115 kbp DNA in 10 kDa dextran (middle), and 115 kbp DNA in 500 kDa dextran (bottom). Distributions for C = 0 (black), 10 (green), 20 (blue), 30 (orange), and 40 (red) are shown…… 54

Figure 4.5 (A) Measured major axis, R_{max}, (white line) and minor axis, R_{min}, (black line) for a typical 115 kbp DNA molecule diffusing in Ld (C = 20) with increasing time. The fluctuation length for the displayed molecule, L_i, is noted for each frame. (B) Ensemble averaged fluctuation length, L, vs. time…….. 57

Figure 4.6 Normalized R_{max} autocorrelation ($<R_{max}(0)R_{max}(t)>/(R_{max}(0))^2$ vs. time for 11 kbp (top) and 115 kbp (bottom) DNA. Color scheme is the same as in Figures 4.4 and 6.5. Autocorrelation data for all cases were well fit to an exponential decay, with the corresponding decay rates, b…….. 58

Figure 4.7 Dextran viscosity, η, vs oscillation frequency, w, for concentrations C = 0 - 40 for (A) Sd and (B) Ld. Color scheme is the same as in Figure 4, with the additional pink squares representing C = 35. Viscosity values are measured via optical tweezers oscillatory microrheology as described in…….. 59

Figure 5.1 Measured force on a 1 μm radius microsphere (red; left axis) during $\omega = 12.57$ rad s^{-1} stage oscillation (black; right axis). The blue curve is the fit to the raw force data (described in methods). The three panels show measurements in solutions of 3 different DNA lengths…….. 73

Figure 5.2 $G'(\omega)$ (closed symbols) and $G''(\omega)$ (open symbols) for 11, 45, and 115 kbp DNA measured with microspheres of radii: 1 μm (red squares), 2.25 μm (blue circles), and 3 μm (black triangles). Theoretically predicted scaling trends for the terminal regime ($G'(\omega) \sim \omega^2$, $G''(\omega) \sim \omega$)…… 74

Figure 5.3 Complex viscosity, $h^*(\omega)$, measured with microspheres of radii 1 μm (red squares), 2.25 μm (blue circles), and 3 μm (black triangles) for each molecular length. Theoretically predicted scaling trends for semi-dilute ($h^*(\omega) \sim \omega^{-0.5}$) and fully entangled ($h^*(\omega) \sim \omega^{-1}$) solutions……..... 75

Figure 5.4 $G'(\omega)$ (closed symbols) and $G''(\omega)$ (open symbols) for 3 μm radius microspheres. Values for 11 kbp (magenta), 45 kbp (green), and 115 kbp (orange) DNA are shown……. 76

Figure 5.5 Polymer disengagement time (τ_d) vs. bead radius (R) for 45 kbp DNA at 1.0 mg/ml. Disengagement times for each bead size (black squares) are determined from the measured crossover frequency for each bead size as described in the text. The data is fit to a power law $\tau_d \sim R^{3.16\pm0.06}$ (red line)….. 79

Figure 6.1 Experiment schematic. Trap position (blue) and probe displacement from trap center vs time are shown. Black/red curves are an average of 10 trials at 3 mm/s strain speed in 1.0 mg/ml DNA. Four stages of the experiment are shown: (Equilibration) Probes are trapped…… 91

Figure 6.2 DNA response during constant rate strain. (a) Measured stress, σ, vs strain, γ, in 1.0 mg/ml DNA for strain rates Wi = 3.6 to 126 (see legend in (b)). (b) Corresponding differential modulus, K, vs strain for each strain rate. (c) Apparent viscosity η vs. strain rate for 0.3 (circles), 0.5 (triangles)…….. 94

Figure 6.3 Probe recoil dynamics following strain. (a) Measured probe recoil, r, (normalized by tube diameter d_T) vs. time (normalized by disengagement time τ_d) when released immediately after strain (wait time t_w=0). Strain rates of Wi = 5.4 to 108 in 0.5 mg/ml DNA are shown…… 97

Figure 6.4 Sample force traces for a probe dragged in a purely Newtonian fluid (9% w/v, unentangled, 500 kDa dextran solution). A probe is captured in solution and allowed 2 seconds to equilibrate. This is followed by the strain phase in which the bead is pulled 30 mm at a constant strain rate…….. 100

ACKNOWLEDGEMENTS

I would like to thank my advisor Doug Smith for all his support, direction, and flexibility in allowing me to work in a lab off campus. I would especially like to thank Dr. Rae Anderson for not only putting up with me all these years in her lab, but for her incredible guidance, insight, encouragement, and constant support. I could not have asked for a better mentor. I would also like to thank my committee members for their valuable input. I would like to express my gratitude to Patrick Smith, Sara Church, Isa Masongsong and Kevin Forey for preparing many of the DNA samples used for the studies in this thesis. I would also like to thank Kent Lee and Dean Henze for their assistance with the optical traps and more importantly for the endless trips to Urbane, great conversations that constantly kept me on my toes, and for tolerating my music in lab all day every day (I'm on a plain…). I would also like to express my sincere thanks to Stephanie Gorczyca for her countless hours collecting data, using her creative eye to help with figures and most importantly for being hilarious and making the lab a fun and upbeat environment to work in. I'd also like to thank fellow physics graduate student Matt Affolter for all the time spent watching 'Always Sunny' and playing Skyrim (well ain't this a surprise!). I definitely won't have to intervene on him for a lack of good ideas. And lastly, I'd like to thank my parents for providing me with more support and encouragement than I could have possibly asked for. Since I first showed an interest in science as a kid (did you know some trees can breathe underwater?) you've not only encouraged me to follow my passions but also gone

above and beyond to support me in those passions (like taking me to ‘rock’ shows). So thank you for everything.

Chapter 3, in full, is a reprint of the material as it appears in Soft Matter. Chapman CD, Shanbhag S, Smith DE, & Robertson-Anderson RM (2012) Complex effects of molecular topology on diffusion in entangled biopolymer blends. *Soft Matter* 8(35):9177-9182. The dissertation author was the primary investigator and author of this paper.

Chapter 4, in full, is a reprint of the material as it appears in Biophysical Journal. Chapman CD, Gorczyca S, & Robertson-Anderson RM (2015) Crowding Induces Complex Ergodic Diffusion and Dynamic Elongation of Large DNA Molecules. *Biophysical journal*, *108*(5):1220-1228. The dissertation author was the primary investigator and author of this paper.

Chapter 5, in full, is a reprint of the material as it appears in Macromolecules. Chapman CD, Lee K, Henze D, Smith DE, & Robertson-Anderson RM (2014) Onset of Non-Continuum Effects in Microrheology of Entangled Polymer Solutions. *Macromolecules* 47(3):1181-1186. The dissertation author was the primary investigator and author of this paper.

Chapter 6, in full, is a reprint of the material as it appears in Physical Review Letters. Chapman CD & Robertson-Anderson RM (2014) Nonlinear Microrheology Reveals Entanglement-Driven Molecular-Level Viscoelasticity of Concentrated DNA. *Phys Rev Lett* 113(9):098303. The dissertation author was the primary investigator and author of this paper.

VITA

2008 Bachelor of Science, Westmont College

2010 Master of Science, University of California, San Diego

2015 Doctor of Philosophy, University of California, San Diego

PUBLICATIONS

Chapman CD, Shanbhag S, Smith DE, & Robertson-Anderson RM (2012) Complex effects of molecular topology on diffusion in entangled biopolymer blends. *Soft Matter* 8(35):9177-9182.

Chapman CD, Lee K, Henze D, Smith DE, & Robertson-Anderson RM (2014) Onset of Non-Continuum Effects in Microrheology of Entangled Polymer Solutions. *Macromolecules* 47(3):1181-1186.

Chapman CD & Robertson-Anderson RM (2014) Nonlinear Microrheology Reveals Entanglement-Driven Molecular-Level Viscoelasticity of Concentrated DNA. *Phys Rev Lett* 113(9):098303.

Chapman CD, Gorczyca S, & Robertson-Anderson RM (2015) Crowding Induces Complex Ergodic Diffusion and Dynamic Elongation of Large DNA Molecules. *Biophysical journal*, *108*(5):1220-1228.

FIELDS OF STUDY

Major Field: Physics

Studies in Polymer Physics and Biophysics
Professor Douglas E. smith

ABSTRACT OF THE DISSERTATION

The Dynamics of Entangled DNA Networks using Single-Molecule Methods

by

Cole David Chapman

Doctor of Philosophy in Physics

University of California, San Diego, 2015

Professor Douglas E. Smith, Chair

Single molecule experiments were performed on DNA, a model polymer, and entangled DNA networks to explore diffusion within complex polymeric fluids and their linear and non-linear viscoelasticity. DNA molecules of varying length and topology were prepared using biological methods. An ensemble of individual molecules were then fluorescently labeled and tracked in blends of entangled linear

and circular DNA to examine the dependence of diffusion on polymer length, topology, and blend ratio. Diffusion was revealed to possess a non-monotonic dependence on the blend ratio, which we believe to be due to a second-order effect where the threading of circular polymers by their linear counterparts greatly slows the mobility of the system. Similar methods were used to examine the diffusive and conformational behavior of DNA within highly crowded environments, comparable to that experienced within the cell. A previously unseen gamma distributed elongation of the DNA in the presence of crowders, proposed to be due to entropic effects and crowder mobility, was observed. Additionally, linear viscoelastic properties of entangled DNA networks were explored using active microrheology. Plateau moduli values verified for the first time the predicted independence from polymer length. However, a clear bead-size dependence was observed for bead radii less than ~3x the tube radius, a newly discovered limit, above which microrheology results are within the continuum limit and may access the bulk properties of the fluid. Furthermore, the viscoelastic properties of entangled DNA in the non-linear regime, where the driven beads actively deform the netw ork, were also examined. By rapidly driving a bead through the network utilizing optical tweezers, then removing the trap and tracking the bead's subsequent motion we are able to model the system as an over-damped harmonic oscillator and find the elasticity to be dominated by stress-dependent entanglements.

Chapter 1

Polymers, Single-Molecule Studies

1.1 Polymer introduction

A polymer is a unique macromolecule, made up of repeated subunits of monomers, which display rich, complex behavior when in concentrated solutions or melts. Polymers are pervasive in everyday life; they are prevalent in nature and make up such basic materials as silk, wool, and the cellulose in cell walls, and are also ideally suited for more complex roles as seen in RNA, proteins, and the storage of genetic material in DNA. Polymers may also be industrially synthesized and are pivotal for a variety of fields such as the materials industry, where they are used to create such common and important materials as nylon, plastics, and rubber. When concentrated, polymeric fluids display unique viscoelastic properties, exhibiting both a viscous and elastic response to deformations, which are highly dependent on the polymer length, structure, and topology. This 'tunability' is a large part of what makes polymers and polymeric fluids such an important part of the materials industry.

1.2 Modeling polymers

The simplest and most straightforward method for modeling polymers is to treat them as a system of N rigid rods, each of length b, referred to as the Kuhn length, where the length of the polymer, L, is then simply Nb. The Kuhn length (twice the

persistence length for a flexible polymer) is commonly used to describe the flexibility of a polymer. The rods are connected at a joint and oriented via a simple self-avoiding random walk, where no two segments of the polymer may occupy the same space. This is referred to as the freely jointed chain, or Gaussian chain model and the result is a random, roughly spherical coil (Figure 1.1) (1). The approximate size of this coil, termed the radius of gyration, is an important quantity in polymer physics and is defined as $<R_g> = Nb^2/6$ and scales as $Rg \sim L^{1/2}$ for an isolated polymer in an ideal solution (1).

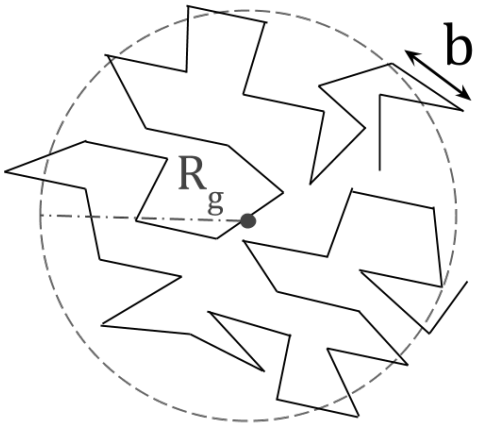

Figure 1.1 The Gaussian chain model, where a polymer is composed of N rigid rods of length b. The random orientation of the joints results in an approximately spherical coil, of radius R_g.

1.3 Reptation model

For dilute polymer solutions, the distance between polymers is large enough that intermolecular interactions may be ignored. As the concentration, c, increases however, the polymers will begin to overlap with one another for $c > c^*$, where c^* is

known as the overlap concentration (1). The dynamics of this semi-dilute regime are described by the Rouse model where the excluded volume interaction and the hydrodynamic interaction are disregarded (1). In this regime, the diffusion of individual polymers, D, will be slowed due to the presence of the surrounding molecules and is predicted to scale inversely with polymer length, $D \sim L^{-1}$. The diffusion has a slightly weaker predicted dependence on concentration and scales as $D \sim c^{-1/2}$.

For concentrations much higher than c^*, the polymers become highly entangled with one another, significantly reducing the mobility of individual polymers and the system as a whole. The dynamics for concentrations at which entanglements dominate, $c > c_e$, where c_e is the so called critical entanglement concentration ($c_e \sim 6c^*$ (2)), are best described via the reptation model, first introduced by de Gennes in 1971 and the cornerstone of entangled polymer physics (3). In this model, each polymer in the solution is confined to a tube-like region by the surrounding polymers, thus restricting the diffusion of the polymer to one-dimension along the axis of the tube and preventing any motion transverse to the tube (Figure 1.2). In this way, a highly complex, many-body problem (a polymer confined by many other polymers) is simplified into the manageable problem of a single polymer in a static confining tube (4). As the polymer diffuses via Brownian motion along the tube, the ends of the polymer escape this confinement and explore the surrounding area, thus creating a new portion of the tube, while the vacated end (opposite the exploring end) of the tube is destroyed, as the tube is not persistent. In this manner, the polymer reptates (so

named for its similarity to the motion of a snake) out of its confining tube, while forming a new one. The time-scale required for a polymer to vacate its tube is known as the disengagement time and is predicted to scale with polymer length for a monodisperse solution as L^3, where $\tau_d = N^3 b^4 \varsigma_0 / \pi^2 k_B T a^2$ (5). τ_d can be evaluated experimentally and is highly dependent on polymer length, concentration, and topology. Experimentally, however, $\tau_d \sim L^{3.4}$ rather than the predicted scaling of 3 (6). The difference is accounted for in what is known as tube or contour length fluctuations, where the polymer chain will undergo thermally driven contraction and stretching, thus the tube is 'forgotten' more quickly than would be otherwise (4). Additionally, due to polymer entanglements, diffusion in this regime is significantly slowed, with a stronger dependence on polymer length and solution concentration, $D \sim L^{-2} c^{-7/4}$, than in the Rouse model. Similar to the experimentally observed increase in length dependence seen for the disengagement time, accounting for contour length fluctuations corrects for the slight discrepancy between initial reptation model predictions and observation for diffusion, resulting in $D \sim L^{-2.3}$ (7).

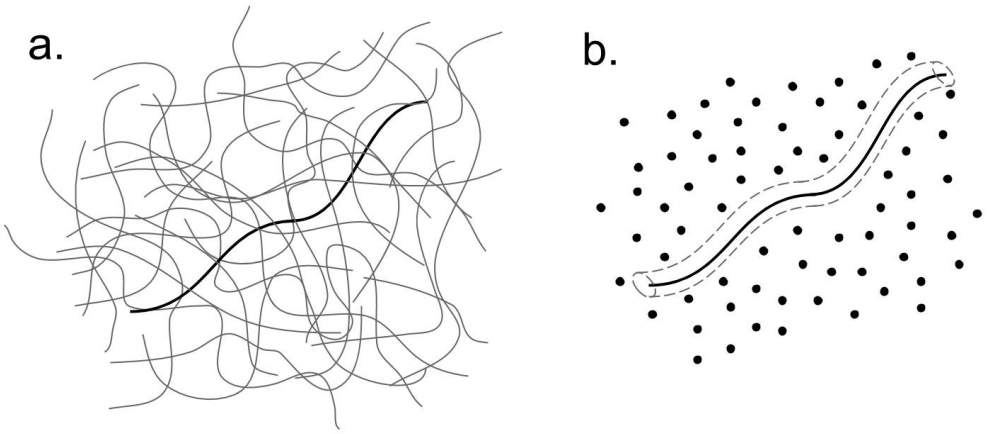

Figure 1.2 (a.) A polymer entangled in a concentrated network of surrounding polymers. (b.) The surrounding polymers may be modeled as simple obstacles, restricting the polymer to a tube-like region, along which the polymer may reptate.

It should be noted that this model provides a coarse picture of the internal dynamics of entangled polymer networks (albeit an incredibly powerful one, which makes countless accurate scaling predictions), with many subsequent theories attempting to fill in some of the finer details to increase our resolution of the behavior of individual polymers within these networks. In addition, the tube model, originally developed for polymer melts, has been successfully extended to apply to entangled polymer solutions using 'blob' theory. In this theory, the solution is modeled as a melt of chains. Each chain is then divided into correlation blobs with the blobs then becoming the effective monomers of the system (8).

1.4 Single-molecule technique basics

As mentioned previously, the reptation model has been incredibly successful in its many predictions yet fails to fully describe the physical dynamics at the molecular level. Single-molecule techniques, central to the research described in this thesis, provide a method for revealing new insights into the internal dynamics of polymer behavior at the molecular, rather than bulk, level. With this method, individual molecules are typically labeled (typically with a fluorescent marker) and observed and recorded, allowing for direct observation of single-molecule dynamics such as their simple Brownian diffusion. This has led to many important findings: For example, single-molecule techniques have allowed researchers to directly visualize polymers undergoing reptation within an entangled network (9), confirming the validity of the tube model and have even measured the confining force from these tubes for an individual polymer in solution (10).

1.5 DNA as a model polymer

Although many candidates exist, DNA has been shown to be ideally suited for single-molecule polymer studies for many reasons. Perhaps the strongest case for using DNA is the sample monodispersity. Unlike synthetic polymers, the length of each DNA molecule is exactly known and additionally the topology may be tightly controlled through the use of enzymes, with little risk of contamination, a current impossibility in industrially synthesized polymers (11, 12). The often drastic change in viscoelastic properties from even a small fraction of impurities (linear polymers in a

circular polymer solution, for example) highlight the advantage of using DNA over other synthetic polymers (13). DNA molecules may also be easily labeled with fluorescent molecules, for straightforward visualization. Building on the previous work of Dr. Anderson and Dr. Smith, DNA was used as the polymer of choice for the studies in this thesis.

1.6 DNA preparation

DNA samples for study are prepared via *E. coli* bacterial stocks, containing the DNA sequence of interest, stored at -80° F. The *E. coli* cells are placed into a nutrient rich LB broth and allowed to multiply overnight. Following centrifugation, the cells are lysed to release their cellular contents. Through a series of purifications, the DNA molecules are isolated, yielding a pure DNA solution typically ranging from ~ 0.5 – 2 mg/ml. The topology of the resulting DNA is supercoiled, however, so enzymes are added to convert the DNA to the desired topology of either relaxed circular or linear. For a more thorough explanation of the DNA preparation, see reference (14).

To visualize the DNA, the molecules of interest are labeled with an intercalating dye, YOYO-1, which has an excitation/emission of 491/509 nm (Figure 1.3). Through the use of basic filters, we can isolate the emission wavelength to visualize the labeled DNA exclusively. When attached to DNA, the dye is ~10^3x brighter than when free in solution, ensuring only the bound dye molecules are detected. A trace amount of the fluorescently labeled DNA molecules are embedded within the network of interest, then videos of individual molecules diffusing are

recorded with their positions and conformations tracked using custom written software (Matlab). Hundreds of videos are recorded for each case of interest, to build up a statistically significant ensemble of molecules, from which a diffusion coefficient and other relevant parameters are calculated.

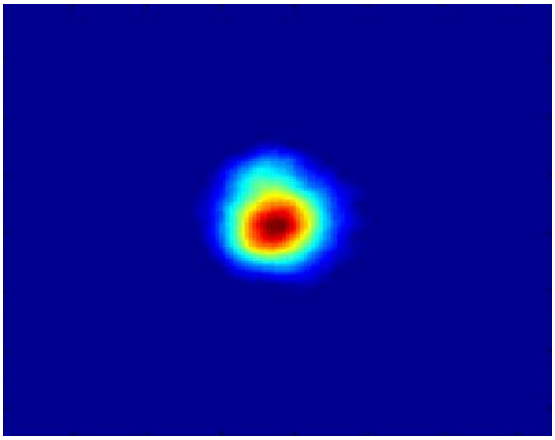

Figure 1.3 A 115 kbp DNA molecule, labeled with YOYO-1 dye.

1.7 Particle Tracking

To calculate the center of mass (COM) of the individual molecules, an approximately uniform distribution of dye molecules (~4:1 base pair to dye ratio) along the DNA molecule is assumed. Under this assumption, the brightness is proportional to the mass of the molecule, allowing the brightness to be used as a proxy for calculating the DNA COM. From the COM values, the ensemble averaged mean squared displacement (MSD) can be calculated, $\langle|x - x_0|^2\rangle$. Here, the Einstein relation, $\langle|x - x_0|^2\rangle = 2Dt$, is invoked to extract a diffusion coefficient, D (1).

Additionally, the conformation of the diffusing DNA molecules may be evaluated. Custom written code (Matlab) is used to determine the outline of the DNA, which is used for conformation analysis and its dependence on the environmental conditions of the polymer solution.

1.8 Simulations

In addition to experiments, simulations play a large role in polymer theory and can be used to aid in explaining the physics/mechanics behind certain phenomena observed in single molecule studies. For example, in the lattice based bond fluctuation model (BFM), monomers are placed and may occupy the vertices of a simple cubic lattice (15). BFM is a Monte Carlo simulation, therefore a monomer from the system is selected at random and also moved at random if the move direction is permissible, i.e. satisfies the defined conditions such as not occupying the same vertex as another monomer, bond length does not exceed threshold value, etc. Using this model, individual polymer COMs can be tracked over time (Monte-Carlo step) to determine an ensemble averaged MSD, allowing multiple parameters of interest to be calculated.

1.9 Open questions in polymer physics

Despite their ubiquity and the existence of reptation theory dating back more than 40 years, many open questions in polymer physics remain. For example, the dynamics of blends consisting of both linear and circular polymers, important particularly in industry and medicine in the creation of tunable materials and

biomaterials, are still not well understood. Additionally, within highly crowded environments, comparable to the dense intracellular environment, sub-diffusive behavior has been reported (16) with the potential crowding effects (pivotal for such medicinal areas as gene therapy and drug delivery (17), which often rely solely upon diffusion as a delivery mechanic) defying classical reptation theory, as the typical crowders may be too short to entangle with one another.

These are just a few of the questions my research attempts to answer, as the advancement of polymer theory, via single-molecule techniques, has huge implications in industry, medicine, and a variety of other fields.

Chapter 2

Rheology and Microrheology

2.1 Rheology

Rheology is the study of a fluid's response to deformation and is used to determine a fluid's viscoelastic properties in bulk. Typical rheological measurements involve applying an oscillatory strain and recording the fluid's response to the applied strain. For a purely viscous fluid, the shear stress, σ, is purely proportional to the shear rate, that is $\sigma \sim \gamma'$, whereas for a purely elastic fluid the shear stress is proportional to the current shear strain, $\sigma \sim \gamma$. Various geometries for rheometers exist such as the parallel plate model, where a strain is induced via rotation of the plate(s), and the cone and disk model, where a rotating cone has the added benefit of creating a uniform shear rate throughout the fluid.

Entangled polymer solutions are viscoelastic and behave as a non-Newtonian fluid, that is their apparent viscosity varies with shear rate. Often, the apparent viscosity of an entangled polymeric fluid decreases with increased strain, a phenomena known as shear thinning. For low oscillation frequencies, referred to as the terminal regime, viscoelastic fluids are liquid-like with $G'' > G'$. Here $G' \sim \omega^2$ and $G' \sim \omega$. From this rapid growth (ω^2 scaling) G' will eventually exceed G'' for increasing ω, thus the elasticity of the fluid will begin to dominate the response (5). The point at which $G' \sim G''$ is known as the crossover frequency and can be used to calculate the disengagement time, $\tau_d = 1/\omega_c$. Here, the induced deformations from the oscillations

are occurring quicker than the timescale at which the polymers may reptate out of their confining tube, resulting in the observed increase in elasticity.

2.2 Microrheology

While highly effective at measuring the viscoelastic properties of complex fluids in bulk, ultimately rheology must rely on theoretical predictions to infer the behavior of a given fluid at the molecular level. As a response to this need for higher resolution, a powerful and relatively new set of techniques known as microrheology have been developed, capable of directly probing the local viscoelasticity at the molecular level. Microrheology has a number of advantages including small sample sizes, sensitivity to small forces (on the order of piconewtons), and the ability to detect microscale heterogeneities, imperceptible to classic bulk rheology techniques. All microrheology measurements involve embedding a dilute amount of micron-sized beads into the complex fluid of choice and operate under the assumption that the material behaves as a homogenous continuum on the length scale of the probe. From there, however, two distinct classes of measurements exist, passive and active microrheology.

In passive microrheology, the embedded beads are allowed to diffuse naturally via Brownian motion with their positions tracked. From the particle tracking, an MSD is developed from which the viscoelastic properties are deduced. The bulk modulus, G^*, can be calculated from the MSD, $G^* = \frac{k_B T}{\pi a s \langle \Delta r^2(s) \rangle}$. Then using the relation:

$G^* = G' + iG''$, G' and G'' can be determined, where G' is the elastic modulus and the real portion of G^*, and G'' is the loss modulus and the imaginary portion of G^* (18).

In active microrheology, on the other hand, the embedded microspheres are actively driven via magnetic or optical tweezers. Magnetic tweezers utilize super-paramagnetic particles (18), which are driven by strong magnets and tracked using video microscopy. Optical tweezers, on the other hand, use highly focused lasers to capture and drive individual embedded microspheres (19). Radiation pressure from the refracted light pulls the bead (of a higher index of refraction than the medium) towards the center of the trap radially and also counters the scattering force felt from the reflected light, preventing the bead from travelling upstream in the direction of laser propagation. Conservation of momentum dictates that any radial displacement of the bead from the trap center results in a deflection of the beam, typically recorded downstream from the focal plane using a position-sensing detector (PSD). Additionally, for small displacements radially, the restoring force is approximately that of a Hookean spring and thus a spring constant or trap stiffness, k_{trap}, may be calculated by observing the beam deflection for a trapped bead oscillating within a solution of known viscosity, such as water (η = 0.001 Pa s) using simple Stokes' drag, $F = k_{trap}\Delta x$ and $F = 6\pi\eta Rv$. Using this method, pN-scale forces can be accurately measured to track a fluid's response to deformations from the optically driven microsphere, which are typically oscillated sinusoidally (Figure 2.1).

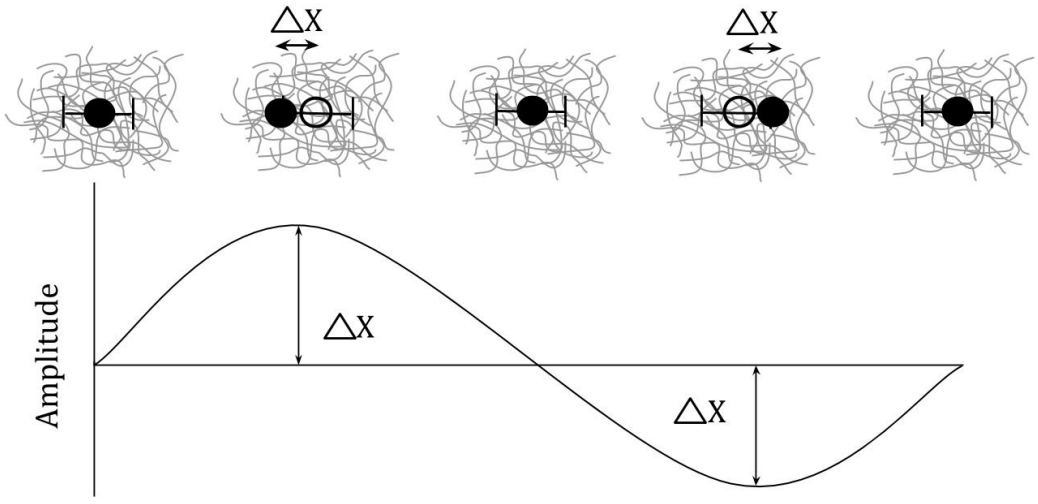

Figure 2.1 Active microrheology schematic. An embedded microsphere is captured and oscillated sinusoidally at a fixed frequency and amplitude. The displacement of the microsphere from trap center is used to calculate the force felt by the microsphere.

2.3 Tweezers setup

For our microrheology measurements, we have developed and built a dual-force optical tweezers setup using a highly modified, inverted fluorescence microscope (IX-71, Olympus). The traps are formed from a 1W, 1064 nm fiber optic laser which is initially directed through a Faraday isolator, preventing any interference caused by back-reflection of the beam. The beam then travels through a beam expander, which increases the beam diameter by 20x. Following expansion, the beam is then split into two distinct polarizations using a polarizing beam splitter (PBS). One beam is then reflected off a static mirror while the other beam is reflected off a

steerable, piezoelectric mirror allowing manipulation of the final trap position, with both beams then directed towards a second beam expander. Following the second expansion, the beams travel through a 1.2 NA, 60X water immersion objective, which tightly focuses the beams, creating two distinct optical traps. The beams are then re-collimated using a 1.4 NA oil immersion condenser and are again split with a PBS and directed to two separate PSD's, which constantly monitor the traps' position at 20 kHz. Schematic of the setup is shown in Figure 2.2.

The two traps may be driven sinusoidally relative to the solution by oscillating the sample stage (while the traps remain stationary) at varying frequencies, resulting in a sinusoidal force response, which can be fit to a sine function and used to calculate the frequency dependent viscoelasticity of the fluid. The portion of the force response in phase with the stage velocity represents the viscous portion, while the elastic portion is in phase with the stage position. Additionally, the inverted microscope is capable of simultaneous epi-fluourescence microscopy, allowing for direct visualization of the sample chamber throughout any experiment.

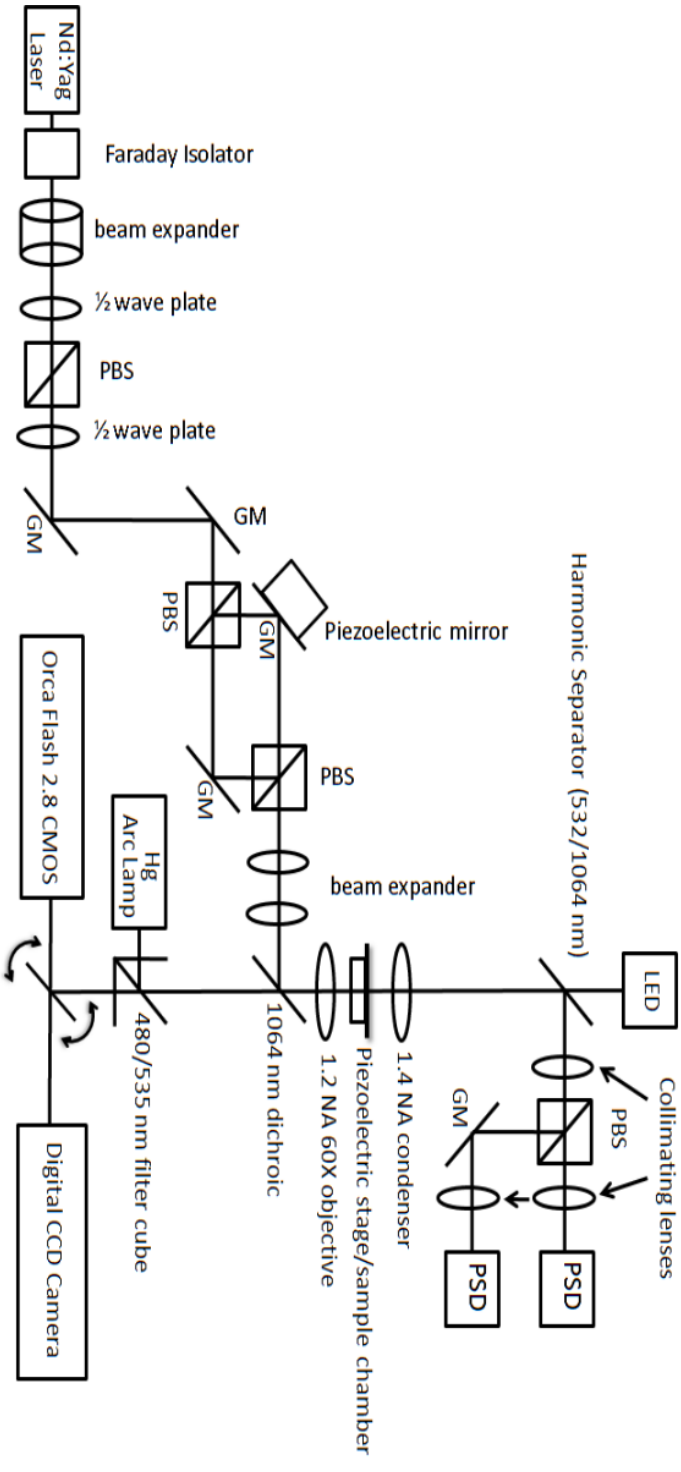

Figure 2.2 Schematic for dual-force optical tweezers setup with epi-fluorescence microscopy.

2.4 Open questions in rheology

It has been widely assumed that for microrheology studies to access the macroscopic rheological properties of complex fluids, the embedded microspheres must be larger than the mesh size of the entangled network. For beads smaller than this mesh size, particles used in passive studies have been found to diffuse much quicker than predicted by the Stokes-Einstein relation (20, 21). However, this limit, where the bead must simply be larger than the characteristic mesh size of the network, is yet to be experimentally validated and is critical to proper interpretation of microrheological results.

Additionally, while the reptation model has been incredible in its ability to predict scaling for many observations in linear rheology, the dynamics (and subsequent scaling predictions) break down for non-linear measurements. In this non-linear regime, the network undergoes significant deformation, where the classical tube theory assumption that the tube walls are static and uncrossable breaks down. Multiple theories and extensions have been proposed to account for these discrepancies with classical tube theory including the idea of chain-stretching, convective constraint release and entanglement constraint effects, among others. Research from this thesis attempts to clarify some of the issues associated with this non-linear regime (Chapter 6).

In addition to the examination of the diffusion of individual molecules, which shed light on the mechanics of individual polymers in solution, these are a few of the

questions my research attempts to answer regarding the dynamics of entanglements and polymer networks as a whole.

Chapter 3

Complex Effects of Molecular Topology on Diffusion in Entangled Biopolymer Blends

3.1 Abstract

By combining single-molecule tracking with bond-fluctuation model simulations, we show that diffusion is intricately linked to molecular topology in blends of entangled linear and ring biopolymers, namely DNA. Most notably, we find a previously unreported non-monotonic dependence of the self-diffusion coefficient for linear DNA on the fraction of linear DNA comprising the ring-linear blend, which we argue arises from a second-order effect of ring DNA molecules being threaded by varying numbers of linear DNA molecules. Results address several debated issues regarding molecular dynamics in biopolymer blends, which can be used to develop novel tunable biomaterials.

3.2 Introduction

Entangled polymers display complex diffusional transport properties that are strongly dependent on molecular concentration, length, and topology. One such system of great interest is DNA, which is not only an important biopolymer, but has also served as a powerful model system for probing general polymer physics questions (22-25). While most progress has focused on monodisperse linear and branched

polymers, blends of polymers of varying lengths and topologies are favored in practical materials engineering to effectively tune properties such as miscibility, strain hardening, etc (26, 27). Biological cells, which exhibit remarkable mechanical properties, also contain a mixture of nucleic acid and protein polymers of varying topologies.

The most powerful theoretical concept in entangled polymer dynamics is the tube model, which postulates that each individual entangled polymer is effectively confined, by the surrounding molecules, to diffuse in a tube-like region parallel to its contour (i.e. reptation). While originally developed for polymer melts, the tube model has been successfully extended to polymer solutions using ‘‘blob’’ theory (28-30), in which each chain is divided into correlation blobs and the solution is modeled as a melt of chains with monomer size equal to the blob size. While the chain-end mediated process of reptation is the foundation of much of our present understanding of the dynamics of linear and branched polymers, extension of the tube model to ring polymers, which have no ends by which to execute standard reptation, is nontrivial and recognized as a major challenge (11, 31-47). Further, experimental data on entangled rings is highly conflicting (11, 34-36, 48) due, in part, to the extreme difficulty of synthesizing samples of purely ring polymers devoid of linear contaminants (11, 49), coupled with the fact that small quantities of linear polymers appear to dramatically alter the rheological properties of ring polymer melts (11, 33, 35, 50). Nonetheless, blends of linear and ring polymers hold great promise as viscoelastic materials and fluids with highly tunable properties.

Recently, we used single-particle tracking to measure self-diffusion coefficients of linear and ring DNA molecules in solutions of entangled linear or ring DNA, and observed dramatic effects of molecular topology (2, 39). In these studies, tracked linear or ring molecules were added to each solution at essentially infinite dilution, so "tracer" diffusion coefficients in entangled solutions of purely linear or purely ring DNA were measured. Tracer diffusion coefficients exhibited a strong and complex dependence on the topology of both the tracer and the surrounding entangling molecules, and this dependence was most dramatic for the longest molecular lengths and highest solution concentrations examined (i.e. highest degree of entanglements). Diffusion in blends containing significant fractions of both ring and linear molecules (ring-linear blends) is expected to exhibit even richer behavior.

In ring-linear (RL) blends, rings can become threaded by their linear counterparts, in which case the only available diffusive mechanism is predicted to be via the threading linear polymers releasing their constraints by unthreading themselves (via reptation) (31, 46, 51, 52). This constraint release process, for which there is indirect experimental evidence (11, 39, 47), is much slower than reptation. Several other ring polymer configurations have also been conjectured in RL blends including once-threaded, unthreaded-linear, and unthreaded-branched (31, 37, 46, 52). Each configuration relies on different diffusive mechanisms, but the extent to which each configuration and diffusive process play a role in RL blends is still debated (31, 40, 46, 47).

Rheological studies have examined bulk properties of RL blends such as viscosity, relaxation spectra and terminal relaxation times (11, 33, 35, 44, 50), attempting to test theoretical predictions (31, 40, 52). While previous studies have all found a larger than expected rise in viscosity of ring polymer melts upon addition of small amounts of linear polymers, the dependence of viscosity on the fraction of linear polymers in the blend (f_L) remains unclear. Some experimental and simulation studies have reported a non-monotonic dependence of viscosity on f_L with a maximum reached at $f_L \approx 0.5$ (53, 54), while others have found that viscosity consistently increased with f_L, approaching but never surpassing the value for a pure linear polymer melt (55, 56), Rings have also been shown to have shorter relaxation times and different relaxation spectra than linear polymers of equal length (11, 25, 33, 35, 57). However, the purity of the ring samples and extent to which the rings are entangled in each of these studies remains controversial.

Molecular diffusion in RL blends has been examined in recent experiments (44, 47, 58-60) and simulations (43, 61) which have reported conflicting results with multiple theoretical interpretations. Most recently, NMR was used to measure the dependence of the average blend self-diffusion (D_{blend}) and ring polymer self-diffusion (D_R) on f_L. While D_R decreased linearly with increasing f_L, D_{blend} showed a non-monotonic dependence on f_L with a minimum reached at $f_L \approx 70\%$ (44). These results contrast with previous findings reporting that blend composition has little effect on diffusion in RL blends (32, 62).

Previously, we implemented a Monte Carlo simulation approach to model RL blends, using a simple bond-fluctuation model (BFM) with discretized polymers on a lattice. The predictions of the model were consistent with our experimental results described above (2, 39). In addition, we predicted that the self-diffusion coefficient for ring polymers (D_R) would decrease nonlinearly with the fraction of linear polymers in the blend (f_L), decreasing more rapidly at low f_L and slowly reaching a plateau at the highest f_L (41). We also predicted that the linear polymer self-diffusion coefficient (D_L) would decrease at low f_L and reach what we believed to be a f_L-independent plateau around $f_L \approx 30\%$.

In this article, we present experimental and simulation results that, for the first time, systematically characterize the effect of molecular diffusion of both linear and ring molecules on blend composition in entangled ring-linear blends.

3.3 Methods

We have chosen to use double-stranded DNA as our model polymer for the described experiments, as DNA, beyond its biological importance has been well established as a model system for probing fundamental questions in polymer physics (22, 24, 25). Further, DNA is amenable to several experimental techniques which are advantageous for the present studies including preparation of ring constructs (11, 12, 63), fluorescent-labeling and single-molecule tracking of tracer molecules. While DNA is less flexible than typical synthetic polymers, a well-accepted notion in current polymer theory is that polymers of varying chemical composition, length and

flexibility when scaled according to the number of monomers or "blobs", exhibit universal properties (28, 30).

Details of all experimental techniques used, briefly summarized below, have been thoroughly described in Refs. (2, 14, 39, 64). Double-stranded DNA molecules, with contour lengths of 11 and 45 kilobasepairs (kbp), corresponding to 3.74 μm (~75 persistence lengths) and 15.3 μm (~305 persistence lengths), respectively, were prepared by replication of cloned plasmid and fosmid constructs in E. coli, followed by extraction and purification. Restriction enzymes (BamHI, ApaI) and Topoisomerase I were used to prepare linear and ring forms, respectively. Blended solutions of varying weight fractions of linear and ring DNA, in aqueous buffer (10 mM Tris-HCl (pH 8), 1 mM EDTA, 10 mM NaCl), with overall solution concentrations (c) of 0.1, 0.5 and 1.0 mg/ml were prepared, as depicted in Figure 3.1. A trace amount ($<10^{-3}c$) of linear or ring DNA (tracers), labeled with YOYO-I (Invitrogen) for tracking, was mixed with the desired blended DNA solution (see Figure 3.1), and imaged with a fluorescence microscope using a 60x 1.2 NA water-immersion objective. Note that because the tracer concentration is <1/1000 of the overall solution concentration, the presence of the tracers can be neglected when determining the overall solution concentration c and the weight fraction of linear DNA in the blended solution (f_L). As reviewed in Ref (24), YOYO-I labeling slightly increases both the persistence length and contour length of DNA by ~1.34. However, the number of persistence lengths and basepairs per persistence length remain unchanged. This small length change has a minimal effect on the dynamics of the

tracer DNA (2, 64), such that tracers are representative of the unlabeled DNA of equal length and topology in the solution. Images were captured at 10 frames/sec with a high-resolution CMOS camera (Hamamatsu). Center-of-mass (*x, y*) coordinates of >200 paths of different molecules were tracked, and the Einstein relation $\langle x^2 \rangle = \langle y^2 \rangle = 2Dt$ was used to determine diffusion coefficients. Errors were estimated using the bootstrap method (65).

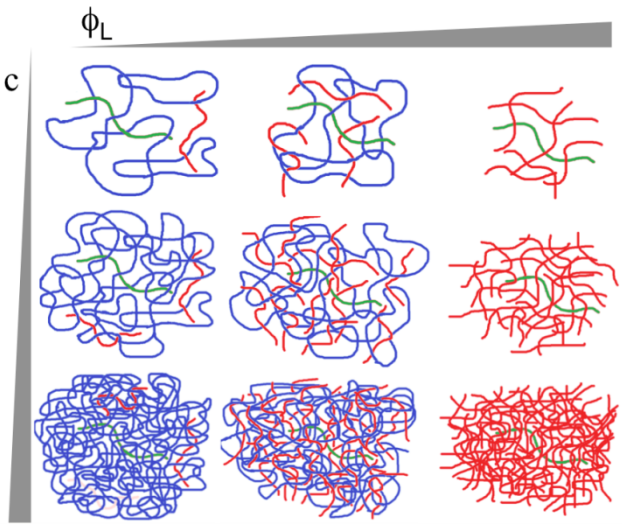

Figure 3.1 Schematic of experimental parameter space probed for ring-linear DNA blends. To track the center-of-mass motion of single linear molecules (to determine D_L) in ring-linear blends, a trace amount of fluorescent-labeled (green) linear tracer chains are embedded in entangled solutions of ring (blue) and linear (red) DNA of varying solution concentration (c) and linear chain fraction (f_L). Concentration increases from 0.1 mg/ml (top row) to 1.0 mg/ml (bottom row) and linear fraction increases from 0 (left column) to 1 (right column). Identical experiments are carried out using fluorescent-labeled ring tracers to determine D_R.

We used the lattice bond-fluctuation model to simulate ring-linear blends and predict molecular self-diffusivities. The underlying protocol, which has been described and validated in sufficient detail previously (41, 43, 61), involves placing and moving beads corresponding to monomers of linear and ring polymers on a simple cubic lattice, subject to the constraints of excluded volume, bond non-crossability, and chain connectivity. The self-diffusion coefficient is computed from the mean-squared displacement of the center-of-mass of the polymers. The 45-kbp system at c = 1 mg/ml was found to be equivalent to N = 316 beads per polymer at a total fractional lattice occupancy of f = 0.5 in the BFM, using the correlation blob model (2, 41). We also performed simulations at f = 0.25 (corresponding to c = 0.5 mg/ml) and f = 0.05 (c = 0.1 mg/ml). For each f, we spanned $0 \leq f_L \leq 1$, adjusting the simulation box size and number of replicas to ensure >500 molecules were used to estimate the self-diffusivity.

3.4 Results

Measured diffusion coefficients for linear and ring tracer DNA molecules are plotted as a function of linear fraction f_L in Figure 3.2. Molecular lengths and solution concentrations probed range from well-above to well-below the critical concentration for entanglement (c_e), above which linear molecules exhibit reptation dynamics (c_e ~ 0.4 mg/ml, ~1.3 mg/ml for 45 kbp, 11 kbp DNA, respectively (2)).

For the 45-kbp DNA at c = 1.0 mg/ml (Figure 3.2a) both D_L and D_R are highest in a pure solution of rings (f_L = 0). D_R decreases rapidly as f_L increases, dropping by a

factor of ~4 with only 20% linear molecules, and by a factor of 8 at 40% linear DNA. For $0.4 < f_L < 1$, D_R continues to monotonically drop, albeit with a weaker f_L dependence, reaching a minimum, ~17 times slower than $D_R(f_L = 0)$, at $f_L = 1$.

Interestingly, our results for D_L display a non-monotonic dependence on the linear fraction f_L, steadily decreasing by a factor of ~3 as f_L increases from 0 to 50%. As f_L is further increased D_L steadily increases, almost doubling as f_L increases to 1. To our knowledge, such behavior was not anticipated by any prior experimental or theoretical work.

At c = 0.5 mg/ml (Figure 3.2b), trends similar to the 1.0 mg/ml case are found for both D_L and D_R, although the dependence on f_L is weakened. D_R decreases by a factor of ~3 as f_L increases from 0 to 1, with a ~2x reduction at $f_L = 0.2$. Likewise, D_L displays a modest non-monotonic dependence on f_L, reaching a minimum at $f_L = 0.6$.

For the lowest concentration (0.1 mg/ml, Figure 3.2c), which is well below the critical concentration for entanglement, both D_L and D_R showed little dependence on blend composition, demonstrating that the complex dependence of molecular diffusion on blend composition is due to molecular entanglements. Similar results were found for ~4x shorter (11-kbp) DNA at 1.0 mg/ml (Figure 3.2c); however the 11-kbp DNA does exhibit a modest decrease in D_R with f_L similar to that of the entangled blends discussed above but much weaker. As the 11-kbp, 1.0 mg/ml system is quite close to the critical concentration for entanglement (c_e ~1.3 mg/ml), this small decrease is expected as entanglements begin to form, and further demonstrates the dependence of the results on molecular entanglements.

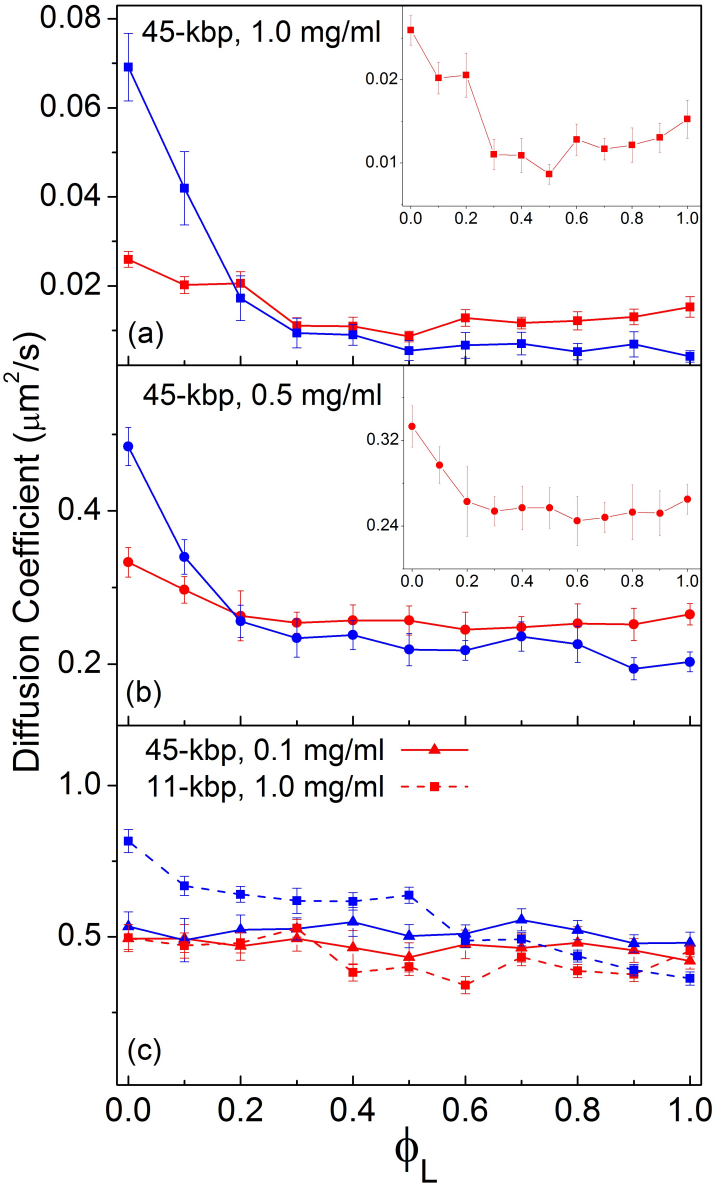

Figure 3.2 Measured self-diffusion coefficients vs. fraction of linear DNA (f_L) in ring-linear blends. Self-diffusion coefficients for ring (blue) and linear (red) DNA in ring-linear blends at three overall solution concentrations, 0.1 mg/ml (triangles), 0.5 mg/ml (circles), and 1.0 mg/ml (squares), and two molecular lengths, 45-kbp (solid lines) and 11-kbp (dashed lines) are shown. The molecular lengths and solution concentrations displayed in each panel, (a), (b), and (c), are listed in the top left corner of the corresponding panel. Insets show zoomed in plots for linear DNA with appropriately adjusted y-axes.

If our BFM simulations capture the essential physics, the mapping between experimental diffusivities ($\mu m^2/s$) and BFM diffusivities ((lattice units)^2/(Monte Carlo Step)) is expected to be proportional. Figure 3.3 presents simulation and experiment results on the same plot, normalized such that $D_L^* = D_L(f_L = 1, c = 1 \text{ mg/ml}) = D_L(f_L = 1, f = 0.5)$.

At the highest ($f = 0.5$) and lowest ($f = 0.05$) concentrations, simulations match experimentally observed trends quite well over the entire f_L range. For the 0.5 mg/ml ($f = 0.25$) case, experimental and simulation results show similar variations of D_L and D_R with f_L, however the magnitudes of the normalized diffusion coefficients differ by a factor of ~2. We believe this discrepancy arises from the fact that this concentration is in the crossover regime between entangled and dilute polymer dynamics, where peculiarities of the BFM lattice are most apparent. For example, previous studies on ring polymers indicate that while both the experiments and the BFM exhibit a crossover from Rouse scaling ($D_R \sim c^{-0.5}$) to reptation scaling ($D_R \sim c^{-1.75}$), and agree in both the dilute (Rouse) and entangled (reptation) regimes, there are noticeable differences in the location ($c_e \sim 0.4$ mg/ml, $f_e \sim 0.25$) and sharpness of the transition (2, 43). Future work will examine this discrepancy in more detail, however it is outside the scope of the current study which is focused on entangled ring-linear blends well above c_e.

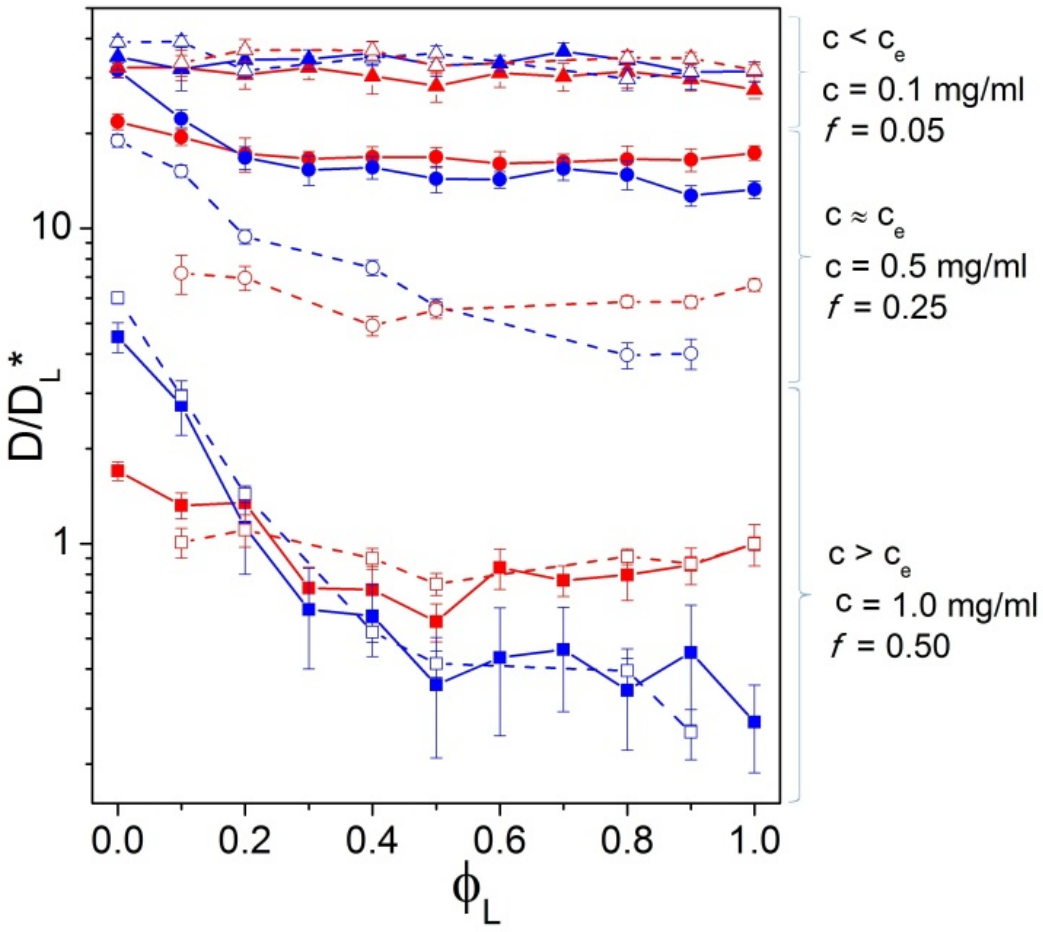

Figure 3.3 Comparison between experiment and simulation results for self-diffusion coefficients vs. linear fraction f_L in ring-linear blends. Experiment (solid lines) and simulation (dashed lines) results are normalized by $D_L^* = D_L(f_L = 1, c = 1 \text{ mg/ml}) = D_L(f_L = 1, f = 0.5)$. Symbols and colors are as in Figure 3.2.

Importantly, the simulations also exhibit the experimentally observed non-monotonic variation of $D_L(f_L)$ at $f = 0.25$ and $f = 0.5$. Because this feature is less prominent than the rapid initial decrease of $D_R(f_L)$, we previously noted that $D_L(f_L)$ appeared to plateau at $f_L \sim 0.3$ in our initial BFM studies (41). However, the observed minimum in D_L is significant as it is above the measured error in both simulations and experiment. The non-monotonicity is also evident in the autocorrelation of the end-to-end vector in the simulations, which is defined as,

$$p_L(t) = \frac{\langle R_{ee}(t) \bullet R_{ee}(0) \rangle}{\langle R_{ee}^2(0) \rangle}$$

where $R_{ee}(t)$ is the end-to-end vector of a linear molecule at time t, and the angular brackets represent an ensemble average over all the linear chains in the system. We used the correlator algorithm, widely used in photon-correlation spectroscopy (66, 67), which allows us to compute $p_L(t)$ on the fly. Figure 3.4 shows that as f_L increases, $p_L(t)$ initially decays more slowly. However, beyond a certain f_L, the trend reverses, and $p_L(t)$ decays more quickly as f_L increases.

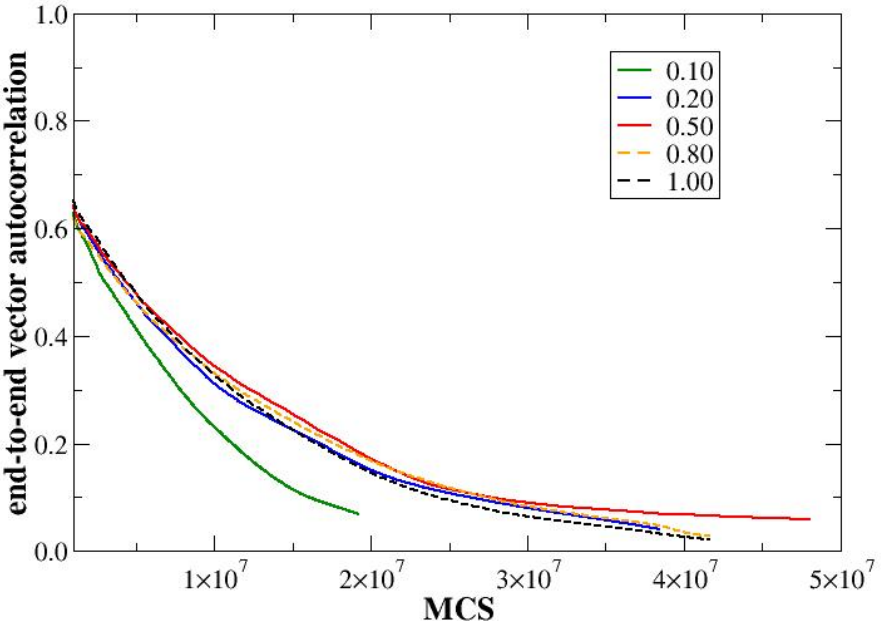

Figure 3.4 The decorrelation of the end-to-end vector of the linear chains at $f = 0.5$ for different f_L values (specified in the legend). The relaxation of the end-to-end vector initially slows down as f_L increases from 0.10 to 0.50, and then accelerates as f_L increases from 0.50 to 1.00. These non-monotonic f_L-dependent dynamics are also evident in Figures 3.3 and 3.5.

3.5 Discussion

While the slowing of ring polymers at small f_L, due to threading, has received much attention, the non-monotonic variation of $D_L(f_L)$ has completely escaped notice. To gain further insight on this feature, we extend the minimal constraint model previously used to explain the variation of $D_R(f_L)$ (41).

In the original model, we considered $D_R(f_L)$ as a competition between constraint release and pure diffusion, with the slower process controlling the overall rate. Characteristic diffusional decorrelation timescales can be defined via $D_i(f_L)$

$=R_{g,i}^2(f_L)/\tau_i(f_L)$, where R_g is the radius of gyration, and i = R (ring) or L (linear). If we ignore the small variation of R_g with f_L (as justified by Refs (40, 54, 61), and treat the polymers as Gaussian coils, the original minimal constraint model can be rephrased as $\tau_R(f_L) = \tau_R(f_L=0) + \tau_{CR}(f_L)$, where the constraint release timescale τ_{CR} depends on the number and mobility of the threading linear chains. From primitive path analysis of simulation data, which shrinks polymer contours without violating topological constraints, we find that the average number of linear polymers threading a ring is approximately $f_L Z$ (40, 41), with Z being the average number of entanglements per molecule in a purely linear polymer melt. Hence, it is reasonable to approximate the Rouse-like contribution as $\tau_{CR}(f_L) \sim \tau_L(f_L)\, f_L Z^2$, which leads to:

$$\tau_R(\phi_L) = \tau_{R0} + c_1 \phi_L Z^2 \tau_L(\phi_L), \qquad (1)$$

where c_1 is a constant, and $\tau_{i0} = \tau_i(f_L=0)$, and $\tau_{i1} = \tau_i(f_L=1)$ for i = R or L. This simplified relation has previously been validated by experimental and simulation data (41).

To extend this model to explain the variation of $D_L(f_L)$, we consider a simple empirical form for $\tau_L(f_L)$, motivated by experimental findings on binary blends of linear polymers (68, 69). When extremely long linear chains with $Z >> 1$ are blended (at fraction f_L) with much shorter linear chains, the viscosity or longest relaxation time of the long molecules $\tau_L(f_L)$ roughly varies as:

$$\tau_L(\phi_L) \approx \phi_L^2 \tau_{L1} + (1-\phi_L^2)\tau_0 Z^2$$

where the time-constant τ_0 establishes the constraint-release Rouse relaxation. By analogy, we hypothesize the following simple form for ring-linear blends:

$$\tau_L(\phi_L) = \phi_L^2 \tau_{L1} + (1-\phi_L^2)\left[c_2 \tau_R(\phi_L) Z^2\right], \qquad (2)$$

where the bracketed term crudely captures the threading of rings via a constraint-release Rouse mechanism, and c_2 is an adjustable parameter. While this is a coarse simplification of complex molecular dynamics, the idea here is simply to explore whether a qualitatively plausible form can rationalize the observed trend.

Equations (1) and (2) are coupled in $\tau_L(f_L)$ and $\tau_R(f_L)$, with two undetermined dimensionless constants c_1 and c_2, which can be determined by considering eq. (1) in the limit of f_L =1, and eq. (2) in the limit of f_L =0, respectively. Thus, $c_1 Z^2 = (\tau_{R1}-\tau_{R0})/(\tau_{L1})$, and $c_2 Z^2 = \tau_{L0}/\tau_{R0}$.

From the diffusivity data at $f_L = 0$ and $f_L = 1$, at 0.5 mg/ml and 1.0 mg/ml, we find $c_1 \sim c_2 \sim 0.01$. In particular, for the 45-kbp, 1 mg/ml case with c_1= 0.008, and c_2=0.012, in eq. (1) and (2), we get Figure 3.5, which qualitatively captures the non-monotonic variation in $\tau_L(f_L)$.

Numerical experimentation with the minimal constraint model indicates that the shape of the curves and the location of the maxima are sensitive to the values of c_1 and c_2. It also points to a necessary criterion for observing the non-monotonic behavior in $\tau_L(f_L)$ clearly, viz. $\tau_{R0}/\tau_{L0} < 1$ and $\tau_{R1}/\tau_{L1} > 1$, requiring that $D_L(f_L)$ and $D_R(f_L)$ cross over, as indeed seen in Figure 3.2. This criterion is satisfied at large *N* or high concentrations, where the minimum in D_L is observed most clearly. The model also suggests that as $\tau_{R1}/\tau_{L1} >> 1$ (perhaps at concentrations and lengths much higher than those explored here), it might be possible to observe minima in D_R as well.

To try to understand the complex interplay of structure and dynamics from a more intuitive standpoint (70), we first ask, "why does τ_R increase monotonically with f_L?" At low f_L, a small fraction of rings are threaded by linear polymers, and rendered sharply less mobile, while the bulk of rings are unthreaded and diffuse essentially freely. As f_L increases, both the fraction of threaded rings and the number of times a particular ring polymer is threaded increases (40), causing $\tau_R(f_L)$, which is an average over all rings, to increase with f_L. Beyond a certain f_L, which depends on Z and *f*, all rings are at least "once"-threaded. The slowdown in mobility is substantial when an unthreaded ring is threaded once; it is less so when a once-threaded ring is threaded twice, which qualitatively explains why the rate of increase in $\tau_R(f_L)$ tapers off in Figure 3.5.

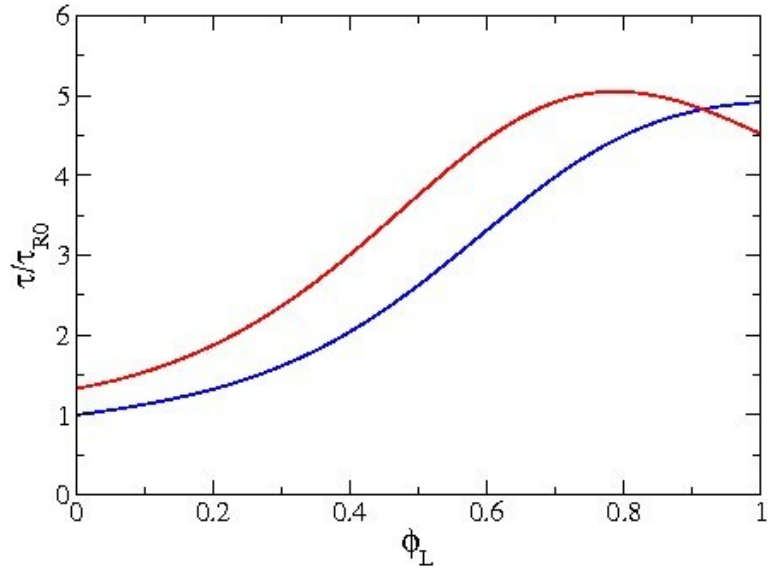

Figure 3.5 The solution of equations (1) and (2) (see text) for $\tau_L(f_L)$ (red) and $\tau_R(f_L)$ (blue), for the 45-kbp, 1 mg/ml case with $c_1 = 0.008$, and $c_2 = 0.012$, exhibits non-monotonic variation in $\tau_L(f_L)$.

The non-monotonic variation in $\tau_L(f_L)$ is more interesting. Previous simulations using primitive path analysis, which indicates how the environment of constraints around a "test" linear polymer varies with f_L (40), demonstrate that the total number of constraints on a linear test chain remains constant (ring constraints decrease while linear constraints increase with f_L). We can combine this structural information with (i) the monotonic increase in $\tau_R(f_L)$ and (ii) $\tau_{R1} > \tau_{L1}$ to explain the non-monotonicity in $\tau_L(f_L)$.

At $f_L = 1$, the linear test chain is only constrained by surrounding linear chains, all having a timescale τ_{L1}. As f_L decreases, at first, one of these constraining linear chains is replaced by a ring polymer. In this regime ($f_L \sim 1$), $\tau_R(f_L) > \tau_{L1}$ (Figure 3.5), since the average ring is threaded multiple times. From the standpoint of the test chain, it exchanged a more mobile constraint with a less mobile one, causing $\tau_L(f_L)$ to initially increase as f_L decreases from 1. Concurrently, however, $\tau_R(f_L)$ decreases with decreasing f_L, as discussed above. The net effect is that as f_L decreases further, a larger fraction of the linear constraints are replaced by rings (effect of structure) that are themselves increasingly mobile (effect of dynamics). Thus, $\tau_R(f_L)$ and $\tau_L(f_L)$ approach each other, and at a certain point $\tau_R(f_L) = \tau_L(f_L)$. Beyond this point, we begin exchanging less mobile linear constraints with more mobile ring constraints. This is manifested as a maximum in $\tau_L(f_L)$ or a minimum in $D_L(f_L)$.

3.6 Conclusion

In summary, we have combined single-molecule experiments with simulation studies to systematically quantify the dependence of molecular diffusion on molecular topology and intermolecular entanglements in blends of linear and ring biopolymers. Among our findings, we observed a previously unreported and unpredicted non-monotonic dependence of linear polymer diffusion on the fraction of linear polymers in the blend, which we have shown can be explained as a second order effect of the slowed diffusion of threaded rings in the blend. Reported results, which resolve several debated issues in polymer physics and chemistry, may also be used to tune novel biopolymer materials and fluids to exhibit specific viscoelastic properties.

3.7 Acknowledgments

Chapter 3, in full, is a reprint of the material as it appears in Soft Matter. Chapman CD, Shanbhag S, Smith DE, & Robertson-Anderson RM (2012) Complex effects of molecular topology on diffusion in entangled biopolymer blends. *Soft Matter* 8(35):9177-9182. The dissertation author was the primary investigator and author of this paper.

Chapter 4

Crowding Induces Complex Ergodic Diffusion and Dynamic Elongation of Large DNA Molecules

4.1 Abstract

Despite the ubiquity of molecular crowding in living cells, the effects of crowding on the dynamics of genome-sized DNA are poorly understood. Here, we track single, fluorescent-labeled large DNA molecules (11, 115 kbp) diffusing in dextran solutions that mimic intracellular crowding conditions (0-40%), and determine the effects of crowding on both DNA mobility and conformation. Both DNAs exhibit ergodic Brownian motion and comparable mobility reduction in all conditions; however crowder size (10 vs 500 kDa) plays a critical role in the underlying diffusive mechanisms and dependence on crowder concentration. Surprisingly, in 10-kDa dextran, crowder influence saturates at ~20% with a ~5x drop in DNA diffusion, in stark contrast to exponentially retarded mobility, coupled to weak anomalous subdiffusion, with increasing concentration of 500-kDa dextran. Both DNAs elongate into lower-entropy states (compared to random coil conformations) when crowded, with elongation states that are gamma distributed and fluctuate in time. However, the broadness of the distribution of states and the time-dependence and scale of elongation length fluctuations depend on both DNA and crowder size with concentration having surprisingly little impact. Results collectively show that mobility reduction and coil elongation of large crowded DNAs are due to a complex interplay between entropic

effects and crowder mobility. While elongation and initial mobility retardation are driven by depletion interactions, subdiffusive dynamics and drastic exponential slowing of DNA, up to ~300x, arise from the reduced mobility of larger crowders. As such, our results elucidate the highly important and widely debated effects of cellular crowding on genome-sized DNA.

4.2 Introduction

Biological cells, comprised of a wide range of macromolecules of varying sizes and structures, are highly crowded, with typical concentrations of ~200-400 mg/ml (20 – 40% w/v) (71). Crowding has been shown to play a principle role in a wide array of biological processes, such as gene expression, protein folding, binding and aggregation, chromosomal compaction, cell volume regulation, and catalytic enzyme activity (17, 71-75). Drug delivery systems, gene therapy, and production and manipulation of synthetic cells and nanomaterials are also highly impacted by cellular crowding (17, 72, 76, 77). Macromolecular mobility is greatly reduced in crowded environments, yet despite these extreme conditions, diffusion is the primary mechanism by which the majority of reactions and interactions occur. Further, crowding has been shown to alter the conformations and stability of nucleic acids and proteins, which greatly impact protein-DNA binding efficiency, transcription and replication (72, 77). Despite the obvious importance of understanding molecular diffusion and configuration in crowded environments, the sheer system complexity, coupled with conflicting experimental and theoretical studies (16, 72) leaves this open

problem widely debated by a range of researchers in biology, physics, engineering, materials science and medicine.

Genomic DNA, storing the genetic code for almost all living things and playing a pivotal role in several other biological functions (78, 79), varies widely in size and conformation among living organisms and is often one of the largest macromolecules in the cell (with bacterial genomes ranging from ~10 – 10,000 kbp). While DNA is often bound by histones or other DNA-binding proteins, there are a number of very important biological processes and biomedical and biotechnology advances that depend on the transport of naked DNA. Several important examples which have received much recent attention include nonviral gene delivery and antisense therapy, transfection and transformation, as well as DNA replication and transcription (80-82). Despite the complexity and significance of large naked DNA, there is a paucity of studies investigating how cellular crowding levels impact the mobility and configuration of large DNA molecules.

Here, we use single-molecule fluorescence microscopy and particle-tracking techniques to simultaneously characterize the diffusion and conformations of large double-stranded DNA molecules (11, 115 kbp) in 0-40% solutions of dextran (10, 500 kDa), a widely used inert crowder comparable in size to small proteins (83). For each case, we quantify mean squared displacements and corresponding diffusion coefficients and ergodicity of DNA motion. We simultaneously determine the degree of conformational state change of DNA upon crowding, as well as corresponding probability distributions and time-dependent fluctuations of states.

Varying experimental and simulation results have been reported regarding the diffusion of macromolecules within crowded environments. Diffusion measurements of small DNA fragments (< 4.5 kbp) in up to 40% Ficoll-70 (84) and the cytoplasm and nucleus of HeLa cells (85); large (48 kbp) DNA in dilute dextran solutions confined within a nanochannel (86); and apomyoglobin in RNAse and human serum albumin (87) have all reported normal Brownian motion where the mean squared displacement (MSD) can be used to calculate the diffusion coefficient via MSD = 2Dt. In contrast, several groups have found evidence of anomalous diffusion in crowded systems, where MSD ~ t^a with typical a values of 0.7 – 0.9 (i.e. subdiffusion) (16). Such anomalous behavior has been reported for aptoferrin in 500 kDa dextran (88), microspheres in cytoplasm (89), nanoparticles in dextran (90), and micron sized Cajal bodies in the nucleus of HeLa cells (91). Small single-stranded DNA in 10 kDa dextran solutions at cellular concentrations was also found to be subdiffusive ($a \geq 0.7$) (92).

While crowding is known to greatly impact the conformations of macromolecules, few studies have examined the effects of crowding on DNA conformation and have reported varying results. In crowded blends of DNA and polyethylene glycol, DNA has been shown to undergo compaction at low DNA concentrations and elongation and phase separation at high DNA concentrations (93, 94). Conversely, DNA molecules confined within nanogeometries and crowded by dextran have been shown to swell, elongate or compact depending on the confinement geometry, crowding level and ionic conditions (75, 86, 95). The time-dependence and

length scale of conformational state fluctuations within crowded environments remains unknown.

Thus, in comparison to their ubiquity and heavy biological significance, the effects of crowding on DNA are poorly understood. As such, our described experiments address important unanswered questions by elucidating the molecular level effects of cellular crowding on both the dynamics and configurational states of genome-sized DNA and the connection between center-of-mass mobility and conformational dynamics.

4.3 Materials and Methods

Double-stranded 11 and 115 kbp DNA, were prepared, as previously described (14), by replication of cloned plasmid (11 kbp) and bacterial artificial chromosome (115 kbp) constructs in E. coli, followed by extraction, purification, and restriction enzyme treatment to convert supercoiled constructs to linear form. For measurements, solutions of 10 kDa and 500 kDa dextran (Sigma) at concentrations of 0, 10, 20, 30, and 40% w/v were prepared in aqueous buffer (10 mM Tris-HCl (pH 8), 1 mM EDTA, 10 mM NaCl). Trace amounts of either 11 or 115 kbp DNA, uniformly labeled with YOYO-1 (Invitrogen), were mixed into dextran solutions, loaded into sample chambers, and equilibrated for ~30 minutes prior to measurements.

Using a high speed CCD QImaging camera on a Nikon Eclipse A1R inverted microscope, videos ranging from 5-60 seconds of DNA diffusing within dextran solutions were recorded at 10 frames/sec. Approximately ~150 – 300 DNA molecules

were recorded for each case. Custom written software (Matlab) was implemented to track the (i) center of mass position and (ii) major axis (R_{max}) and minor axis (R_{min}) vectors for each molecule (as described in Results). Tracked trajectories were then used to calculate all presented quantities (Figures 4.1 – 4.5). Error for MSDs and D values were calculated using the bootstrap method (96).

The zero-shear viscosity of dextran solutions of different concentrations were measured using optical tweezers microrheology as described previously (97). Briefly, microspheres of radius r = 4.5 mm embedded in dextran solutions were trapped and oscillated over a range of small amplitude frequencies (0.5 μm; 0.05 – 10.0 Hz) using an optical tweezers and piezoelectric microscope stage. Microspheres were coated with BSA to prevent nonspecific binding. Oscillation amplitudes and frequencies were low enough to ensure we were probing the near-equilibrium properties of the solution such that inhomogeneities in the flow field and depletion around the bead are negligible. The force *F* that the dextran solution exerts on the oscillating sphere was measured using a position-sensing detector that measures the deflection of the trapping laser during oscillation. The measured force on the sphere and speed *v* of the piezoelectric stage were used to determine the viscosity via Stokes drag ($F = 6\pi\eta r v$ where η is the solution viscosity). Further instrumentation and methods details are fully described and justified in Refs (97) and (98). Some of the higher concentration viscosities exhibit modest frequency dependence (shear thinning) at higher frequencies, but all solutions reach a low frequency plateau (see Figure 4.7). We

determine the zero-shear viscosity from this low frequency plateau value of viscosity. Measured viscosities are presented in Figure 4.7.

4.4 Results and Discussion

4.4.1 Diffusion

We have imaged single, fluorescent-labeled DNA molecules diffusing in dextran solutions of concentrations, C, comparable to cellular conditions (C = 0 – 40 (% w/v)). We tracked the center of mass positions of ~150-300 diffusing DNA in time to quantify the mean squared displacements (MSD) for each case (Figure 4.1). For each MSD, we evaluate a, where MSD ~ t^a, and, as expected, for DNA diffusing in the absence of crowders (C = 0), we find purely linear behavior (i.e. classical Brownian motion) for all measured timescales (0-10 s and 10-50 s). We also find a ~ 1 for DNA diffusing in 10 kDa dextran (Sd) for all DNA lengths, crowding concentrations and timescales. Conversely, 0-10 s MSDs for both DNA constructs in 500 kDa dextran (Ld) solutions exhibit weakly anomalous mobility with a values of ~0.66±0.05 – 0.87±0.06, decreasing slightly with increasing C (Figure 4.1A). Our results suggest that the crowder size, rather than DNA size, plays the key role in the emergence of subdiffusive dynamics.

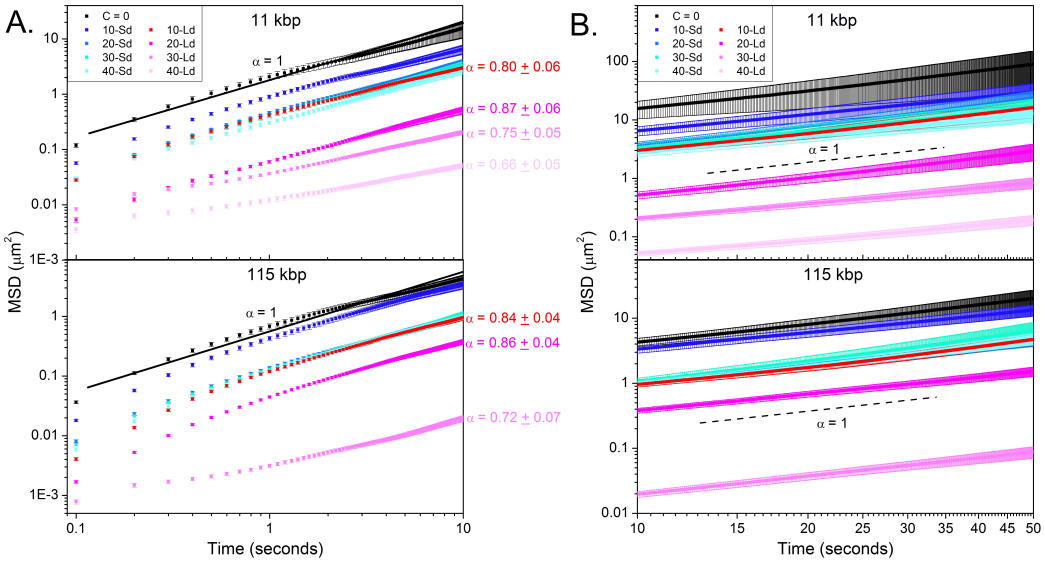

Figure 4.1 Mean squared displacements vs. time for both the 11 kbp (top) and 115 kbp (bottom) DNA diffusing in both 10 kDa (Sd) and 500 kDa (Ld) dextran from (A) 0-10 seconds and (B) 10-50 seconds. The concentration, C, and crowder size (Sd or Ld) for each MSD is indicated in the legend. (A) All MSDs are fit to a power law MSD ~t^{α}. $\alpha = 1$ scaling (black line), which demonstrates classical Brownian motion, is added for convenience. For cases that display sublinear scaling, α values are listed to the right of the MSD in the corresponding color. MSDs without a listed α value display linear scaling. As seen in B for long timescales, α approaches unity for all cases.

Multiple models have been proposed to explain the source of anomalous subdiffusion within crowded environments, with the two most widely invoked being the continuous time random walk (CTRW) and fractional Brownian motion (FBM) models (88, 99-101). CTRW is built around a non-Gaussian propagator, and reveals distinctly non-ergodic behavior, where time averaged MSDs differ from ensemble averaged MSDs (99). FBM, on the other hand, is completely ergodic with diffusion driven by a stationary Gaussian process (16, 99). Thus, to determine which model

describes our weakly anomalous behavior, we test the ergodicity of the DNA diffusion by evaluating the two most robust ergodicity breaking parameters (101): $EB(t) = \frac{\langle\overline{\delta^2(t)}\rangle}{\langle x^2(t)\rangle}$ and the non-Gaussianity parameter, $G(t) = \frac{1}{2}\frac{\langle\overline{\delta^4(t)}\rangle}{\langle\overline{\delta^2(t)}\rangle^2} - 1$, where $\langle x^2(t)\rangle$ is the MSD and $\langle\overline{\delta^2(t)}\rangle$ is the time-averaged MSD. For a purely Gaussian ergodic process EB = 1 and G → 0 for sufficiently long times. For all data sets measured, we find that G goes to zero and EB ~ 1 (Figure 4.2). Thus our results show that large DNA diffusion is best modelled by FBM, which is a Gaussian stationary process. We note that obstructed diffusion is another potential ergodic process that has been proposed for crowded environments (16), but this model is based on immobile crowders. Thus, obstructed diffusion should only explain cases in which the diffusion timescale of the crowders is much slower than that of the diffusing molecule, whereas in our experiments the crowders are much more mobile than the DNA itself. The radii of gyration of Sd and Ld are R_g = 3.5 nm and 19 nm, respectively (86), as compared to our DNA which have R_g = 0.2 and 1.0 mm for the 11 kbp and 115 kbp DNA (63). Using our measured viscosities of the different dextran solutions we can calculate the diffusion coefficients for dextran via $D = k_bT/6\pi\eta R_g$ and compare to those of our DNA (see Figure 4.3B). As seen in Figure 4.3B, even Ld diffuses >10x times faster than the 11 kbp DNA, and in most cases dextran is diffusing ~100x times faster. Thus, dextran behaves as a relatively mobile crowder compared to the timescale of DNA mobility. Finally, another possible explanation for our measured subdiffusion is that the DNA is trapped in minima surrounded by the crowders, which would have to collectively move before DNA can diffuse (102, 103). However, the studies that have reported this

source of subdiffusion also find that the trapped polymer undergoes compaction. In our conformational analysis (described in the Conformation Section below) we see no signs of compaction rather we observe polymer elongation, so we believe that this explanation is likely not valid for our experimental parameters.

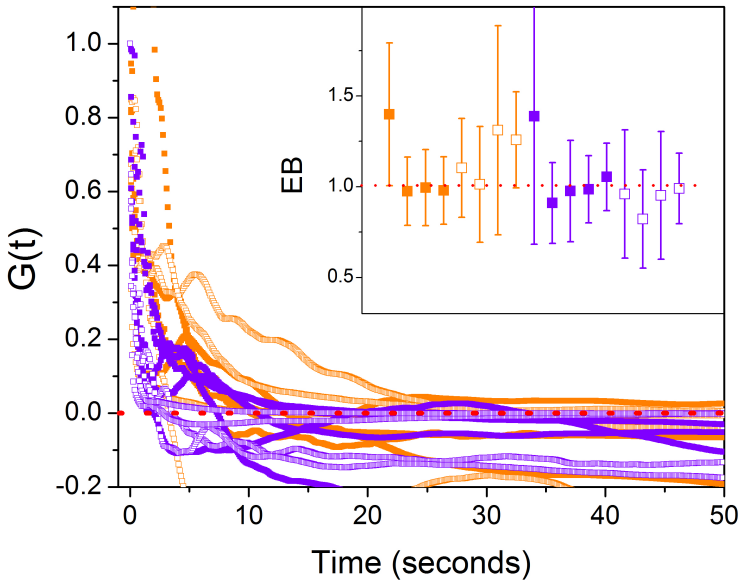

Figure 4.2 Non-Gaussianity parameter, G vs. time for 11 kbp (purple) and 115 kbp (orange) DNA diffusing in 10 kDa (open squares) and 500 kDa (closed squares) dextran. Note G tends to zero (dashed line), indicating an ergodic diffusion process. Inset shows calculated ergodicity-breaking term (EB) for each crowding case. EB = 1 (dashed line) indicates ergodic behavior. See text for definitions of G and EB.

Crowding-induced subdiffusion is predicted to only be apparent at intermediate timescales and approach normal diffusion on long time scales (16). Using this prediction, coupled with the weak nature and ergodicity of the subdiffusion, we

approximate our MSDs in Ld at long times (10-50 s; Figure 4.1B) as linear in order to extract diffusion coefficients D and compare to D values found in Sd (Figure 4.3). Importantly, a values determined from these long-time tails of the MSDs are all indistinguishable from unity within the experimental error, demonstrating the accuracy of the reported D values (Figure 4.1B).

We find that the reduction of D from the C=0 case (D_0), as concentration of either crowder increases, is nearly identical for both DNA lengths; however, the concentration dependence of D/D_0 is starkly different in Sd vs Ld, once again demonstrating that DNA mobility is driven by crowder size rather than DNA size. We note that a reduction in mobility with increasing concentration is not entirely surprising, and could in fact simply be due to the increasing viscosity of the Ld and Sd solutions with increasing concentration via the Stokes-Einstein relation $D \sim \eta^{-1}$. To separate the effect of increasing viscosity with dextran concentration from our measured mobility reduction we compare D/D_0 to η_0/η (Figure 4.3A). As seen is Figure 4.3A, we find that crowding-induced mobility reduction is distinctly different than that due simply to increasing viscosity. We find that the DNA mobility is actually enhanced compared to that expected from Stokes-Einstein dynamics. This enhanced mobility takes effect immediately at the onset of crowding (C = 10) with the DNA exhibiting a mobility ~10x faster than its corresponding Stokes-Einstein mobility. This effect can also be seen by comparing dextran diffusion coefficients D_{dex} to that of DNA (Figure 4.3B). If the DNA mobility reduction were purely viscosity-dependent then D_{dex}/D_{DNA} would remain constant for all concentrations. However, as seen in

Figure 3B, this ratio initially drops an order of magnitude (enhanced DNA mobility) then remains fairly constant with a modest increase for Ld solutions and decrease for Sd solutions as C increases. We can understand this enhanced mobility as arising from the corresponding conformational change of the DNA that we observe at the onset of crowding (see Conformation section). The DNA undergoes a conformational change to facilitate transport through the crowded solution. Note that both the relative mobility enhancement and the conformational change appear at the onset of crowding and remain relatively unchanged as the crowding increases.

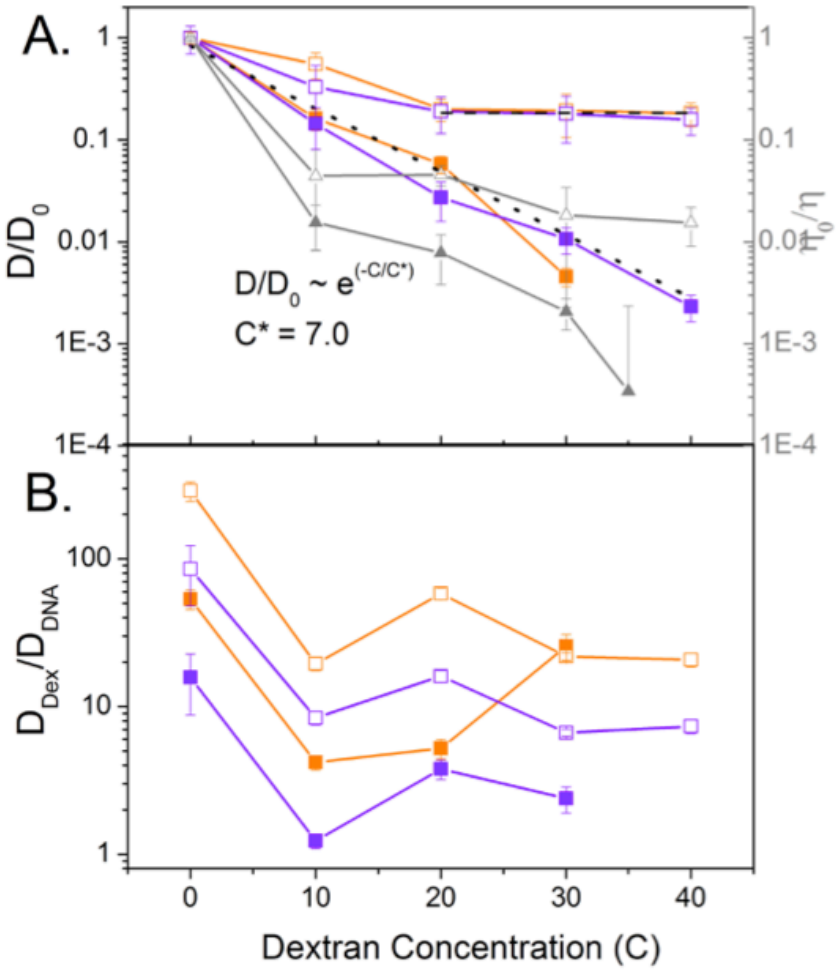

Figure 4.3 (A) Normalized DNA diffusion coefficients, D/D_0, and inverse normalized dextran solution viscosities, η_0/η, vs. dextran concentration C for DNA diffusing in dextran solutions. Color and symbol scheme is as in Figure 4.2, with inverse viscosity shown in gray. The reduction in D from C = 0 (D_0) appears independent of DNA length with the crowder length playing a dominating role. Note the surprising saturating effect for 10 kDa dextran data with negligible change in D/D_0 for C > 20 (horizontal dashed line). Conversely, in 500 kDa, D/D_0 displays exponential scaling with C. From the exponential fit (dashed line) we find a critical crowding concentration of C* ~7.0. (B) Ratio of dextran vs DNA diffusion coefficients for each crowding case (same color/symbol scheme as A).

We find that in Sd, DNA mobility is reduced ~5x from C = 0 to 20 compared to the ~20x increase in viscosity; however, surprisingly, for C > 20, a saturating effect is observed as D/D_0 remains nearly constant for both lengths of DNA while the viscosity increases ~3x more. To the best of our knowledge, this is the first time such a saturating effect has been reported for diffusion in a crowded system. We note that this result appears counterintuitive according to the Stokes-Einstein relation $D \sim \eta^{-1}$, and given the error in our measured D values, it is possible that the mobility is actually decreasing with increasing C, albeit with a weak dependence that is immeasurable within our experimental error. We interpret this result as arising from the change in conformational dynamics of the DNA that we observe upon crowding as detailed in the following Conformation section. The change in DNA conformation and the associated fluctuations would directly impact the COM diffusion, and could lead to enhanced mobility as compared to that due to fluid viscosity as described above.

Conversely, in Ld, we find D/D_0 for both DNA constructs decreases exponentially up to the highest C values, dropping by ~300x, though still significantly enhanced in comparison to the ~3000x increase in viscosity.. By fitting the data to an exponential of the form $D/D_0 \sim \exp(-C/C^*)$, we find a critical crowding concentration of C* = 7.0%. As the mobility reduction deviates from the viscosity relation at ~C* we can interpret our measured critical crowding concentration as quantifying the concentration at which crowding induces breakdown of Stokes-Einstein mobility of DNA. Further, the concentration at which we begin to observe weak subdiffusion in Ld is ~2C*, once again demonstrating that the dependence of diffusion on crowding

concentration cannot be explained by Stokes-Einstein fluid effects. Similar results, namely DNA-independent mobility reduction and exponential dependence on C have been reported for shorter DNA (<4.5 kbp) in Ficoll-70 (84).

The significant difference in diffusive dynamics of DNA between Sd and Ld cases can be understood by noting the significant difference in mobility of the two crowders (Figure 4.3). While highly mobile crowders (i.e. Sd is ~60x and ~300x more mobile than 11 and 115 kbp DNA) contribute to reduced mobility, this effect alone cannot explain the extreme mobility reduction seen with Ld and in many other crowded systems (84, 89, 92).

Interestingly, our results are distinctly different from our previous diffusion results for semidilute and concentrated solutions of large DNA (13, 104) which show power law dependence on solution concentration as well as a strong dependence on DNA length in line with classical Doi-Edwards polymer theory (1). Further, we previously found no evidence of subdiffusion despite the fact that actual D values were comparable in magnitude to those measured in this study. This sharp contrast indicates that crowded systems, comprised of molecules with different sizes and structures have unique and complex dynamics not explained by classical theory for concentrated homogenous polymer solutions.

4.4.2 Conformation

To further elucidate the effects of crowding on DNA, we investigated the conformational changes induced by Sd and Ld. During measurements, we commonly observed an unexpected elongation of DNA relative to the dilute case (C = 0), where DNA assumes a roughly spherical random coil conformation (Figure 4.4 insets, Figure 4.5A). To quantify this elongation, which was most apparent for 115 kbp DNA in Ld, we use custom written software (Matlab), to quantify a major (R_{max}) and minor (R_{min}) axis (Figure 4.4 insets) of each DNA molecule for all recorded frames. The method we use, which defines an outline of the molecule is similar to that of calculating the radius of gyration tensor for each conformation (105). From our measured major and minor axes, we define an elongation parameter, $E = (R_{max}/R_{min}) - 1$, to quantify the elongation relative to the random coil state. We find that the probability distribution of elongation states P_E is well fit to a gamma distribution, $P_E(k,\theta) = \frac{\theta^{-k}}{\Gamma(k)} E^{k-1} e^{\frac{-E}{\theta}}$, where k is the shape term and q is a measure of the distribution width (Figure 4.4). Gamma distributions have also recently been shown to describe the dynamics of several biological processes dominated by Brownian motion (106, 107).

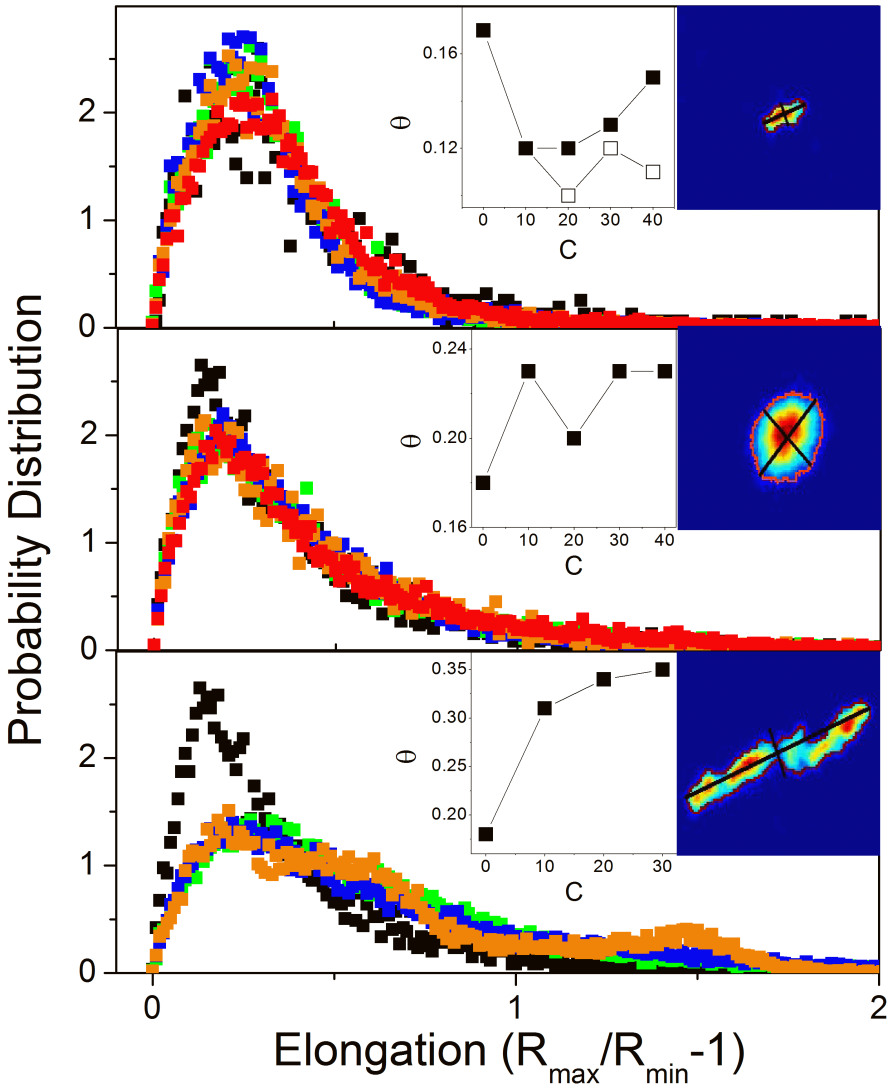

Figure 4.4 Probability distributions for elongation parameter E for 11 kbp DNA in 500 kDa dextran (top), 115 kbp DNA in 10 kDa dextran (middle), and 115 kbp DNA in 500 kDa dextran (bottom). Distributions for C = 0 (black), 10 (green), 20 (blue), 30 (orange), and 40 (red) are shown. Right insets show recorded images of typical DNA conformations when crowded with DNA outline and major (R_{max}) and minor (R_{min}) axes used to calculate E (scale of each inset is $(10\mu m)^2$). Left insets show the gamma distribution width parameter (θ) vs. C. For 115 kbp DNA, this width is lowest for C = 0 while for 11 kbp DNA, θ at C = 0 is highest. The distribution for 11 kbp DNA in 10 kDa dextran (not shown) is nearly identical to that in 500 kDa dextran (top). θ values for this case are shown (open squares) in the top inset.

For 115 kbp DNA in Ld, we see a ~67% increase in the average elongation coupled with a distribution widening of q ≈ 0.37 for C = 0 to q ≈ 0.62 for all crowding levels. Similar behavior (C-independent elongation and distribution widening) is seen for 115 kbp DNA in Sd, however less pronounced. Interestingly, while we find modest elongation for the 11 kbp DNA (similar to 115 kbp DNA in Sd), the distribution width q actually decreases with the addition of dextran (Figure 4.4 inset). Of note is the saturation effect of elongation for both DNAs, as the initial addition of dextran (C = 10) causes an increase in the average elongation and change in distribution width but this distribution remains relatively unchanged up to the highest concentration (Figure 4.4). Elongation has only previously been reported for crowded DNA when confined in nanogeometries (86, 95) or in conjunction with large-scale phase separation (94) at high salt conditions.

We also sought to determine whether the elongation distributions arise from an ensemble of individual molecules, each with relatively fixed elongation states that varied from molecule to molecule, or from individual molecules (all in similar states) fluctuating between elongation states in time. Thus, to evaluate the time dependence of elongation, we define a fluctuation length, $L(t) = \langle |R_{max}(0) - R_{max}(t)| \rangle$, which quantifies how quickly the conformational state of a molecule is changing and the length scale of elongation fluctuations. Figure 4.5A, depicting the physical interpretation of L(t), demonstrates that for very short times L(t) is nearly zero as the DNA has not had time to alter its conformation. As t increases, the conformation changes more apparently. For long times, L(t) approximately plateaus to a near steady

state terminal value, L_p (Figure 4.5B). We can understand this terminal value as the length scale of conformational "breathing" between different states. By fitting L(t) to a single exponential we quantify a decay rate, b, for conformational breathing, or the rate at which elongation states become decorrelated from one another (Figure 4.5 insets). As expected, the decay rate of fluctuations is largest for C = 0 for all cases, indicating more rapid conformational fluctuations, which is then slowed, as DNA center-of-mass mobility is reduced by the addition of crowders. Interestingly, we see once again a saturating effect with b decreasing upon initial crowding but remaining relatively unchanged for C = 10 – 40 for all DNA and crowder sizes, corroborating our elongation state distribution results. We are aware of no previously reported direct measure of the dynamics associated with crowding-induced conformational change. We note that a more conventional measure of correlations would be the autocorrelation function of the major axis in time, i.e. $\langle R(0)R(t)\rangle$. While this autocorrelation can provide the timescale of decorrelation, similar to our measured decay rate, it does not provide a straightforward measure of the breathing length scale. Nonetheless, we calculate the autocorrelation of elongation states and find a similar decay rate (see Figure 4.6), further validating our defined elongation fluctuation length parameter.

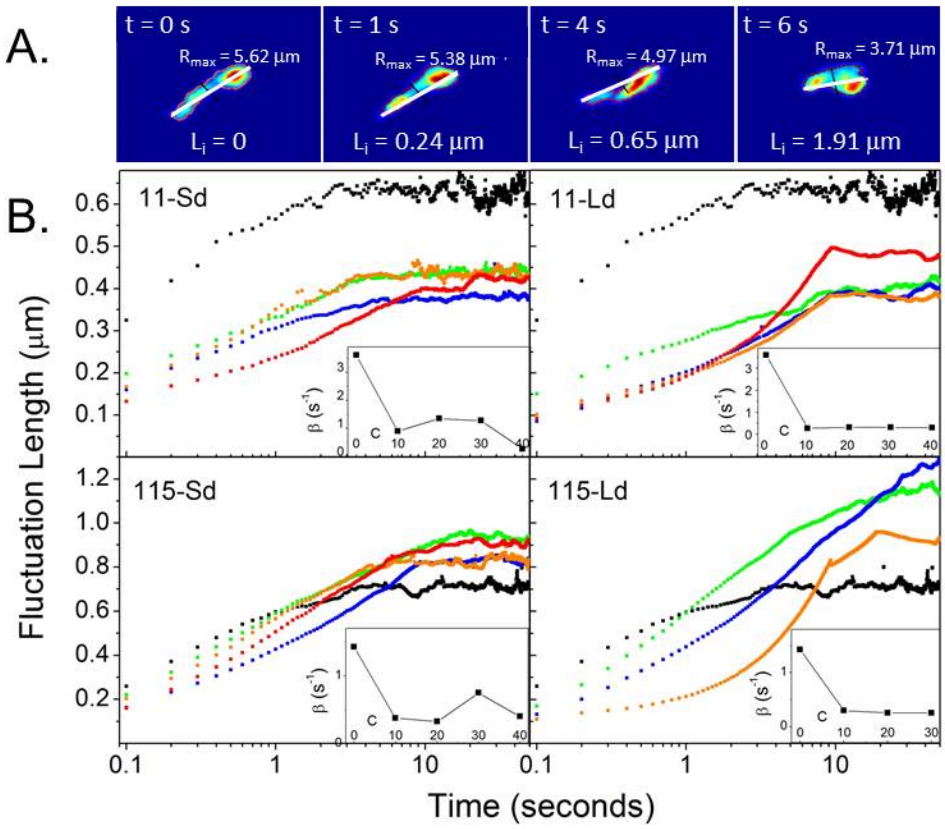

Figure 4.5 (A) Measured major axis, R_{max}, (white line) and minor axis, R_{min}, (black line) for a typical 115 kbp DNA molecule diffusing in Ld (C = 20) with increasing time. The fluctuation length for the displayed molecule, L_i, is noted for each frame. (B) Ensemble averaged fluctuation length, L, vs. time for 11 kbp DNA in 10 kDa dextran (11-Sd), 11 kbp DNA in 500 kDa dextran (11-Ld), 115 kbp DNA in 10 kDa dextran (115-Sd), and 115 kbp DNA in 500 kDa dextran (115-Ld). Color scheme is the same as in Figure 4.4. Fluctuation lengths are all fit to single exponentials with decay rates β shown in the insets. The decay rate for C = 0 is highest for all cases, as expected; however, it remains relatively unchanged as C increases beyond 10. Also note that the terminal fluctuation length, ~0.7 µm for both DNAs at C = 0, increases ~46% for 115 kbp DNA upon crowding but actually decreases ~40% for 11 kbp DNA

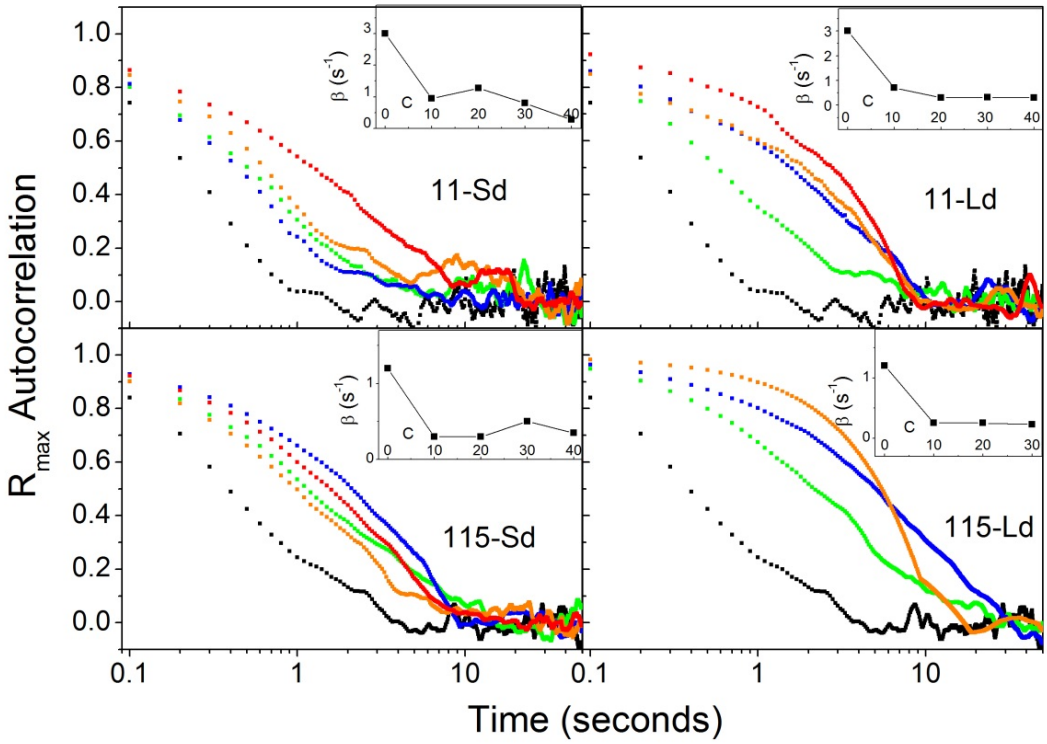

Figure 4.6 Normalized R_{max} autocorrelation ($\langle R_{max}(0)R_{max}(t)\rangle/(R_{max}(0))^2$ vs. time for 11 kbp (top) and 115 kbp (bottom) DNA. Color scheme is the same as in Figures 4.4 and 6.5. Autocorrelation data for all cases were well fit to an exponential decay, with the corresponding decay rates, b, vs. dextran concentration C, shown as insets for each plot. Note that the values and trends of the decay rates are nearly identical to the corresponding fluctuation length decay rates (see Figure 4.5B).

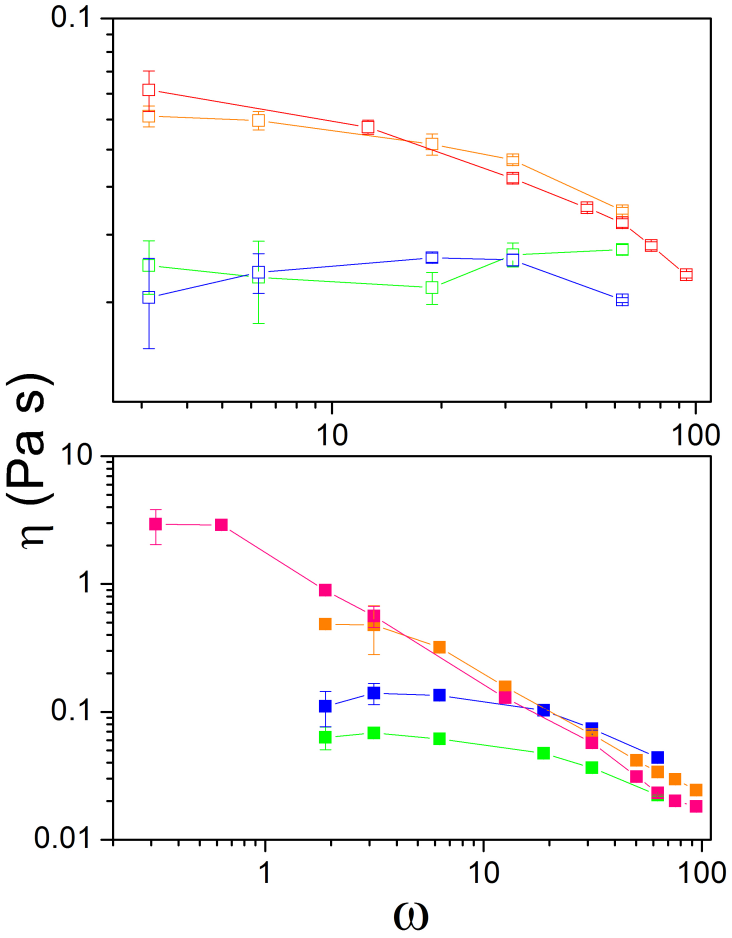

Figure 4.7 Dextran viscosity, η, vs oscillation frequency, w, for concentrations C = 0 - 40 for (A) Sd and (B) Ld. Color scheme is the same as in Figure 4, with the additional pink squares representing C = 35. Viscosity values are measured via optical tweezers oscillatory microrheology as described in Methods and in Refs 97 and 98. Briefly, microspheres embedded in dextran solutions are trapped using optical tweezers and oscillated over a range of frequencies, w, at an amplitude of 0.5 mm. An approximate frequency-independent plateau can be seen for all concentrations at low w. This low-frequency plateau viscosity provides a reliable estimate of the zero-shear viscosity of each solution. This plateau regime is also indicative of the frequency range over which the solution is behaving as a purely viscous fluid.

For the 115 kbp DNA, both in Sd and Ld, we find that the terminal fluctuation length, L_p, (~0.7 mm for C = 0) increases ~43% to ~1.0 mm for C > 0, indicating that the crowders are inducing larger, slower fluctuations. This result is in agreement with our elongation distribution data for 115 kbp DNA, where we indeed see an increased width in the gamma distribution for C > 0 relative to C = 0. Interestingly, for 11 kbp in both Sd and Ld, L_p actually decreases ~40% upon crowding (from $L_p \approx 0.7$ mm at C = 0 to ~0.40 mm for C > 0), corroborated by the reduced width in elongation distribution upon crowding (Figure 4.4). Thus our findings demonstrate a novel crowding-induced molecular elongation mechanism dominated by DNA size with crowder size also playing a role.

Naively, crowding-induced DNA elongation is counterintuitive as the highest entropy state for DNA in solution is a random coil conformation. However, crowding-induced ordering of macromolecules is a well-known entropic effect, the depletion interaction, driven by entropy maximization of the crowders, which are much greater in number than the diffusing macromolecule of interest. The depletion interaction, whereby the crowders seek to increase their accessible volume and thus entropy, is responsible for a wide range of biochemical processes including enhanced protein folding and increased enzymatic reaction rates and DNA melting temperatures. When in a random coil the spherical space taken up by the DNA is excluded from the dextran which creates an effective osmotic pressure inward on the coil. While such pressure could lead to compaction at high enough salt concentrations, the electrostatic repulsion of neighboring DNA segments prevents full compaction without high salt,

so the DNA instead elongates to reduce the excluded volume. For reference, the volume taken up by a 115 kbp random coil with R_g = 1 mm is ~1 mm^3 compared to a volume of ~$1x10^{-4}$ mm^3 (~$(2nm)^2$ x 30 mm) for fully extended 115 kbp DNA. We see less pronounced elongation for Sd as these crowders are small enough that they could partially penetrate the random coil configuration thereby lowering the osmotic pressure difference. While we see reduced elongation for 11 kbp DNA we find that the width of the distribution of states is lowered along with the terminal fluctuation length. Both effects, signatures of increased order, reflect an alternative entropy minimizing induced in 11 kbp DNA by the crowders. Conversely, for 115 kbp DNA, because the elongation, and corresponding entropy drop, is much more extreme, it compensates partially by an increased width of distribution states and terminal fluctuation length.

While crowding-induced changes in molecular conformation are often explained in terms of entropic effects, as described above, crowding molecules can also affect the enthalpic contributions to the free energy change of the molecule from changing conformation. The most relevant enthalpic effect in our case would be due to preferential hydration of the crowder (which would modulate the solvent quality). Several recent studies have investigated the entropic and enthalpic contributions of different crowders on the stability and aggregation of various proteins and nucleic acids, with varying and often conflicting results (108, 109). However, the overwhelming majority of studies using dextran as a crowder have shown that the entropic excluded volume effect dominates the crowding-induced free energy change

(108-112). Further, a very recent study examining crowding-induced protein aggregation (109) has shown that flexible, inert, hydrophilic polysaccharides (such as dextran) influence the conformational free energy solely via excluded volume interactions. Interestingly, this same study shows that the effect of dextran-crowding is not proportional to the solution viscosity, in line with our diffusion results. While one recent experiment (113) reported that the crowding-induced stabilization of the protein ubiquitin by dextran is largely caused by enthalpic rather than entropic effects, this enthalpy-driven stabilization is shown to be independent of the size of the dextran (comparing polymeric to monomeric dextran) and to rely solely on the chemical structure (as expected for an enthalpy driven process). Conversely, our data show that the size of the dextran plays an important role in the conformational fluctuations of DNA. As crowder size plays a key role in entropically-driven processes, our results suggest that entropy rather than enthalpy is indeed the driving force underlying the crowding-induced conformational change of DNA, in line with reported results for conformational changes in proteins.

Surprisingly, despite the initial conformational change induced by the addition of crowders, we see little change in elongation, width distribution or fluctuation time and length-scale as the crowder level is increased from C = ~10 – 40. We see a similar saturating effect for DNA diffusion in Sd, which we attribute to the mobility of Sd as compared to Ld and to the DNA itself. Thus, we can understand the initial mobility reduction and elongation/ordering of the DNA induced by the addition of crowders as driven by entropic depletion effects. However, because dextran is much more mobile

than DNA, the DNA is still subject to rapid thermal kicks from the crowders and rapidly changing “available” space to fluctuate within, which counteracts the slowing and elongation driven by entropy maximization of the crowders. As Ld is ~6x slower than Sd, the enhanced elongation in Ld is due to less rapid thermal kicks and rearranging. This reduced mobility also leads to a greater DNA mobility reduction, which is coupled with an exponential dependence of mobility on crowding level and subdiffusive behavior.

4.5 Conclusion

We have used single-molecule imaging and particle-tracking techniques to simultaneously track molecular diffusion and conformation of large genome-sized DNA in crowded environments that mimic cellular crowding conditions. Despite the essential role that mobility and configuration play in DNA function in the cell, relatively few studies have investigated the effects of crowding on large DNA and no previous studies have experimentally measured both center-of-mass mobility and conformational dynamics to elucidate the connection between the two. We determine the linearity and ergodicity of DNA MSDs and quantify both the probability distributions of DNA elongation states as well as elongation fluctuation time and length scales.

While DNA displays ergodic Brownian motion for all crowding cases, we find that underlying diffusive mechanisms of large DNA are driven by the size and mobility of the crowder rather than the DNA itself. For smaller crowders we find

classical linear scaling of the MSD with time, which is linked to a novel saturation effect whereby increased levels of crowding beyond ~20% have negligible effect on DNA diffusion due to the high crowder mobility counteracting the entropic depletion effect restricting DNA conformation and diffusion. Reduced DNA elongation in smaller crowders coupled with a similar unique saturation effect of elongation state distributions and fluctuation timescales further supports this result. In contrast, DNA diffusion in large crowders displays exponential mobility reduction with crowder concentration up to ~300x at 40%, which is coupled with weak subdiffusive dynamics, with $a \approx 0.7 - 0.9$, demonstrating that the fractional Brownian motion model for macromolecular diffusion in crowded environments well explains the diffusion of large DNA amongst crowders that are ≤50x smaller and more mobile than the DNA itself.

While DNA size plays a minimal role in diffusion, it dominates elongation dynamics. Both DNA constructs exhibit elongation and slower state fluctuations upon crowding with elongation probabilities that are gamma distributed and show minimal dependence on crowder concentration. However, 115 kbp DNA displays elongation distribution widths and fluctuation lengths that increase upon crowding, in contrast to 11 kbp DNA in which these parameters actually decrease. Both effects are signatures of the reduced DNA entropy induced by the depletion effect of the surrounding crowders.

Our collective results, which reveal important new insights into the complex effects of cellular crowding on large DNA, are critical to a wide range of open

questions and problems debated by researchers in biology, physics, chemistry, engineering, materials science and medicine, including understanding important biological processes, developing new drug delivery and gene therapy techniques, fabricating synthetic cells, and designing novel biomaterials.

4.6 Acknowledgments

Chapter 4, in full, is a reprint of the material as it appears in Biophysical Journal. Chapman CD, Gorczyca S, & Robertson-Anderson RM (2015) Crowding Induces Complex Ergodic Diffusion and Dynamic Elongation of Large DNA Molecules. *Biophysical journal*, *108*(5):1220-1228. The dissertation author was the primary investigator and author of this paper.

Chapter 5

Onset of Non-Continuum Effects in Microrheology of Entangled Polymer Solutions

5.1 Abstract

Microrheology has emerged as a powerful approach for elucidating mechanical properties of soft materials and complex fluids, especially biomaterials. In this technique, embedded microspheres are used to determine viscoelastic properties via generalized Stokes-Einstein relations, which assume the material behaves as a homogeneous continuum on the length scale of the probe. However, this condition can be violated if macromolecular systems form characteristic length scales that are larger than the probe size. Here we report observations of the onset of this effect in DNA solutions. We use microspheres driven with optical tweezers to determine the frequency dependence of the linear elastic and viscous moduli and their dependence on probe radius and DNA length. For well-entangled DNA we find that the threshold probe radius yielding continuum behavior is ~3x the reptation tube diameter, consistent with recent theoretical predictions. Notably, this threshold is significantly larger than the mesh size of the polymer network, and larger than typical probe sizes used in microrheology studies.

5.2 Introduction

Polymeric fluids and soft matter, ubiquitous in nature and industry alike, display complex and intriguing mechanical properties. As such, numerous studies have been devoted to understanding their stress-strain relationships (1, 5, 114, 115); however, many unanswered questions remain. In standard rheology studies macroscopic strains are applied and bulk induced stress is measured to quantify the frequency dependence of elastic and viscous responses. In contrast, microrheology uses embedded microspheres, either diffusing passively or driven by magnetic or optical tweezers, to probe mechanical properties at the microscale (20, 116-128). Microrheology has emerged as a powerful complimentary approach to standard macrorheology, and has many advantages, including small sample sizes, small applied strains (important for fragile biomaterials), and the ability to detect microscale heterogeneities and fluctuations (20, 129).

In microrheology studies, measurements of microsphere motion are interpreted to deduce viscoelastic moduli via generalized Stokes-Einstein relations (126). Theoretically, such an analysis should yield accurate determinations of macroscopic material properties provided the material behaves as a near-equilibrium, homogeneous, isotropic continuum on the size scale of the probing microsphere. It is widely accepted that when polymers overlap to form a transient mesh the embedded probe should be chosen to be larger than the characteristic mesh size to access macroscopic rheological properties. Alternatively, probes smaller than the mesh size can and have been used to determine microscale structures and heterogeneities present

in polymer systems (20, 127, 128). Several recent experiments have employed passive nanoparticle tracking to examine both microscale and macroscale properties of flexible synthetic polymers, such as polyethylene oxide (PEO), polyethylene glycol (PEG), and polystyrene (PS) (20, 21, 130-132). Studies with polyethylene oxide found results independent of probe size for probe diameters of 0.46 – 2 μm (all larger than the mesh size, polymer radius of gyration, and entanglement correlation length), suggesting the continuum limit is valid (130, 132). Further, studies of entangled PS, employing nanoparticles smaller than the polymer mesh size (as well as the radius of gyration and entanglement correlation length), measured anomalous diffusion rates much faster than those predicted by the Stokes-Einstein relation, demonstrating a breakdown of the continuum limit (20, 21). In contrast, recent findings for semi-dilute PEG suggest that the polymer radius of gyration, rather than the mesh size, is the threshold probe size for reaching the continuum limit (131). For entangled polymers, several theoretical studies regarding the diffusion of spherical nanoparticles predict that the threshold probe radius, R, is the reptation tube diameter, d_T (133-135). Recently, Yamamoto and Schweizer (135) used a statistical dynamics approach to build on these predictions and show that $R = d_T$ is not actually sufficient for the continuum limit; rather the probe must be several times larger than the tube diameter, predicting a threshold criterion of $R \approx 5d_T$. Despite the widespread use of passive microrheology techniques to probe polymer systems (20, 127, 128, 131, 136), this predicted crossover length scale has yet to be experimentally validated.

Compared to typical synthetic polymers, considerably larger length scales are encountered in biopolymer systems. For example, semi-flexible actin filaments with persistence lengths of ~17 μm have been extensively studied by microrheology (117, 137-141), and evidence of non-continuum effects (such as free diffusion and cage-hopping) has been reported for probe sizes similar to the mesh size (120, 126, 139, 142-145). However, the transition from the non-continuum to the continuum regime, critical to understanding the microscopic nature of viscoelastic behavior in polymer systems, has not been characterized. The nature of such a transition also likely differs for more flexible biopolymers such as long DNA molecules in which the persistence length (≈ 50 nm) is significantly smaller than the polymer length (~1 – 50 mm). In contrast to actin, relatively few microrheology studies of DNA have been carried out, and most have been in the semi-dilute or marginally entangled regime (121, 146-149). Probe sizes used in the reported studies were larger than the DNA mesh size and non-continuum effects were not observed, indicating that the probes were sufficiently large to detect macroscopic properties. Thus, for entangled flexible polymers, the point of onset of non-continuum effects has not been observed.

Here, we report studies of the transition from the continuum to non-continuum regime in microrheology measurements with DNA, and the dependence on probe size and DNA length, including lengths longer than studied previously. We identify a threshold probe radius of ~$3d_T$ for entangled DNA, consistent with recent theoretical predictions (135). For DNA, a model for flexible polymers in general, this threshold

is significantly larger than the mesh size and typical probe sizes used in microrheology studies.

We used an active microrheology technique in which an optically trapped microsphere is driven sinusoidally at varying frequencies through DNA solutions while the resisting force is measured (117, 119). From these measurements we determined the storage modulus, $G'(\omega)$, which characterizes the elastic response, the loss modulus, $G''(\omega)$, which characterizes the viscous response, and the complex viscosity, $h^*(\omega)$, which is the ratio of complex modulus to frequency. We studied linear double-stranded DNA lengths of 11 kbp, 45 kbp, and 115 kbp at 1.0 mg/ml, which span the range from the unentangled to well-entangled regime with concentrations corresponding to $0.8c_e$, $2c_e$, and $4c_e$, respectively, where c_e is the critical concentration for entanglements (previously determined to be ~6x the polymer coil overlap concentration) (2). The mesh size for all three samples remains fixed (~100 nm), however the number of entanglements per molecule (n) increases with molecular length. Microspheres with radii of 1, 2.25, and 3 μm, all much larger than the DNA mesh size, were tested.

5.3 Experimental Section

Three double-stranded DNA constructs, an 11 kbp (3.7 μm) plasmid, a 45 kbp (15 μm) fosmid, and a 115 kbp (39 μm) bacterial artificial chromosome were prepared by replication of cloned constructs in E. coli, followed by extraction and purification. One-cutter restriction enzymes, BamH1 (for 11 kbp), ApaI (45 kbp), and MluI (115

kbp), were used to convert the supercoiled constructs to linear form. These protocols have been thoroughly described previously (13, 14). For measurements, DNA solutions were prepared in aqueous buffer (10 mM Tris-HCl (pH 8), 1 mM EDTA, 10 mM NaCl) at a concentration of 1.0 mg/ml. Microspheres, with radii of 1, 2.25, and 3 μm (Polysciences), were coated with Alexa-Fluor-488 BSA (Invitrogen) to prevent nonspecific binding and to visualize the microspheres. Trace amounts of coated microspheres were mixed with the prepared DNA solutions and the solution was equilibrated for ~30 minutes prior to measurements.

A custom-built force-measuring optical trap, formed by a 1064 nm Nd:YAG DPSS laser (CrystaLaser) focused with a 60X 1.4 NA objective (Olympus), was used to capture individual microspheres within the sample chamber. The DNA solutions were displaced relative to the fixed trap using a piezoelectric nano-positioning stage (Mad City Labs) to apply a sinusoidal oscillation. A position-sensing detector (Pacific Silicon Sensors) measured the trapping laser deflection, which is proportional to the force acting on the trapped microsphere. The trap was calibrated using Stokes drag for a microsphere oscillating in water. The oscillation amplitude was chosen to be 0.52 μm as this was found to be sufficiently large to obtain a clear signal while being small enough that the response was not amplitude dependent (in the near-equilibrium regime of material response).

As depicted in Figure 5.1, force measurements for individual trials were each fit to a sine curve using the least squares method. The resulting fit for each force trace and the recorded stage position are used to calculate the storage modulus, $G'(\omega) =$

$[|F_{max}|/(|x_{stage}|6\pi R)]cos(\Delta\varphi)$, loss modulus, $G''(\omega) = [|F_{max}|/(|x_{stage}|6\pi R)]sin(\Delta\varphi)$, and complex viscosity, $\eta^*(\omega) = [(G'(\omega)/\omega)^2 + (G''(\omega)/\omega)^2]^{1/2}$, as described previously (117), where $|F_{max}|$ is amplitude of measured force, $|x_{stage}|$ is stage amplitude, and $\Delta\varphi$ is phase difference between stage position and recorded force signal. Ten trials, each an average of ten full oscillations, were completed for each frequency, with a new microsphere captured in a different region of the sample chamber for each trial. Average and standard deviation of $G'(\omega)$, $G''(\omega)$, and $\eta^*(\omega)$ for the ten individual trials give the plotted values and error bars, respectively, for each frequency shown in Figures 5.2, 5.3, and 5.4.

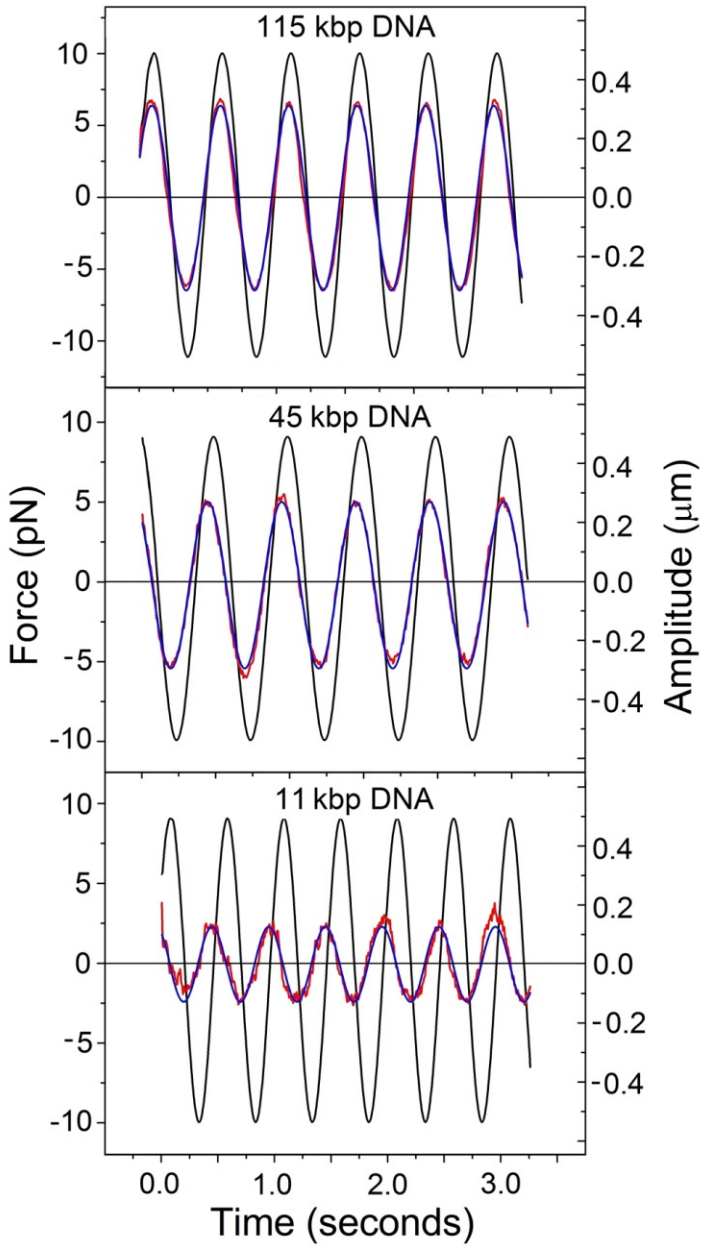

Figure 5.1 Measured force on a 1 μm radius microsphere (red; left axis) during ω = 12.57 rad s^{-1} stage oscillation (black; right axis). The blue curve is the fit to the raw force data (described in methods). The three panels show measurements in solutions of 3 different DNA lengths (specified at the top of each plot).

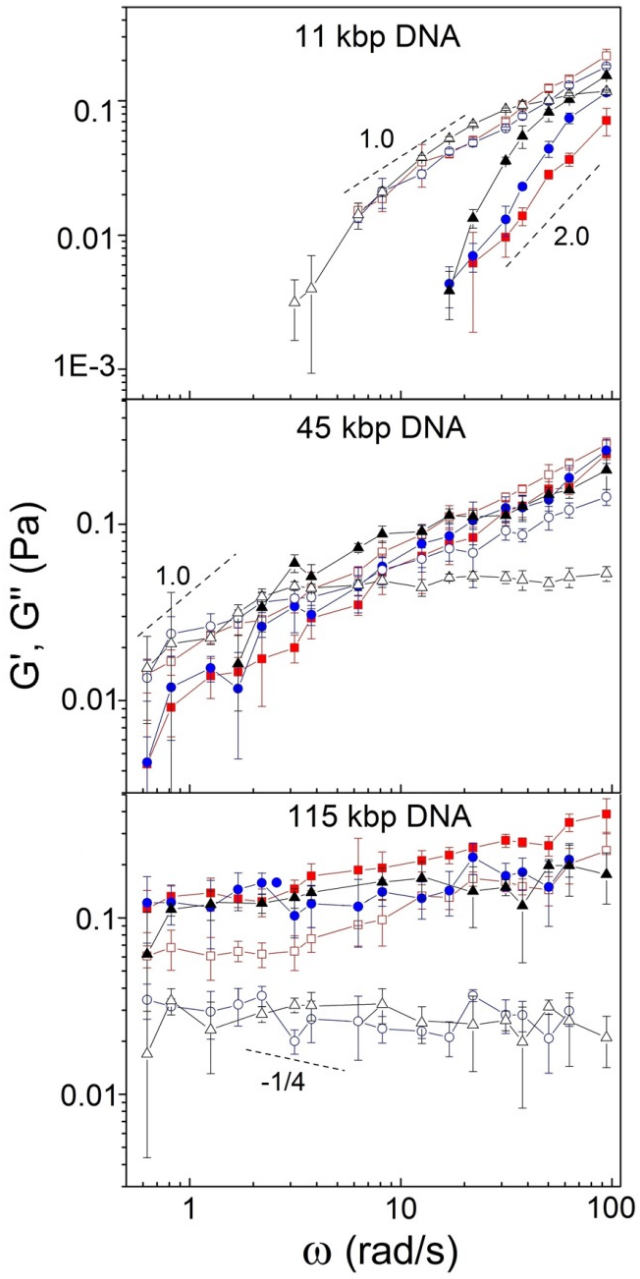

Figure 5.2 *G′(ω)* (closed symbols) and *G″(ω)* (open symbols) for 11, 45, and 115 kbp DNA measured with microspheres of radii: 1 μm (red squares), 2.25 μm (blue circles), and 3 μm (black triangles). Theoretically predicted scaling trends for the terminal regime ($G'(\omega) \sim \omega^2$, $G''(\omega) \sim \omega$) and the entangled regime ($G''(\omega) \sim \omega^{-1/4}$) are shown for comparison (dashed lines).

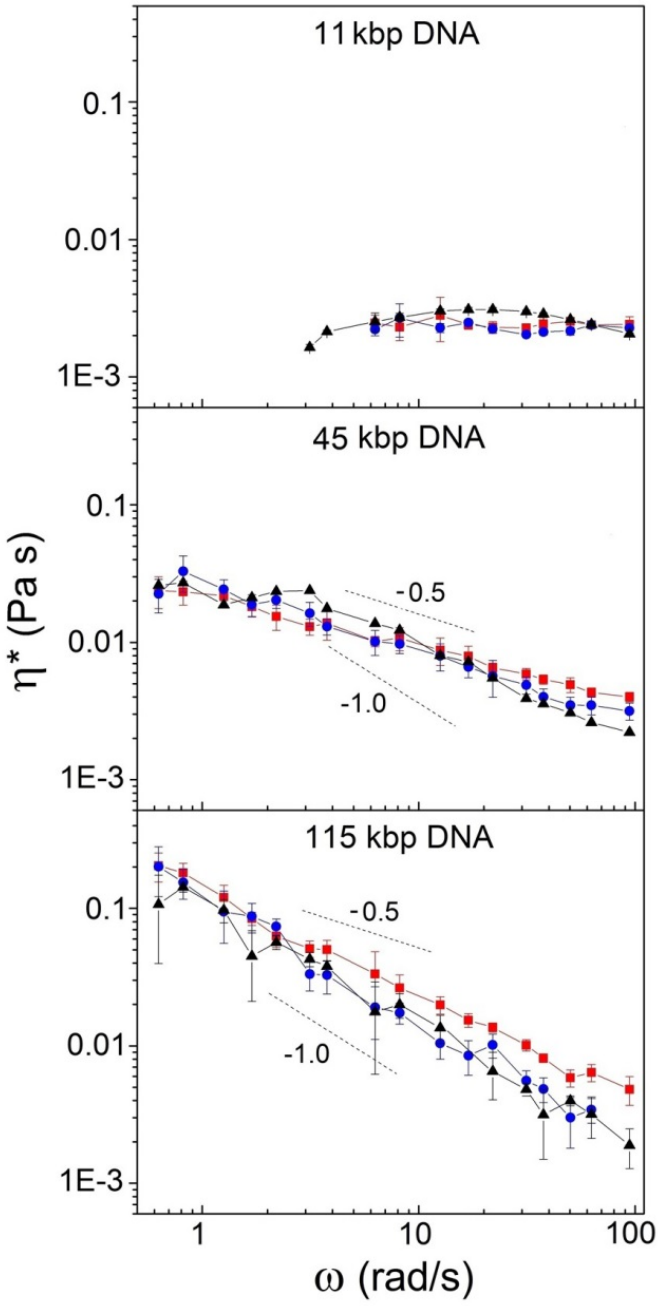

Figure 5.3 Complex viscosity, $h^*(\omega)$, measured with microspheres of radii 1 μm (red squares), 2.25 μm (blue circles), and 3 μm (black triangles) for each molecular length. Theoretically predicted scaling trends for semi-dilute ($h^*(\omega) \sim \omega^{-0.5}$) and fully entangled ($h^*(\omega) \sim \omega^{-1}$) solutions are shown for comparison.

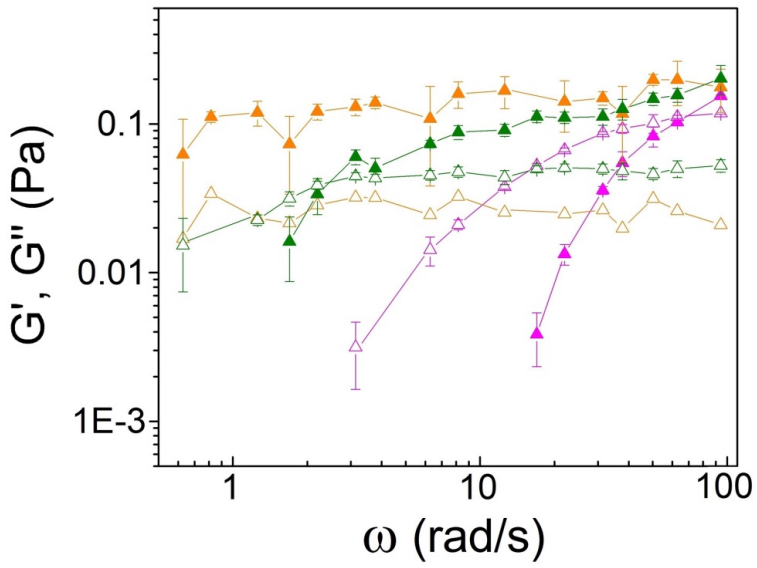

Figure 5.4 *G′(ω)* (closed symbols) and *G″(ω)* (open symbols) for 3 μm radius microspheres. Values for 11 kbp (magenta), 45 kbp (green), and 115 kbp (orange) DNA are shown.

5.4 Results

For 11 kbp DNA (0.8c_e) microsphere size had a minimal effect compared with that for the two longer DNAs (Figure 5.2). *G′(ω)* displays similar scaling with frequency for all probe sizes with magnitudes increasing slightly with microsphere size. *G″(ω)* is essentially independent of microsphere size except for the highest frequency where a modest rollover is observed for 3 μm radius microspheres. Measurements are consistent with terminal relaxation regime scaling behavior, *G′(ω)* ~ ω^2 and *G″(ω)* ~ ω, predicted by tube models (5), which indicates a low level of

entanglements (as expected for $c < c_e$). Further, the viscous response (G'') dominates over the measured frequency range, with the exception of the highest frequency for the 3 μm radius microspheres. The observed scaling of $G'(\omega)$ and $G''(\omega)$ for 11 kbp DNA is also consistent with that found in prior macrorheology measurements on calf-thymus DNA (polydisperse, ~13 kbp) at 1.0 mg/ml (150, 151). The measured complex viscosity, $h^*(\omega)$, also nearly probe size-independent (Figure 5.3), is largely frequency-independent, further indication of the terminal relaxation regime.

A greater dependence on probe size was observed with 45 kbp DNA ($2c_e$), mainly for frequencies above ~2 rad s^{-1}. As entanglements play a larger role in the response at higher frequencies, this finding suggests that the effect of microsphere size is linked to polymer entanglements. Below ~2 rad s^{-1} both $G'(\omega)$ and $G''(\omega)$ scale as ω^x with $x < 1$, consistent with a transition from the terminal regime to entanglement-dominated regime (5). In the well-entangled regime, reptation theory predicts that G' reaches a well-defined plateau, termed the plateau modulus (5), G_N^0, and G'' scales as $\omega^{-1/4}$. The most conspicuous probe-size dependence is that G'' with 3 μm radius probes dramatically plateaus at high frequency whereas it continues to rise with the two smaller probes. Although we do not observe a decreasing trend, this plateau is consistent with a transition from $G''(\omega) \sim \omega$ to $G''(\omega) \sim \omega^{-1/4}$. For G' we do not observe a clear plateau for any probe size, but G' with the 3 μm probe rolls over towards an apparent high frequency plateau at lower frequencies than observed with the smaller probes. Observed scaling behavior for 3 μm radius probes is also similar

to that observed in previous macrorheology measurements of 48.5 kbp DNA at 1.0 mg/ml (129).

Measurements with 45 kbp DNA also show $G''(\omega) > G'(\omega)$ over the entire frequency range for 1 μm microspheres, in contrast to the larger microsphere data which both display a crossover frequency, ω_c, above which $G'(\omega) > G''(\omega)$. This crossover frequency is predicted to be inversely proportional to the disengagement time (τ_d) for entangled polymers, i.e. the time for an entangled polymer to reptate out of its confining tube (1). Thus only for $\omega > \omega_c$ is tube confinement (entanglements) predicted to dominate the response. Our data show polymer disengagement times of $\tau_d \leq 0.07$ s ($\omega_c \geq 95$ rad s^{-1}), $\tau_d \approx 0.89$ s ($\omega_c \approx 7$ rad s^{-1}), and $\tau_d \approx 2.1$ s ($\omega_c \approx 3$ rad s^{-1}) for the 1 μm, 2.25 μm and 3 μm radii microspheres, respectively. By estimating $\tau_d \approx 0.065$ s for the 1 μm radius spheres, the disengagement times exhibit power law scaling with bead radius of $\tau_d \sim R^{3.16\pm0.06}$ (Figure 5.5). This scaling of τ_d with microsphere size indicates that larger microspheres can more effectively probe entanglements, suggesting that the continuum limit has not yet been reached with the smaller probes (134). This is also seen in the complex viscosity as the scaling exponent increases from ~-0.5 (predicted for the semi-dilute regime (129)) for 1 μm radius spheres to nearly -1, indicative of the entangled regime, for 3 μm spheres (Figure 5.3).

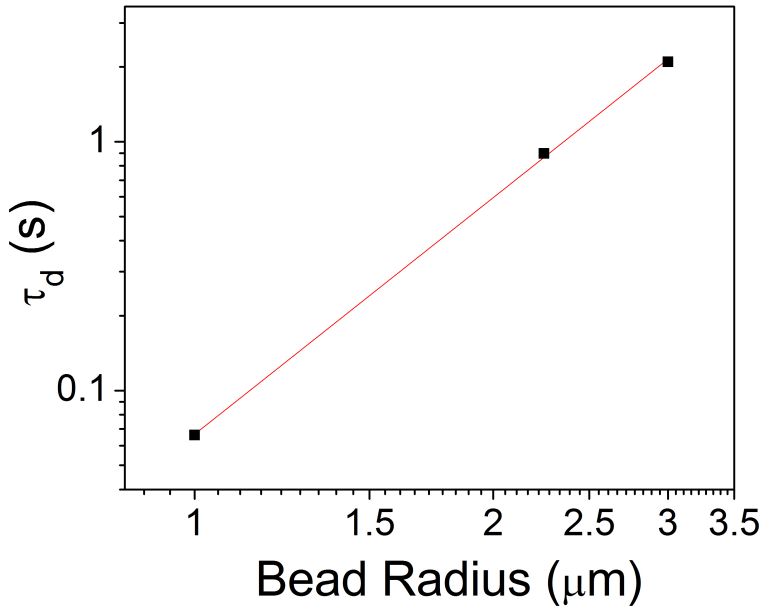

Figure 5.5 Polymer disengagement time (τ_d) vs. bead radius (R) for 45 kbp DNA at 1.0 mg/ml. Disengagement times for each bead size (black squares) are determined from the measured crossover frequency for each bead size as described in the text. The data is fit to a power law $\tau_d \sim R^{3.16\pm0.06}$ (red line).

For the longest DNA (115 kbp, $4c_e$), $G'(\omega) > G''(\omega)$ across the entire frequency spectrum for all three microspheres (Figure 5.2), implying $\tau_d > 10$ s ($\omega_c < 0.63$ rad s^{-1}), which is consistent with our previous finding of $\tau_d \approx 30$ s for this system via single molecule force measurements (10). This finding demonstrates that entanglements dominate the polymer response, as expected given $c \approx 4c_e$. However, while the measured viscoelastic moduli using 2.25 and 3 μm radius microspheres are nearly identical over the entire frequency range, the 1 μm radius microsphere data is distinctly different. For the two largest microspheres, $G'(\omega)$ is roughly constant over

the entire frequency range, displaying a plateau modulus of $G_N^0 \approx 0.2$ Pa, while $G''(\omega)$ displays a decreasing trend consistent with the predicted $\omega^{-1/4}$ scaling for the entanglement-dominated regime (5). In sharp contrast, $G'(\omega)$ and $G''(\omega)$ for 1 μm radius microspheres steadily increase with ω, indicating the probe is not behaving as if the well-entangled regime was reached. Further, the complex viscosity scales as $h^*(\omega) \sim \omega^{-1}$ for the two larger microspheres while the scaling exponent for 1 μm microspheres lies between -1 and -0.5 (Figure 5.3). These data indicate that for 115 kbp DNA only microspheres with radii larger than ~2 μm are fully sensitive to the molecular entanglements and thus have accessed the continuum limit, in contrast to the smaller microspheres which appear to be detecting fewer entanglements.

5.5 Discussion

We have shown that microsphere size plays an important role in active microrheology measurements for entangled DNA, a model flexible polymer. We investigated the transition to non-continuum behavior by conducting measurements with different probe sizes and DNA lengths, including longer DNA lengths than studied previously, and found a clear dependence on the degree of entanglement of the DNA. Our results suggest two distinct threshold probe sizes based on the level of polymer entanglement. For semi-dilute, unentangled DNA (11 kbp, $c < c_e$) the threshold probe radius is <1 μm, while for well-entangled DNA (115 kbp, $c \approx 4c_e$) it is ~2 μm.

One prior study observed a slight dependence of DNA microrheology results on microsphere size, but this was not found to be due to non-continuum effects, but rather to a depletion-layer effect in which polymer concentration near the surface of the microspheres is altered (147). While this effect can be important to consider, it becomes increasingly small for DNA concentrations above ~0.3 mg/ml and does not affect the frequency dependence of the moduli (147, 149, 152). Therefore, this effect cannot explain the dramatic changes we observe in scaling behavior of the moduli with microsphere size with our longest DNA at 1 mg/ml.

Thus, how can we explain the value of a threshold probe size for entangled DNA? There are several relevant length scales associated with both the individual polymers and the polymer network that could play a role in the viscoelastic response. The length scales associated with the individual DNA molecules are: persistence length (~50 nm), molecular length (3.7 μm, 15 μm and 39 μm), and radius of gyration (~0.3, 0.6, and 1.0 μm) (63). Length scales associated with the polymer network are: mesh size (~100 nm), tube diameter and polymer length between entanglements, l_e. l_e can be experimentally determined from the plateau modulus via the theoretically predicted relationship (1) $M_e = 4/5cRT/G_N^0$. For 3 μm microspheres, $G'(\omega)$ for all three DNA lengths approaches a value of ~0.2 Pa (Figure 5.4) giving $l_e \approx 5$ μm. As an aside, this finding verifies for the first time the predicted scaling $G_N^0 \sim M^0$ for entangled DNA (153). The tube diameter is comparable to the spatial distance between entanglements, thus using our measured l_e and treating DNA as a random coil, we calculate a tube diameter of ~0.7 μm.

Several length scales listed above are on the order of the microsphere radii, including the molecular length. However, if the threshold length scale were the DNA length, then we should not observe agreement between 2.25 μm and 3 μm radius microspheres for the 115 kbp DNA as all microsphere sizes are smaller than the DNA length.

Motivated by theoretical predictions (133-135), we can compare our threshold probe radius for well-entangled DNA (115 kbp, $n \approx 8$) to the tube diameter to find a criterion of $R \approx 3d_T$ for the continuum limit, which is closely aligned with the threshold size recently predicted by Yamamoto and Schweizer ($R \approx 5d_T$) for probe diffusion in typical entangled synthetic polymer melts (133-135). This previously un-validated threshold is demonstrated with 115 kbp DNA as we see microsphere-size independence only above $R \approx 2$ μm. Further, the measured scaling of G' and G'' with frequency for both the 2.25 and 3 μm radius microspheres ($\geq 3d_T$) is consistent with tube theory predictions for well-entangled polymers, in sharp contrast to the smaller 1 μm radius ($\sim 1.4d_T$) microspheres. We note that our criterion is actually slightly smaller than that predicted by Yamamoto and Schweizer which most likely stems from the different techniques addressed (passive probe diffusion vs. actively driven probes) as well as the different systems investigated (synthetic polymer melts vs. biopolymer solutions). Given these differences, the agreement between the theoretical predictions of Yamamoto and Schweizer and our experimental results lends credence to the universality of both results.

For 45 kbp DNA ($c \approx 2c_e$, $n \approx 3$), this threshold is not apparent as data for all three microsphere sizes differs. This is most likely due to the fact that 45 kbp DNA is only marginally entangled with ~3 entanglements per molecule. In fact, the predicted threshold of $R \approx 5d_T$ is only valid for well-entangled polymers with the criterion $n > 4$ (135). We can understand the probe size dependence for the 45 kbp DNA by analogy to cage-hopping, where probes diffusing through entanglements can exhibit increased diffusion by hopping to new entanglement cages, thereby momentarily avoiding entanglement constraints (20, 134). Similarly, if there are only a few entanglements in the vicinity of the probe, local fluctuations could momentarily release the probe from these constraints. This non-continuum effect should become more significant as the probe size decreases. Our finding that the measured polymer disengagement time scales roughly as the volume of the probe ($\tau_d \sim R^{3.16\pm0.06}$) for the 45-kbp DNA (Figure 5.5) supports this interpretation and is in agreement with recent theoretical studies that suggest that the rate of cage-hopping decreases with probe size (134).

Finally, for the semi-dilute, unentangled case (11 kbp, $n < 1$), our findings suggest agreement with recent theoretical studies that predict the threshold size for unentangled polymers is the radius of gyration (135). Here, all probe sizes are larger than the radius of gyration (~0.3 μm for 11 kbp DNA), and yield similar results, with scaling of G' and G'' in good agreement with theoretical expectations and prior macrorheology studies (1, 5, 150, 151). We note that as all microsphere sizes are also larger than the mesh size, this could also be an important length scale for un-entangled or weakly entangled polymers; however, distinguishing between the mesh size and the

radius of gyration does not serve a practical purpose as both length scales are smaller than microsphere sizes used in most microrheology experiments.

We also note that throughout this discussion we have focused on the consequences of a probe being too small, however in microrheology if a probe becomes too large, this could also lead to systematic errors in the measured response. For instance, in our experimental design the microspheres and polymer solution are in a sample chamber with a thickness of ~100 μm. If the trapped probe approaches either surface during oscillation, surface interactions will influence the measured response and the optical trap characteristics. Thus, we would suggest that a probe not be larger than ~10 μm to eliminate any unwanted experimental artifacts; however, testing this limit is left open for future studies.

5.6 Conclusion

We have used active microrheology measurements with optical tweezers, employing microspheres of varying radii, to characterize the effect of probe size on measured linear viscoelastic properties of entangled DNA (a model flexible polymer) of varying lengths and degrees of entanglement. We have found that for un-entangled solutions, where the molecular length is less than the length between entanglements, the storage and loss moduli reveal only a weak dependence on microsphere size, provided the microsphere radius is larger than the radius of gyration. However, the microsphere radius becomes more relevant as the number of entanglements per molecule increases (i.e., the length of the molecule becomes significantly larger than *l*-

$_e$). We propose that for well-entangled flexible polymers, microrheology measurements of linear viscoelastic properties only become microsphere size independent for microspheres with radii larger than ~3 times the tube diameter. Given that this threshold is significantly larger than the mesh size for flexible polymers (e.g., ~2 μm vs. 100 nm for 115 kbp DNA at 1 mg/ml), and larger than typical microsphere sizes used in microrheology experiments, this finding must be carefully considered. Considering the current wide spread use of microrheology to characterize biopolymer systems, this finding is important to understanding the complex relationship between stress and strain in these materials at the molecular level.

5.7 Acknowledgments

Chapter 5, in full, is a reprint of the material as it appears in Macromolecules. Chapman CD, Lee K, Henze D, Smith DE, & Robertson-Anderson RM (2014) Onset of Non-Continuum Effects in Microrheology of Entangled Polymer Solutions. *Macromolecules* 47(3):1181-1186. The dissertation author was the primary investigator and author of this paper.

Chapter 6

Nonlinear Microrheology Reveals Entanglement-driven Molecular-level Viscoelasticity of Concentrated DNA

6.1 Abstract

We optically drive a trapped microscale probe through entangled DNA at rates up to 100x the disentanglement rate (Wi≈100), then remove the trap and track subsequent probe recoil motion. We identify a unique crossover to the nonlinear regime at Wi≈20. Recoil dynamics display rate-dependent dilation and complex power-law healing of the reptation tube. The force response during strain exhibits key nonlinear features such as shear-thinning and yielding with power-law rate dependence. Our results, distinctly non-classical and in accord with recent theoretical predictions, reveal molecular dynamics governed by individual stress-dependent entanglements, rather than chain stretching.

6.2 Introduction

Microrheology, which uses embedded microspheres as probes, has recently emerged as a powerful technique for characterizing the molecular-level viscoelastic response of a wide range of soft materials and complex fluids, ubiquitous in industry, biology, and daily modern life (126, 147, 154-159). Microliter sample sizes enable characterization of valuable and difficult to produce materials, such as DNA and

cytoskeleton networks, inaccessible to bulk macrorheology techniques. Physiological scales of induced stresses (piconewtons) and strains (microns) are also directly applicable to a range of biological processes such as cell locomotion, blood flow, and elimination of pathological respiratory mucus comprised of entangled DNA (160); as well as new drug delivery techniques (161).

Linear microrheology measurements, which use passive probe motion or small force probe oscillations, can readily determine microscale linear rheological properties via generalized Stokes-Einstein relations (126), provided the probe is larger than a characteristic length scale of the material (97). While numerous studies have provided critical insight into the microscale linear viscoelastic properties of entangled polymers and other soft materials (25, 126, 147, 149, 154-159, 162, 163), far fewer have investigated the nonlinear regime in which the probe is actively driven (via magnetic or optical tweezers) to significantly deform the material from equilibrium (162, 164, 165). Here, interpretations within a macrorheology framework are complicated by the inherently inhomogeneous flow fields induced (158, 166). Thus, while microrheology has the unique ability to directly elucidate the molecular-level source of nonlinear material behavior, careful experimental design and interpretation, currently lacking in the literature, is critical.

Further, the reptation tube model, pioneered by deGennes (3) and Doi and Edwards (DE) (1), remarkable in its ability to predict linear properties of entangled polymers (167), fails to fully capture intriguing nonlinear effects such as shear-thinning and yielding; proving ill-equipped to explain potential polymer

disentanglement at high strain rates (129, 168). According to the tube model, each polymer is confined to move within a tube-like region formed by surrounding entangling polymers, restricting motion transverse to polymer contour. Tube model extensions, such as chain stretching and convective constraint release (CCR) have been proposed to accurately explain nonlinear effects (169-175), but conflicting experimental results and theories leave the regime controversial (176, 177). Previously, we used optical tweezers to characterize the near-equilibrium tube potential confining entangled DNA and found evidence of rate-dependent tube dilation not predicted by DE theory and anharmonic tube softening for large strains (25), in accord with recent simulations (178, 179). A recent theoretical model proposed by Sussman and Schweizer (SS) (170, 171, 175) for entangled rigid polymers predicts an anharmonic potential induced solely by individual topological constraints and coupled to the external stress imposed. Results of the SS model are consistent with previous extensions to DE theory that introduce CCR dynamics (173, 174) as well as experimental and simulation results for flexible polymers (178-181). Conversely, Lu et al. (LW) (169, 181) propose that chain stretching is the dominant mechanism underlying nonlinear features such as a stress overshoot during shear (129, 164). As such, experiments that directly elucidate the underlying molecular dynamics leading to widely observed nonlinear effects are needed (176, 177).

Here, we present a novel microrheology technique, using optical tweezers, able to directly characterize the molecular-level viscoelastic response of entangled DNA. We identify a unique crossover to nonlinearity at strain rates ~20 times faster than the

disengagement rate (i.e. the rate for a polymer to reptate out of its confining tube). We quantify for the first time the nonlinear spring constant associated with microscale viscoelasticity, which we show arises primarily from individual DNA entanglements that are coupled directly to induced stress, with chain stretching playing a minimal role. Results resolve a long-standing debate regarding the molecular dynamics underlying the nonlinear response of entangled polymers. Further, our technique and analysis can be used to characterize the microscale nonlinear viscoelastic properties of a wide range of complex fluids and materials.

6.3 Methods

Double-stranded 45 kbp DNA, was prepared, as previously described (14), by replication of a cloned fosmid construct in E. coli, followed by extraction, purification, and restriction enzyme treatment to convert supercoiled constructs to linear form. DNA solutions were prepared in aqueous buffer (10 mM Tris-HCl (pH 8), 1 mM EDTA, 10 mM NaCl) at concentrations of 0.3, 0.5, and 1.0 mg/ml corresponding to $0.5c_e$, c_e and $2c_e$, respectively, where c_e is the critical entanglement concentration (2). We can determine corresponding tube diameters d_T and disengagement times t_d by combining our previous results from linear oscillatory rheology experiments on 45 kbp DNA ($d_T \approx 0.7$ mm at 1 mg/ml, $G_N^0 \sim c^{1.8}$) (97) with tube theory scaling predictions (1). We estimate $t_d \approx 0.72$ s, 1.24 s and 2.57 s, and $d_T \approx 1.3$ mm, 1.0 mm, and 0.7 mm for 0.3, 0.5, and 1.0 mg/ml, respectively. Trace amounts of 4.5 mm microspheres

(probes) coated with Alexa-Fluor-488 BSA were embedded in DNA solutions which equilibrated for ~30 min prior to measurements.

A custom-built force-measuring optical trap, formed by a 1064 nm Nd:YAG fiber laser focused with a 60X 1.4 NA objective, was used to trap a probe within the sample chamber. A nanopositioning stage displaced DNA solutions 30 mm relative to the trapped probe at speeds v = 1 – 60 mm/s, which can be expressed as strain rates via $\dot{\gamma} = 3v/\sqrt{2}a$, where a is probe radius (165). To compare measured rates to characteristic relaxation rates for each solution, we report all speeds as Weissenberg numbers, $Wi = \dot{\gamma}\tau_d$. Several other groups have used a similar strain ramp technique to probe soft material linear dynamics (25, 157, 182). Following strain, the probe remained trapped for wait times, t_w, of 0 - 20 s (0 – 27.6t_d), after which the trap was shut off and subsequent probe position was tracked. An experimental schematic is shown in Figure 6.1. All reported data is an average of ≥10 trials. All measurements were repeated in water and viscous unentangled dextran solutions. Both controls exhibited purely Newtonian Stokes flow fluid behavior (Figure 6.4).

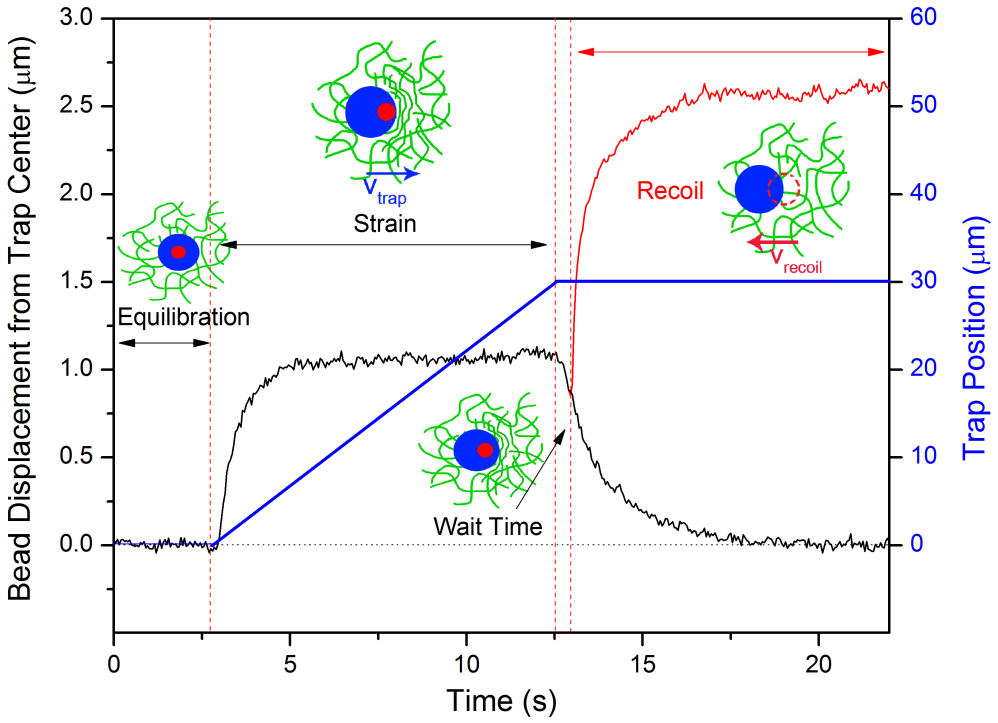

Figure 6.1 Experiment schematic. Trap position (blue) and probe displacement from trap center vs time are shown. Black/red curves are an average of 10 trials at 3 mm/s strain speed in 1.0 mg/ml DNA. Four stages of the experiment are shown: (Equilibration) Probes are trapped, probe and DNA solution equilibrate; (Strain) Traps are driven 30 mm at constant speed v_{trap} through solution; (Wait Time) Following strain, trapped probe begins to return to trap center; (Recoil) Trap is shut off and probe recoils backward (red curve) with speed v_{recoil}. Black curve during Recoil shows full return of probe to trap center if the laser is not shut off.

A position-sensing detector measured the laser deflection during strain at 20 kHz, while probe images were recorded at 100 s^{-1} both during and after strain. The laser deflection and probe displacement from the trap center during the strain are both proportional to the force acting on the trapped probe over the entire force range accessed. The trap was calibrated via the *in situ* equipartition method in our DNA solutions (157, 163) and Stokes drag in water (183). Measured force curves closely

approximate the fluid response, as we find no detectable difference in measured traces when trap stiffness is increased ~2x. For ease of rheological interpretation, measured force, F, and trap displacement, x, are converted to stress and strain via $s = F/pa^2$ and $g = x/2a$ respectively.

6.4 Results and Discussion

We find (Figure 6.2a) that the force exerted on the probe during strain initially increases with displacement (i.e. elastic response) before eventually yielding to a plateau (i.e. viscous response). Such yielding, a key feature of nonlinear strains, arises from unrecoverable microstructure rearrangement due to chain disentanglement and sliding (162, 168). We quantify the strain at which the DNA yields, g_y, as the point at which the differential modulus of the force response ($K = ds/dg_{trap}$), which characterizes the elasticity or stiffness of the material (Figure 6.2b), drops to $(2e)^{-1}$ of its peak value (Figure 6.2d). We find that for $Wi \leq 10$, g_y increases linearly with strain speed, indicative of the linear regime in which the relaxation rate is constant (i.e. unperturbed entanglement density). For $Wi \geq 20$ we find approximate scaling $g_y \sim Wi^{1/3}$ in agreement with previous macrorheology experiments on entangled melts, and suggested to arise from a loss of entanglements or tube softening (169, 171, 180). Within this framework, s_y should be proportional to g_y which we find for strains >0.5 (Figure 6.2d inset). While LW suggest that entanglement reduction is due primarily to chain stretching, not accounted for in SS theory (169, 181), they also show that significant chain stretch is the source of stress overshoots experimentally seen in

macrorheology studies on entangled flexible polymers including DNA (129, 164). We find no such overshoot, in accord with previous rheology studies on F-actin solutions and gelatins as well as SS predictions (162, 171, 184). This key difference between our measurements and macro- measurements on DNA highlights the unique system dynamics each technique probes (158) and shows that chain stretching only plays a significant role at the level of many-chain dynamics. Further, for very fast rates the yield strain appears to be asymptoting to a plateau with values of $0.7 > g_y > 2$ in agreement with SS predictions. Note that our results are distinctly non-classical as DE predicts a yield stress and strain that are both independent of strain rate with $g_y \sim 2.25$.

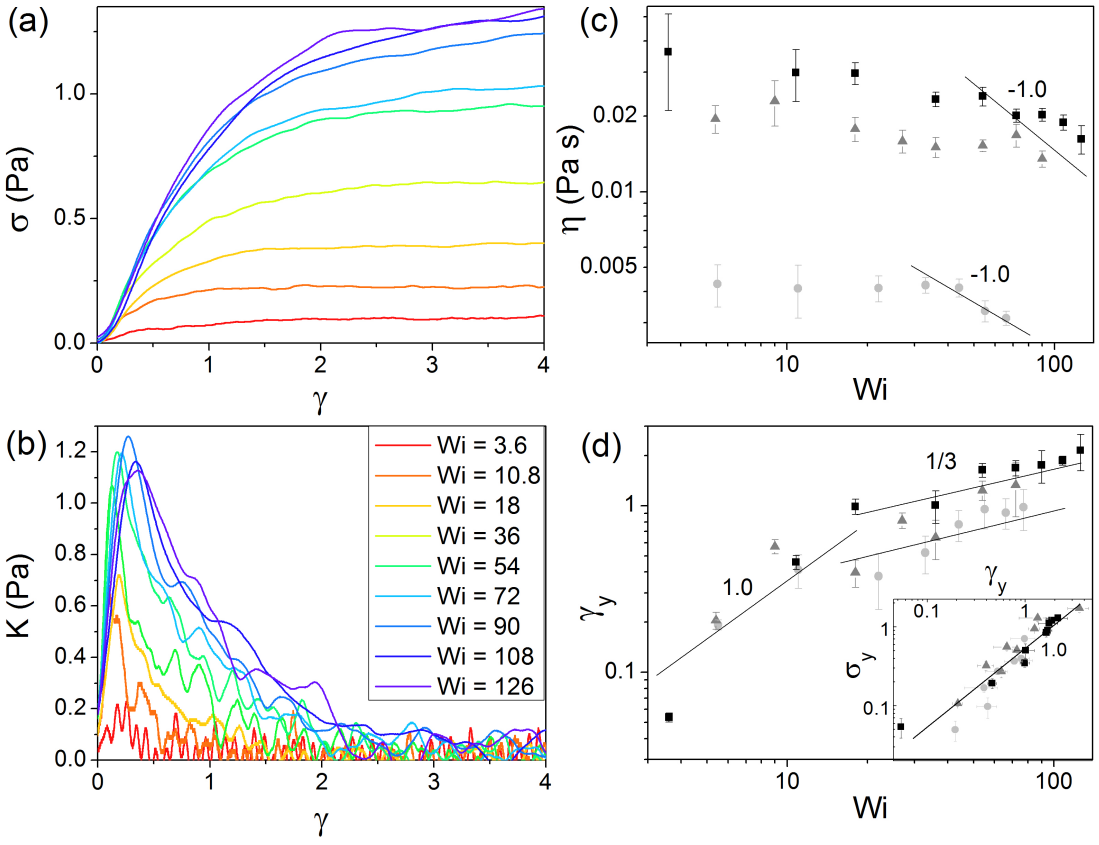

Figure 6.2 DNA response during constant rate strain. (a) Measured stress, σ, vs strain, γ, in 1.0 mg/ml DNA for strain rates Wi = 3.6 to 126 (see legend in (b)). (b) Corresponding differential modulus, K, vs strain for each strain rate. (c) Apparent viscosity η vs. strain rate for 0.3 (circles), 0.5 (triangles), and 1.0 mg/ml (squares) DNA with predicted scaling $\eta \sim Wi^{-1}$ shown. (d) Yield strain, γ_y, vs Wi for DNA solutions shown in (c) with predicted scaling for linear ($\gamma_y \sim Wi^{1.0}$) and nonlinear regimes ($\gamma_y \sim Wi^{1/3}$). Inset shows yield stress, σ_y, vs γ_y and predicted scaling $\sigma_y \sim \gamma_y$.

From the measured force plateaus (corresponding to $K \approx 0$), we calculate an apparent viscosity via Stokes drag, $h = F/6\pi a$, which is roughly rate independent for $Wi < 20$ then decreases, approaching a scaling of $h \sim Wi^{-1.0}$ (Figure 6.2c), in accord with macrorheology experiments that show shear-thinning exponents of -0.5 to -1 (1, 129). Classical DE theory predicts shear thinning in the nonlinear regime but with -1.5 scaling, while tube-model extensions that include CCR-like phenomena accurately capture experimental results (171-174).

Following a post-strain wait time, t_w, the trap is removed, after which the probe appeared to jump back or 'recoil' towards its original position (Figures 6.1, 6.3). The tracked position of the probe vs. time (Figure 6.3a) fit well to a decaying exponential, from which we determined a maximum recoil distance, R, and a decay rate, b, for each strain (Figure 6.3b,c). Our control data showed no measurable recoil, indicating that the recoil is an elastic effect dependent on entanglements. Thus, while the system has yielded to the strain by releasing some entanglements, the tube confinement has not been completely destroyed (170, 180). If the principle hindrance to probe recoil is individual entanglements then the recoil distance should be comparable to the tube diameter, in line with our results (Figure 6.3b). More importantly, we find R increases with Wi, crossing from linear scaling to $R \sim Wi^{0.4}$ at $Wi \approx 20$. While the low Wi scaling is indicative of a linear response, the high Wi scaling is in accord with SS predictions for the strain-rate dependence of tube dilation arising from direct coupling of the tube potential to the external stress (rather than simply shear induced affine deformation) (171). Further, R reaches $\sim 5d_T$, in excellent agreement with tube radius expansion

calculated by previous flexible polymer simulations (178). The wait-time dependence of R shows $R \leq d_T$ for wait times $t_w > O(t_D)$, demonstrating the coupled effect of the tube retracting to its equilibrium size (i.e. lost entanglements reforming) and those entanglements partially relaxing.

This dynamic entanglement reformation and relaxation is more readily seen in the wait time dependence of the recoil decay rate b (Figure 6.3c). We find that b decreases with t_w, but with distinctly different time dependences for Wi above and below ~20. For $Wi < 20$ the decay is exponential as expected for a single constant rate relaxation mechanism (i.e relaxation of the static deformed tube as predicted by DE). For $Wi > 20$ we find a short time plateau followed by $b \sim t^{-0.6}$ scaling, in agreement with the disengagement time scaling $t_D \sim t^{0.6}$ predicted by SS (170). Further, the two-step power-law relaxation is in close agreement with SS predictions for the stress relaxation following a constant shear strain, explained as an initial fast relaxation mechanism coupled to tube retraction (giving the short-time plateau), followed by simultaneous relaxation of the deformed entanglements (predicted by DE) and tube contraction (slowing the relaxation rate to a power-law). We also find that b increases with Wi in line with the strain-rate dependent relaxation rate predicted by tube theories with CCR-like phenomena (171, 174).

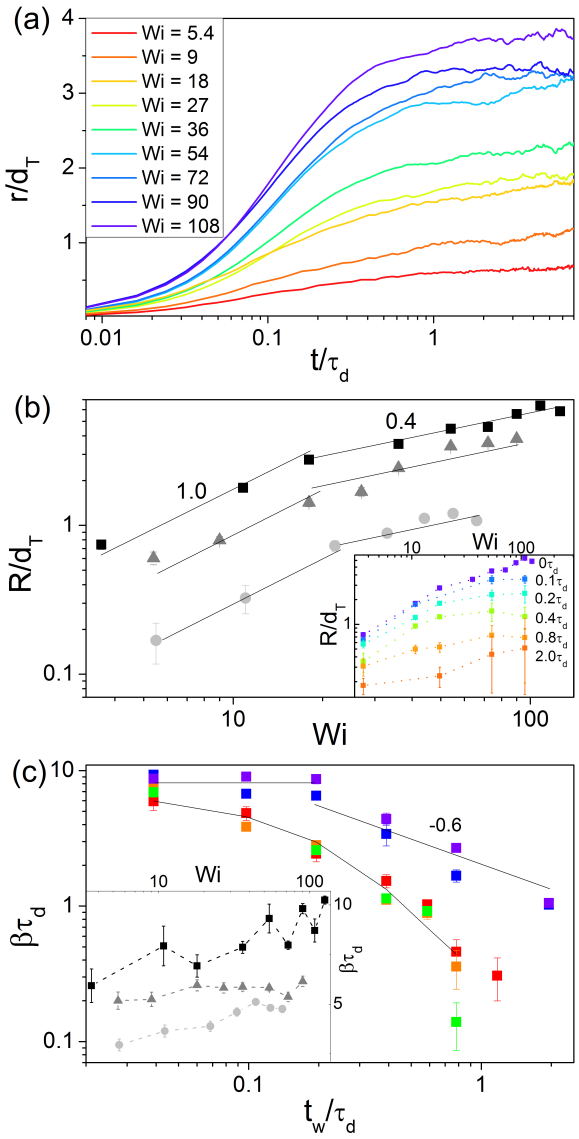

Figure 6.3 Probe recoil dynamics following strain. (a) Measured probe recoil, r, (normalized by tube diameter d_T) vs. time (normalized by disengagement time τ_d) when released immediately after strain (wait time t_w=0). Strain rates of Wi = 5.4 to 108 in 0.5 mg/ml DNA are shown. (b) Maximum recoil distance reached, R, vs Wi for 0.3 (circles), 0.5 (triangles), and 1.0 mg/ml (squares) DNA at t_w=0 with predicted scaling exponents for linear (1.0) and nonlinear (0.4) regimes. Inset shows R vs. Wi for t_w = 0 to $2\tau_d$ in 1.0 mg/ml DNA. (c) Measured recoil decay rate, β, vs t_w for 1.0 mg/ml DNA at Wi = 3.6 (red), 10.8 (orange), 18 (green), 54 (blue), and 108 (violet) with predicted scaling for linear (exponential curve) and nonlinear (0, -0.6) regimes. Inset shows β vs. Wi for t_w=0 for all three DNA solutions.

To further characterize the microscale stress relaxation, we calculate an effective spring constant associated with entanglements. As the probe recoil fits well to a decaying exponential, we can treat it as that of an overdamped harmonic oscillator and use b to determine an effective entanglement spring constant, k, via $b = [b - (b^2 - 4mk)^{1/2}]/2m$, where $b = 6pha$ and m is probe mass. Calculated spring constants are small enough that $k \sim b$, so corresponding rate and time dependences of k are as in Figure 6.3c. Thus, the elastic entanglement stiffness is strain-rate dependent and crosses from linear to nonlinear relaxation dynamics at $Wi \sim 20$.

For $Wi < 20$ spring constants are nearly rate independent and increase with concentration as expected for the linear regime with average values 3.01, 1.65, and 1.49 pN/mm for the 1.0, 0.5 and 0.3 mg/ml DNA, respectively. We can convert our low Wi spring constant, k_L, for each concentration to a modulus, G_L, and compare with the predicted linear modulus $G_e = 3k_bTr_e$ (1), where r_e is the density of entanglements. Our G_L values are 0.84, 0.46 and 0.41 Pa, in excellent agreement with the predicted values 0.76, 0.43 and 0.29 Pa for 1.0, 0.5 and 0.3 mg/ml DNA. Further, our measured 1.0 mg/ml modulus is in accord with macrorheology plateau modulus measurements for similar DNA solutions (0.65 Pa) (129).

In equilibrium, the elastic energy of each entanglement monomer should be comparable to k_bT. Thus, to confirm that our measured spring constants are indeed due to individual entanglements we compare our near-equilibrium elastic energy to the thermal energy, i.e. $\frac{1}{2}k_Lx^2 \approx k_bT$. We calculate an approximate equilibrium stretching length scale, x, associated with each entanglement of $x \approx 49$ nm, 79 nm, and 88 nm for

1.0, 0.5, and 0.3 mg/ml DNA, respectively. The size of each 'entanglement monomer' should be on the order of the mesh size of the solution, z, which is ~100 nm, 140 nm and 180 nm for 1.0, 0.5, and 0.3 mg/ml DNA, respectively; giving us $x \approx 0.5z$, and showing that the equilibrium stretching length is comparable to and scales with the entanglement monomer size. Thus, individual DNA entanglements are the source of the microscale elastic response, as confirmed by our other presented results. If we assume a constant stretching length, as k increases to ~2x the equilibrium value (with increasing Wi, Figure 6.3c) the elastic energy exceeds the thermal energy and thus cannot be sustained, so entanglements must be released, reducing the average entanglement density and softening the confining tube.

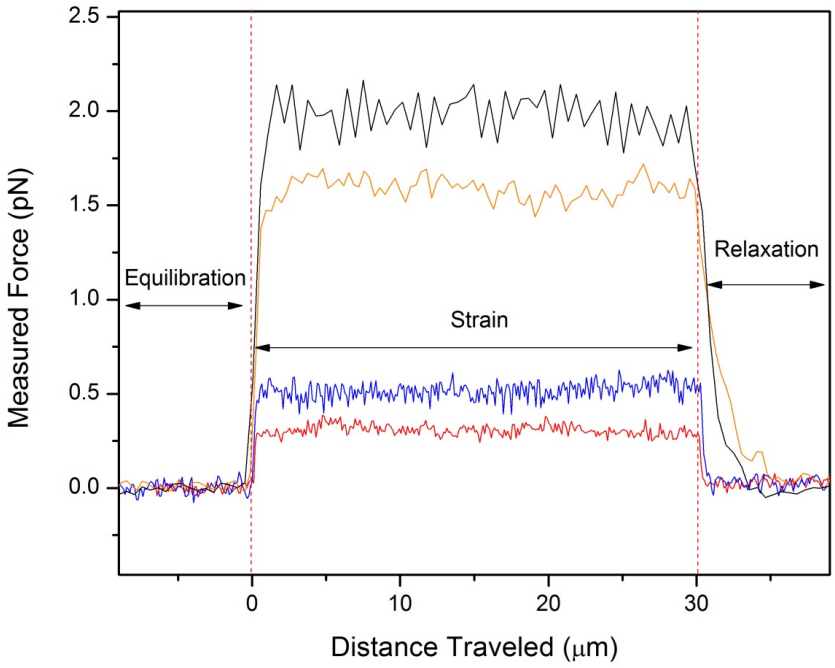

Figure 6.4 Sample force traces for a probe dragged in a purely Newtonian fluid (9% w/v, unentangled, 500 kDa dextran solution). A probe is captured in solution and allowed 2 seconds to equilibrate. This is followed by the strain phase in which the bead is pulled 30 μm at a constant strain rate. Strain rates from 3 – 35 mm/s were measured. Here, four sample strain rates are shown; 3 (red), 5 (blue), 20 (orange), and 25 mm/s (black). Following the strain, the probe is allowed to relax back to the trap center. As expected, the force reaches a constant value (independent of strain distance) almost instantaneously, showing a purely viscous force response. Subsequent relaxation also occurs almost instantaneously (as compared to our measured entangled DNA solutions). Purely Newtonian behavior was observed for all measured strain rates.

6.5 Conclusion

Here, we have demonstrated a novel experimental technique in which we use an optically trapped probe to drive entangled DNA far from equilibrium, and characterize the molecular-level linear and nonlinear viscoelastic response during and following strain. We show for the first time that microscale nonlinear viscoelasticity for entangled DNA is driven by individual entanglement constraints rather than chain stretching. However, the entanglements are distinctly non-classical, exhibiting rate-dependent releasing or tube dilation and complex power-law relaxation dynamics. Our results provide critical insights into the long-standing debate on the molecular dynamics underlying the experimentally observed nonlinear response exhibited in entangled polymers. Our technique and analysis can also be used to characterize the microscale viscoelastic properties of a wide range of complex fluids and materials.

6.6 Acknowledgments

Chapter 6, in full, is a reprint of the material as it appears in Physical Review Letters. Chapman CD & Robertson-Anderson RM (2014) Nonlinear Microrheology Reveals Entanglement-Driven Molecular-Level Viscoelasticity of Concentrated DNA. *Phys Rev Lett* 113(9):098303. The dissertation author was the primary investigator and author of this paper.

Chapter 7

Conclusions, Future Work

7.1 Introduction

The preceding chapters have discussed the state of single-molecule studies and the contributions of my research to the current understanding of polymer theory. Diffusion of polymers in linear-circular blends has been revealed to possess a non-monotonic dependence on blend ratio, a find with clear industrial applications as synthetic polymers are typically impure, with polymers of a non-desired topology potentially drastically altering the viscoelastic properties of a given fluid. The diffusive behavior of DNA within crowded environments, on the other hand, was shown to depend predominantly upon crowder length.

Additionally, the viscoelastic properties of entangled DNA networks were examined using dual-force optical tweezers. A clear bead-size dependence was observed for beads smaller than ~3x the tube diameter, above which measurements are able to access macroscopic (bulk) properties of the fluid. The non-linear properties of DNA networks were also studied, revealing molecular dynamics, which are governed primarily by stress-dependent entanglements. However, many open questions still remain, with multiple promising avenues of research presenting themselves as a clear continuation of this work.

7.2 Bilinear blends

While blends of differing topologies, here linear and circular, were examined, bilinear blends, consisting of two distinct linear polymers of differing length could potentially yield interesting and useful results. Despite the relative simplicity of the system, bulk studies on bilinear blends have yielded highly complex behavior, with diffusivity and viscoelasticity displaying a strong dependence on the relative polymer lengths and volume fractions. For example, if one of the polymer species is short enough such that it will fail to entangle at a given concentration, the volume fraction occupied by the polymer will behave approximately as a solvent (185). If both polymers are large enough and concentrated enough as to become entangled, more complicated viscoelastic behavior is observed, with multiple peaks for *G'* and *G''* commonly found, indicative of the multiple timescales associated with the internal dynamics of the system (185). Classical reptation theory is unable to account for this type of bilinear system, in particular the assumption of a static tube has been found to be troublesome (5). Potential theories have been described to address these more complex findings, such as double reptation, with moderate success. However, the dynamics are still not fully understood and single-molecule studies in this area are lacking.

As with circular/linear polymeric blends, the knowledge gained from the behavior of bilinear blends would of great interest to industry and the creation of new, tunable materials. Thus, both diffusion studies, involving labeling and subsequently

tracking DNA molecules, and microrheology studies to obtain the viscoelastic properties of bilinear blends would potentially yield valuable results.

7.3 Crowding

Our previous results involving the diffusive and conformational behavior of linear DNA molecules in highly crowded environments showed a previously unknown entropy driven conformational change. This elongation of the DNA was most pronounced for our largest, 115kbp, DNA molecules diffusing in an environment crowded with 500 kDa dextran. Whether this behavior would be observed for circular, or even supercoiled DNA is unclear. Additionally, the effects of different crowding agents, polyethylene glycol (a common industrial compound) or ficoll for example, could yield new insights into the diffusive mechanisms involved for DNA in these crowded environments. Multiple crowders could perhaps be combined to lend a more realistic intracellular environment, important for medical applications, such as drug delivery and gene therapy, which rely heavily on diffusion within cellular crowding.

7.4 Microrheology

Another relevant study would be to examine the potential ‘wake’ created when using active microrheology techniques. When a bead is actively driven through a complex fluid, polymers may begin to accumulate along the leading edge of the bead, leaving an area devoid of polymers along the trailing edge. This phenomenon has been

observed experimentally and through simulations previously in colloid solutions (186). To ensure this would not have a noticeable effect on our measurements, we have previously attempted to observe any potential 'wake' effects by utilizing our dual-trap optical tweezers setup. By first testing the force response on individually trapped beads being actively driven through an entangled DNA solution for 30 μm at a constant rate, then comparing to the force response when both traps are utilized to drive two closely spaced beads (~ 15 μm apart, spaced along the axis of the driving force), we were able to conclude that any potential wake effects were insignificant for measurements at low speed/concentration regimes. The force response of the individual bead, as well as each of the two simultaneously driven beads were equal. However, for speeds above 30 μm/s in 1.0 mg/ml 115 kbp DNA, a clear difference was observed. Here, the force felt by the lagging bead was found to plateau at a lower value than that of the leading bead. The experiment was repeated in both directions, to ensure the effect was not due to differences in the individual traps, revealing identical behavior. While shown to have little effect for studies at lower speeds or concentrations, this trailing 'wake' could potentially have profound effects on interpreting future high-speed, non-linear microrheology results.

7.5 Conclusion

Despite being relatively young, single-molecule studies have proven to be an incredibly powerful set of techniques, having brought about innumerable important

discoveries to the world of polymer physics. The research in this thesis has attempted to answer at least a few of the countless questions facing the field today; however, many open questions persist. With the broad range of fields, which depend on its advancement, it is certain to be studied in earnest for the foreseeable future.

References

1. Doi M & Edwards SF (1986) *The theory of polymer dynamics* (Oxford University Press, New York) pp xiii, 391 p.

2. Robertson RM & Smith DE (2007) Self-diffusion of entangled linear and circular DNA molecules: Dependence on length and concentration. *Macromolecules* 40(9):3373-3377.

3. De Gennes P-G (1979) *Scaling concepts in polymer physics* (Cornell university press).

4. Milner S & McLeish T (1998) Reptation and contour-length fluctuations in melts of linear polymers. *Phys Rev Lett* 81(3):725.

5. McLeish TCB (2002) Tube theory of entangled polymer dynamics. *Adv Phys* 51(6):1379-1527.

6. Doi M (1983) Explanation for the 3. 4-power law for viscosity of polymeric liquids on the basis of the tube model. *Journal of Polymer Science Polymer Physics Edition* 21(5):667-684.

7. Wheeler L & Lodge T (1989) Tracer diffusion of linear polystyrenes in dilute, semidilute, and concentrated poly (vinyl methyl ether) solutions. *Macromolecules* 22(8):3399-3408.

8. Colby RH & Rubinstein M (1990) Two-parameter scaling for polymers in θ solvents. *Macromolecules* 23(10):2753-2757.

9. Perkins TT, Smith DE, & Chu S (1994) Direct observation of tube-like motion of a single polymer chain. *Science* 264(5160):819-822.

10. Robertson RM & Smith DE (2007) Direct measurement of the intermolecular forces confining a single molecule in an entangled polymer solution. *Phys Rev Lett* 99(12).

11. Kapnistos M, Lang M, Vlassopoulos D, Pyckhout-Hintzen W, Richter D, Cho D, Chang T, & Rubinstein M (2008) Unexpected power-law stress relaxation of entangled ring polymers. *Nat Mater* 7(12):997-1002.

12. Bielawski CW, Benitez D, & Grubbs RH (2002) An" endless" route to cyclic polymers. *Science* 297(5589):2041-2044.

13. Chapman CD, Shanbhag S, Smith DE, & Robertson-Anderson RM (2012) Complex effects of molecular topology on diffusion in entangled biopolymer blends. *Soft Matter* 8(35):9177-9182.

14. Laib S, Robertson RM, & Smith DE (2006) Preparation and characterization of a set of linear DNA molecules for polymer physics and rheology studies. *Macromolecules* 39(12):4115-4119.

15. Carmesin I & Kremer K (1988) The bond fluctuation method: a new effective algorithm for the dynamics of polymers in all spatial dimensions. *Macromolecules* 21(9):2819-2823.

16. Höfling F & Franosch T (2013) Anomalous transport in the crowded world of biological cells. *Reports on Progress in Physics* 76(4):046602.

17. Nakano S-i, Miyoshi D, & Sugimoto N (2013) Effects of Molecular Crowding on the Structures, Interactions, and Functions of Nucleic Acids. *Chemical reviews* 114(5):2733-2758.

18. Breuer KS (2005) *Microscale diagnostic techniques* (Springer).

19. Williams MC (2002) Optical tweezers: measuring piconewton forces. *Biophysics Textbook Online: http://www. biophysics. org/btol*.

20. Guo H, Bourret G, Lennox RB, Sutton M, Harden JL, & Leheny RL (2012) Entanglement-Controlled Subdiffusion of Nanoparticles within Concentrated Polymer Solutions. *Phys Rev Lett* 109(5):055901.

21. Tuteja A, Mackay ME, Narayanan S, Asokan S, & Wong MS (2007) Breakdown of the continuum stokes-einstein relation for nanoparticle diffusion. *Nano letters* 7(5):1276-1281.

22. Pecora R (1991) DNA: A Model Compound for solution studies of macromolecules. *Science* 251(4996):893-898.

23. Schroeder CM, Babcock HP, Shaqfeh ES, & Chu S (2003) Observation of polymer conformation hysteresis in extensional flow. *Science* 301(5639):1515-1519.

24. Shaqfeh ESG (2005) The dynamics of single-molecule DNA in flow. *J Non-Newton Fluid* 130(1):1-28.

25. Robertson RM & Smith DE (2007) Direct measurement of the intermolecular forces confining a single molecule in an entangled polymer solution. *Physical Review Letters* 99(12):126001.

26. Singla S & Beckham HW (2008) Miscible Blends of Cyclic Poly(oxyethylene) in Linear Polystyrene. *Macromolecules* 41(24):9784-9792.

27. Dealy JM & Larson RG (2006) *Structure and Rheology of Molten Polymers: From Structure to Flow Behavior and Back Again* (Hanser Gardner Publications, Cincinnati).

28. de Gennes PG (1979) *Scaling Concepts in polymer physics* (Cornell University Press, Ithaca, NY).

29. Colby RH & Rubinstein M (1990) Two-parameter scaling for polymers in theta solvents. *Macromolecules* 23(10):2753-2757.

30. Heo Y & Larson RG (2005) The scaling of zero-shear viscosities of semidilute polymer solutions with concentration. *Journal of Rheology* 49(5):1117-1128.

31. Klein J (1986) Dynamics of entangled linear, branched, and cyclic polymers. *Macromolecules* 19(1):105-118.

32. Kawaguchi D, Masuoka K, Takano A, Tanaka K, Nagamura T, Torikai N, Dalgliesh RM, Langridge S, & Matsushita Y (2006) Comparison of interdiffusion behavior between cyclic and linear polystyrenes with high molecular weights. *Macromolecules* 39(16):5180-5182.

33. Roovers J (1988) Viscoelastic Properties of Polybutadiene Rings. *Macromolecules* 21(5):1517-1521.

34. Obukhov SP, Rubinstein M, & Duke T (1994) Dynamics of a Ring Polymer in a Gel. *Phys Rev Lett* 73(9):1263-1266.

35. McKenna GB, Hostetter BJ, Hadjichristidis N, Fetters LJ, & Plazek DJ (1989) A study of the linear viscoelastic properties of cyclic polystyrenes using creep and recovery measurements. *Macromolecules* 22(4):1834-1852.

36. Semlyen JA (2000) *Cyclic Polymers* (Klwer Academic Publishers, Amsterdam) 2 Ed.

37. Iyer BVS, Lele AK, & Juvekar VA (2006) Flexible ring polymers in an obstacle environment: Molecular theory of linear viscoelasticity. *Phys Rev E* 74(2):-.

38. Robertson RM & Smith DE (2007) Direct measurement of the confining forces imposed on a single molecule in a concentrated solution of circular polymers. *Macromolecules* 40(24):8737-8741.

39. Robertson RM & Smith DE (2007) Strong effects of molecular topology on diffusion of entangled DNA molecules. *P Natl Acad Sci USA* 104(12):4824-4827.

40. Subramanian G & Shanbhag S (2008) Conformational properties of blends of cyclic and linear polymer melts. *Phys Rev E Stat Nonlin Soft Matter Phys* 77(1 Pt 1):011801.

41. Subramanian G & Shanbhag S (2008) Self-diffusion in binary blends of cyclic and linear polymers. *Macromolecules* 41(19):7239-7242.

42. McLeish T (2008) Polymer Dynamics Floored by the Rings. *Nat Mater* 7(12):933-935.

43. Iyer BVS, Shanbhag S, Juvekar VA, & Lele AK (2008) Self-Diffusion Coefficient of Ring Polymers in Semidilute Solution. *Journal of Polymer Science Part B-Polymer Physics* 46(21):2370-2379.

44. Nam S, Leisen J, Breedveld V, & Beckham HW (2009) Melt Dynamics of Blended Poly(oxyethylene) Chains and Rings. *Macromolecules* 42(8):3121-3128.

45. Vettorel T, Grosberg AY, & Kremer K (2009) Statistics of polymer rings in the melt: a numerical simulation study. *Phys Biol* 6(2):-.

46. Yang YB, Sun ZY, Fu CL, An LJ, & Wang ZG (2010) Monte Carlo simulation of a single ring among linear chains: Structural and dynamic heterogeneity. *Journal of Chemical Physics* 133(6):-.

47. Habuchi S, Satoh N, Yamamoto T, Tezuka Y, & Vacha M (2010) Multimode Diffusion of Ring Polymer Molecules Revealed by a Single-Molecule Study. *Angew Chem Int Edit* 49(8):1418-1421.

48. Roovers J & Toporowski PM (1988) Synthesis and characterization of ring polybutadienes. *Journal of Polymer Science Part B-Polymer Physics* 26(6):1251-1259.

49. Bielawski CW, Benitez D, & Grubbs RH (2002) An "endless" route to cyclic polymers. *Science* 297(5589):2041-2044.

50. Orrah DJ, Semlyen JA, & Ross-Murphy SB (1988) Studies of Cyclic and Linear Poly(Dimethylsiloxanes). XXVII. Bulk Viscosities Above the Critical Molar Mass for Entanglement *Polymer* 29(8):1452-1454.

51. Graessley WW (1982) Entangled linear, branched and network polymer systems — Molecular theories. *Advances in Polymer Science* 47:67-117.

52. Mills PJ, Mayer JW, Kramer EJ, Hadziioannou G, Lutz P, Strazielle C, Rempp P, & Kovacs AJ (1987) Diffusion of polymer rings in linear polymer matrices. *Macromolecules* 20(3):513-518.

53. Roovers J (1985) The melt properties of ring polystyrenes. *Macromolecules* 18(6):1359-1361.

54. Halverson JD, Grest GS, Grosberg AY, & Kremer K (2012) Rheology of ring polymer melts: from linear contaminants to ring-linear blends. *Phys Rev Lett* 108(3):038301.

55. Iyer BV, Lele AK, & Juvekar VA (2006) Flexible ring polymers in an obstacle environment: Molecular theory of linear viscoelasticity. *Phys Rev E* 74(2):021805.

56. McLeish T (2008) Polymer dynamics: Floored by the rings. *Nature materials* 7(12):933-935.

57. McKenna GB & Plazek DJ (1986) The Viscosity of Blends of Linear and Cyclic Molecules of Similar Molecular Mass. *Polymer Communication* 27(10):304-306.

58. Tead SF, Kramer EJ, Hadziioannou G, Antonietti M, Sillescu H, Lutz P, & Strazielle C (1992) Polymer topology and diffusion: a comparison of diffusion in linear and cyclic macromolecules. *Macromolecules* 25(15):3942-3947.

59. Cosgrove T, Turner MJ, Griffiths PC, Hollingshurst J, Shenton MJ, & Semlyen JA (1996) Self-diffusion and spin-spin relaxation in blends of linear and cyclic polydimethylsiloxane melts. *Polymer* 37(9):1535-1540.

60. von Meerwall E, Ozisik R, Mattice WL, & Pfister PM (2003) Self-diffusion of linear and cyclic alkanes, measured with pulsed-gradient spin-echo nuclear magnetic resonance. *Journal of Chemical Physics* 118(8):3867-3873.

61. Iyer BVS, Lele AK, & Shanbhag S (2007) What is the size of a ring polymer in a ring-linear blend? *Macromolecules* 40(16):5995-6000.

62. Muller M, Wittmer JP, & Cates ME (1996) Topological effects in ring polymers: A computer simulation study. *Phys Rev E Stat Phys Plasmas Fluids Relat Interdiscip Topics* 53(5):5063-5074.

63. Robertson RM, Laib S, & Smith DE (2006) Diffusion of isolated DNA molecules: dependence on length and topology. *Proceedings of the National Academy of Sciences* 103(19):7310-7314.

64. Robertson RM, Laib S, & Smith DE (2006) Diffusion of isolated DNA molecules: Dependence on length and topology. *P Natl Acad Sci USA* 103(19):7310-7314.

65. Efron B & Tibshirani R (1991) Statistical data analysis in the computer age. *Science* 253(5018):390-395.

66. Magatti D & Ferri F (2001) Fast multi-tau real-time software correlator for dynamic light scattering. *Appl Opt* 40(24):4011-4021.

67. Ramirez J, Sukumaran SK, & Likhtman AE (2007) Significance of cross correlations in the stress relaxation of polymer melts. *Journal of Chemical Physics* 126(24):244904.

68. Watanabe J, Harkness BR, Sone M, & Ichimura H (1994) Rigid-rod polyesters with flexible side chains. 4. Thermotropic behavior and phase structures in polyesters based on 1,4-dialkyl esters of pyromellitic acid and 4,4'-biphenol. *Macromolecules* 27(2):507-512.

69. Park SJ & Larson RG (2006) Long-chain dynamics in binary blends of monodisperse linear polymers. *Journal of Rheology* 50(1):21-39.

70. Vasquez R & Shanbhag S (2011) Percolation of Trace Amounts of Linear Polymers in Melts of Cyclic Polymers. *Macromol Theor Simul* 20(3):205-211.

71. Ellis RJ (2001) Macromolecular crowding: an important but neglected aspect of the intracellular environment. *Current opinion in structural biology* 11(1):114-119.

72. Miyoshi D & Sugimoto N (2008) Molecular crowding effects on structure and stability of DNA. *Biochimie* 90(7):1040-1051.

73. Tan C, Saurabh S, Bruchez MP, Schwartz R, & LeDuc P (2013) Molecular crowding shapes gene expression in synthetic cellular nanosystems. *Nature nanotechnology* 8(8):602-608.

74. Rivas G, Ferrone F, & Herzfeld J (2004) Life in a crowded world. *EMBO reports* 5(1):23-27.

75. Pelletier J, Halvorsen K, Ha B-Y, Paparcone R, Sandler SJ, Woldringh CL, Wong WP, & Jun S (2012) Physical manipulation of the Escherichia coli chromosome reveals its soft nature. *Proceedings of the National Academy of Sciences* 109(40):E2649-E2656.

76. Heddi B & Phan AT (2011) Structure of human telomeric DNA in crowded solution. *J Am Chem Soc* 133(25):9824-9833.

77. Li G-W, Berg OG, & Elf J (2009) Effects of macromolecular crowding and DNA looping on gene regulation kinetics. *Nature Physics* 5(4):294-297.

78. Sherr CJ (1996) Cancer cell cycles. *Science* 274(5293):1672-1677.

79. Blackburn EH (1991) Structure and function of telomeres. *Nature* 350(6319):569-573.

80. Herweijer H & Wolff J (2003) Progress and prospects: naked DNA gene transfer and therapy. *Gene therapy* 10(6):453-458.

81. Wiethoff CM & Middaugh CR (2003) Barriers to nonviral gene delivery. *Journal of pharmaceutical sciences* 92(2):203-217.

82. Bally MB, Harvie P, Wong FM, Kong S, Wasan EK, & Reimer DL (1999) Biological barriers to cellular delivery of lipid-based DNA carriers. *Advanced drug delivery reviews* 38(3):291-315.

83. Pastor I, Pitulice L, Balcells C, Vilaseca E, Madurga S, Isvoran A, Cascante M, & Mas F (2014) Effect of crowding by Dextrans in enzymatic reactions. *Biophysical chemistry* 185:8-13.

84. Dauty E & Verkman A (2005) Actin Cytoskeleton as the Principal Determinant of Size-dependent DNA Mobility in Cytoplasm A NEW BARRIER FOR NON-VIRAL GENE DELIVERY. *Journal of Biological Chemistry* 280(9):7823-7828.

85. Lukacs GL, Haggie P, Seksek O, Lechardeur D, Freedman N, & Verkman A (2000) Size-dependent DNA mobility in cytoplasm and nucleus. *Journal of Biological Chemistry* 275(3):1625-1629.

86. Jones JJ, van der Maarel JR, & Doyle PS (2011) Effect of nanochannel geometry on DNA structure in the presence of macromolecular crowding agent. *Nano letters* 11(11):5047-5053.

87. Zorrilla S, Hink MA, Visser AJ, & Lillo MP (2007) Translational and rotational motions of proteins in a protein crowded environment. *Biophysical chemistry* 125(2):298-305.

88. Szymanski J & Weiss M (2009) Elucidating the origin of anomalous diffusion in crowded fluids. *Phys Rev Lett* 103(3):038102.

89. Regner BM, Vučinić D, Domnisoru C, Bartol TM, Hetzer MW, Tartakovsky DM, & Sejnowski TJ (2013) Anomalous diffusion of single particles in cytoplasm. *Biophysical journal* 104(8):1652-1660.

90. Weiss M (2013) Single-particle tracking data reveal anticorrelated fractional Brownian motion in crowded fluids. *Phys Rev E* 88(1):010101.

91. Platani M, Goldberg I, Lamond AI, & Swedlow JR (2002) Cajal body dynamics and association with chromatin are ATP-dependent. *Nature cell biology* 4(7):502-508.

92. Stiehl O, Weidner-Hertrampf K, & Weiss M (2013) Kinetics of conformational fluctuations in DNA hairpin-loops in crowded fluids. *New Journal of Physics* 15(11):113010.

93. Kojima M, Kubo K, & Yoshikawa K (2006) Elongation/compaction of giant DNA caused by depletion interaction with a flexible polymer. *The Journal of chemical physics* 124(2):024902.

94. Biswas N, Ichikawa M, Datta A, Sato YT, Yanagisawa M, & Yoshikawa K (2012) Phase separation in crowded micro-spheroids: DNA–PEG system. *Chem Phys Lett* 539:157-162.

95. Zhang C, Shao PG, van Kan JA, & van der Maarel JR (2009) Macromolecular crowding induced elongation and compaction of single DNA molecules confined in a nanochannel. *Proceedings of the National Academy of Sciences* 106(39):16651-16656.

96. Efron B & Tibshirani R (1990) *Statistical data analysis in the computer age* (University of Toronto, Department of Statistics).

97. Chapman CD, Lee K, Henze D, Smith DE, & Robertson-Anderson RM (2014) Onset of Non-Continuum Effects in Microrheology of Entangled Polymer Solutions. *Macromolecules* 47(3):1181-1186.

98. Chapman CD & Robertson-Anderson RM (2014) Nonlinear Microrheology Reveals Entanglement-Driven Molecular-Level Viscoelasticity of Concentrated DNA. *Phys Rev Lett* 113(9):098303.

99. Klages R, Radons G, & Sokolov IM (2008) *Anomalous transport: foundations and applications* (John Wiley & Sons).

100. He Y, Burov S, Metzler R, & Barkai E (2008) Random time-scale invariant diffusion and transport coefficients. *Phys Rev Lett* 101(5):058101.

101. Cherstvy AG & Metzler R (2014) Non-ergodicity, fluctuations, and criticality in heterogeneous diffusion processes. *arXiv preprint arXiv:1404.3356*.

102. Honeycutt J, Thirumalai D, & Klimov D (1989) Polymer chains in porous media. *Journal of Physics A: Mathematical and General* 22(5):L169.

103. Baumgärtner A & Muthukumar M (1987) A trapped polymer chain in random porous media. *The Journal of chemical physics* 87(5):3082-3088.

104. Robertson RM & Smith DE (2007) Strong effects of molecular topology on diffusion of entangled DNA molecules. *Proceedings of the National Academy of Sciences* 104(12):4824-4827.

105. Arkın H & Janke W (2013) Gyration tensor based analysis of the shapes of polymer chains in an attractive spherical cage. *The Journal of chemical physics* 138(5):054904.

106. Phelps C, Lee W, Jose D, von Hippel PH, & Marcus AH (2013) Single-molecule FRET and linear dichroism studies of DNA breathing and helicase binding at replication fork junctions. *Proceedings of the National Academy of Sciences* 110(43):17320-17325.

107. Raghu RC & Schofield J (2012) Simulation of tethered oligomers in nanochannels using multi-particle collision dynamics. *The Journal of chemical physics* 137(1):014901.

108. Hall D & Minton AP (2003) Macromolecular crowding: qualitative and semiquantitative successes, quantitative challenges. *Biochimica et Biophysica Acta (BBA)-Proteins and Proteomics* 1649(2):127-139.

109. Breydo L, Reddy KD, Piai A, Felli IC, Pierattelli R, & Uversky VN (2014) The crowd you're in with: effects of different types of crowding agents on protein aggregation. *Biochimica et Biophysica Acta (BBA)-Proteins and Proteomics* 1844(2):346-357.

110. Goodrich GP, Helfrich MR, Overberg JJ, & Keating CD (2004) Effect of macromolecular crowding on DNA: Au nanoparticle bioconjugate assembly. *Langmuir* 20(23):10246-10251.

111. Christiansen A & Wittung-Stafshede P (2014) Synthetic crowding agent dextran causes excluded volume interactions exclusively to tracer protein apoazurin. *FEBS letters* 588(5):811-814.

112. Wang Y, Sarkar M, Smith AE, Krois AS, & Pielak GJ (2012) Macromolecular crowding and protein stability. *J Am Chem Soc* 134(40):16614-16618.

113. Senske M, Törk L, Born B, Havenith M, Herrmann C, & Ebbinghaus S (2014) Protein Stabilization by Macromolecular Crowding through Enthalpy rather than Entropy. *J Am Chem Soc*.

114. Larson RG (1999) *The structure and rheology of complex fluids* (Oxford University Press, New York) pp xxi, 663 p.

115. Witten TA & Pincus PA (2004) *Structured fluids: polymers, colloids, surfactants* (Oxford University Press on Demand).

116. Zaner KS & Valberg PA (1989) Viscoelasticity of F-actin measured with magnetic microparticles. *The Journal of cell biology* 109(5):2233-2243.

117. Ziemann F, Radler J, & Sackmann E (1994) Local measurements of viscoelastic moduli of entangled actin networks using an oscillating magnetic bead micro-rheometer. *Biophys J* 66(6):2210-2216.

118. Mason TG & Weitz D (1995) Optical measurements of frequency-dependent linear viscoelastic moduli of complex fluids. *Phys Rev Lett* 74(7):1250-1253.

119. Valentine M, Dewalt L, & Ou-Yang H (1996) Forces on a colloidal particle in a polymer solution: a study using optical tweezers. *Journal of Physics: Condensed Matter* 8(47):9477.

120. Gittes F, Schnurr B, Olmsted PD, MacKintosh FC, & Schmidt CF (1997) Microscopic viscoelasticity: Shear moduli of soft materials determined from thermal fluctuations. *Phys Rev Lett* 79(17):3286-3289.

121. Mason TG, Ganesan K, vanZanten JH, Wirtz D, & Kuo SC (1997) Particle tracking microrheology of complex fluids. *Phys Rev Lett* 79(17):3282-3285.

122. MacKintosh F & Schmidt C (1999) Microrheology. *Current opinion in colloid & interface science* 4(4):300-307.

123. Gardel ML, Valentine MT, & Weitz DA (2005) Microrheology. *Microscale diagnostic techniques*, (Springer), pp 1-49.

124. Savin T & Doyle PS (2005) Static and dynamic errors in particle tracking microrheology. *Biophysical journal* 88(1):623-638.

125. Graham RS & McLeish TCB (2008) Emerging applications for models of molecular rheology. *J Non-Newton Fluid* 150(1):11-18.

126. Squires TM & Mason TG (2010) Fluid Mechanics of Microrheology. *Annu Rev Fluid Mech* 42:413-438.

127. Köster S, Lin Y-C, Herrmann H, & Weitz DA (2010) Nanomechanics of vimentin intermediate filament networks. *Soft Matter* 6(9):1910-1914.

128. Kotlarchyk M, Botvinick E, & Putnam A (2010) Characterization of hydrogel microstructure using laser tweezers particle tracking and confocal reflection imaging. *Journal of Physics: Condensed Matter* 22(19):194121.

129. Teixeira RE, Dambal AK, Richter DH, & Shaqfeh ESG (2007) The individualistic dynamics of entangled DNA in solution (vol 40, pg 2461, 2007). *Macromolecules* 40(9):3514-3514.

130. Dasgupta BR, Tee SY, Crocker JC, Frisken BJ, & Weitz DA (2002) Microrheology of polyethylene oxide using diffusing wave spectroscopy and single scattering. *Physical review. E, Statistical, nonlinear, and soft matter physics* 65(5 Pt 1):051505.

131. Kohli I & Mukhopadhyay A (2012) Diffusion of Nanoparticles in Semidilute Polymer Solutions: Effect of Different Length Scales. *Macromolecules* 45(15):6143-6149.

132. van Zanten JH, Amin S, & Abdala AA (2004) Brownian motion of colloidal spheres in aqueous PEO solutions. *Macromolecules* 37(10):3874-3880.

133. Wyart FB & De Gennes P (2000) Viscosity at small scales in polymer melts. *The European Physical Journal E* 1(1):93-97.

134. Cai L-H, Panyukov S, & Rubinstein M (2011) Mobility of nonsticky nanoparticles in polymer liquids. *Macromolecules* 44(19):7853-7863.

135. Yamamoto U & Schweizer KS (2011) Theory of nanoparticle diffusion in unentangled and entangled polymer melts. *The Journal of chemical physics* 135(22):224902-224902-224916.

136. Lu Q & Solomon MJ (2002) Probe size effects on the microrheology of associating polymer solutions. *Phys Rev E* 66(6):061504.

137. Maggs AC (1998) Micro-bead mechanics with actin filaments. *Phys Rev E* 57(2):2091-2094.

138. Xu JY, Palmer A, & Wirtz D (1998) Rheology and microrheology of semiflexible polymer solutions: Actin filament networks. *Macromolecules* 31(19):6486-6492.

139. Schmidt FG, Hinner B, & Sackmann E (2000) Microrheometry underestimates the values of the viscoelastic moduli in measurements on F-actin solutions compared to macrorheometry. *Phys Rev E* 61(5):5646-5653.

140. Gardel ML, Valentine MT, Crocker JC, Bausch AR, & Weitz DA (2003) Microrheology of entangled F-actin solutions. *Phys Rev Lett* 91(15).

141. Liu J, Gardel ML, Kroy K, Frey E, Hoffman BD, Crocker JC, Bausch AR, & Weitz DA (2006) Microrheology probes length scale dependent rheology. *Phys Rev Lett* 96(11).

142. Schnurr B, Gittes F, MacKintosh FC, & Schmidt CF (1997) Determining microscopic viscoelasticity in flexible and semiflexible polymer networks from thermal fluctuations. *Macromolecules* 30(25):7781-7792.

143. McGrath JL, Hartwig JH, & Kuo SC (2000) The mechanics of F-actin microenvironments depend on the chemistry of probing surfaces. *Biophysical Journal* 79(6):3258-3266.

144. Valentine MT, Perlman ZE, Gardel ML, Shin JH, Matsudaira P, Mitchison TJ, & Weitz DA (2004) Colloid surface chemistry critically affects multiple particle tracking measurements of biomaterials. *Biophysical Journal* 86(6):4004-4014.

145. Wong IY, Gardel ML, Reichman DR, Weeks ER, Valentine MT, Bausch AR, & Weitz DA (2004) Anomalous diffusion probes microstructure dynamics of entangled F-actin networks. *Phys Rev Lett* 92(17).

146. Goodman A, Tseng Y, & Wirtz D (2002) Effect of length, topology, and concentration on the microviscosity and microheterogeneity of DNA solutions. *J Mol Biol* 323(2):199-215.

147. Chen DT, Weeks ER, Crocker JC, Islam MF, Verma R, Gruber J, Levine AJ, Lubensky TC, & Yodh AG (2003) Rheological microscopy: Local mechanical properties from microrheology. *Phys Rev Lett* 90(10).

148. Gutsche C, Kremer F, Kruger M, Rauscher M, Weeber R, & Harting J (2008) Colloids dragged through a polymer solution: Experiment, theory, and simulation. *J Chem Phys* 129(8):084902.

149. Zhu XY, Kundukad B, & van der Maarel JRC (2008) Viscoelasticity of entangled lambda-phage DNA solutions. *J Chem Phys* 129(18).

150. Mason TG, Dhople A, & Wirtz D (1998) Linear viscoelastic moduli of concentrated DNA solutions. *Macromolecules* 31(11):3600-3603.

151. Bandyopadhyay R & Sood AK (2002) Rheology of semi-dilute solutions of calf-thymus DNA. *Pramana-J Phys* 58(4):685-694.

152. Levine AJ & Lubensky TC (2001) Response function of a sphere in a viscoelastic two-fluid medium. *Phys Rev E* 63(4).

153. Graessley W & Edwards S (1981) Entanglement interactions in polymers and the chain contour concentration. *Polymer* 22(10):1329-1334.

154. Mason TG & Weitz D (1995) Optical measurements of frequency-dependent linear viscoelastic moduli of complex fluids. *Phys Rev Lett* 74(7):1250.

155. Atakhorrami M, Sulkowska J, Addas K, Koenderink G, Tang J, Levine A, MacKintosh F, & Schmidt C (2006) Correlated fluctuations of microparticles in viscoelastic solutions: quantitative measurement of material properties by microrheology in the presence of optical traps. *Phys Rev E* 73(6):061501.

156. Rich JP, Lammerding J, McKinley GH, & Doyle PS (2011) Nonlinear microrheology of an aging, yield stress fluid using magnetic tweezers. *Soft Matter* 7(21):9933-9943.

157. Tassieri M, Gibson GM, Evans R, Yao AM, Warren R, Padgett MJ, & Cooper JM (2010) Measuring storage and loss moduli using optical tweezers: broadband microrheology. *Phys Rev E* 81(2):026308.

158. Squires TM (2005) Active microrheology in the continuum limit: can the macrorheology be recovered? *arXiv preprint cond-mat/0507551*.

159. Gardel M, Valentine M, Crocker JC, Bausch A, & Weitz D (2003) Microrheology of entangled F-actin solutions. *Phys Rev Lett* 91(15):158302.

160. Rubin BK (2006) The pharmacologic approach to airway clearance: Mucoactive agents. *Paediatr Respir Rev* 7:S215-S219.

161. Cribb JA, Meehan TD, Shah SM, Skinner K, & Superfine R (2010) Cylinders vs. spheres: biofluid shear thinning in driven nanoparticle transport. *Ann Biomed Eng* 38(11):3311-3322.

162. Wilking JN & Mason TG (2008) Optically driven nonlinear microrheology of gelatin. *Phys Rev E* 77(5).

163. Tassieri M, Evans R, Warren RL, Bailey NJ, & Cooper JM (2012) Microrheology with optical tweezers: data analysis. *New Journal of Physics* 14(11):115032.

164. Cribb JA, Vasquez PA, Moore P, Norris S, Shah S, Forest MG, & Superfine R (2013) Nonlinear signatures of entangled polymer solutions in active microbead rheology. *J Rheol (N Y N Y)* 57:1247.

165. Squires TM (2008) Nonlinear microrheology: Bulk stresses versus direct interactions. *Langmuir* 24(4):1147-1159.

166. Squires TM & Brady JF (2005) A simple paradigm for active and nonlinear microrheology. *Phys Fluids* 17(7).

167. Wang B, Guan J, Anthony SM, Bae SC, Schweizer KS, & Granick S (2010) Confining potential when a biopolymer filament reptates. *Phys. Rev. Lett* 104(11):118301.

168. Wang SQ, Wang YY, Cheng SW, Li X, Zhu XY, & Sun H (2013) New Experiments for Improved Theoretical Description of Nonlinear Rheology of Entangled Polymers. *Macromolecules* 46(8):3147-3159.

169. Wang S-Q, Ravindranath S, Wang Y, & Boukany P (2007) New theoretical considerations in polymer rheology: Elastic breakdown of chain entanglement network. *The Journal of chemical physics* 127(6):064903.

170. Sussman DM & Schweizer KS (2012) Microscopic theory of quiescent and deformed topologically entangled rod solutions: General formulation and relaxation after nonlinear step strain. *Macromolecules* 45(7):3270-3284.

171. Sussman DM & Schweizer KS (2013) Entangled Rigid Macromolecules under Continuous Startup Shear Deformation: Consequences of a Microscopically Anharmonic Confining Tube. *Macromolecules* 46(14):5684-5693.

172. Desai PS & Larson RG (2014) Constitutive model that shows extension thickening for entangled solutions and extension thinning for melts. *Journal of Rheology (1978-present)* 58(1):255-279.

173. Graham RS, Likhtman AE, McLeish TC, & Milner ST (2003) Microscopic theory of linear, entangled polymer chains under rapid deformation including chain stretch and convective constraint release. *Journal of Rheology (1978-present)* 47(5):1171-1200.

174. Marrucci G (1996) Dynamics of entanglements: A nonlinear model consistent with the Cox-Merz rule. *J Non-Newton Fluid* 62(2):279-289.

175. Sussman DM & Schweizer KS (2011) Microscopic Theory of the Tube Confinement Potential for Liquids of Topologically Entangled Rigid Macromolecules. *Phys Rev Lett* 107(7):078102.

176. Larson RG (2007) Looking inside the entanglement “tube” using molecular dynamics simulations. *Journal of Polymer Science Part B: Polymer Physics* 45(24):3240-3248.

177. Likhtman AE (2009) Whither tube theory: from believing to measuring. *J Non-Newton Fluid* 157(3):158-161.

178. Baig C, Mavrantzas VG, & Kröger M (2010) Flow effects on melt structure and entanglement network of linear polymers: Results from a nonequilibrium molecular dynamics simulation study of a polyethylene melt in steady shear. *Macromolecules* 43(16):6886-6902.

179. Dambal A, Kushwaha A, & Shaqfeh ES (2009) Slip-link simulations of entangled, finitely extensible, wormlike chains in shear flow. *Macromolecules* 42(18):7168-7183.

180. Boukany PE, Wang S-Q, & Wang X (2009) Universal scaling behavior in startup shear of entangled linear polymer melts. *Journal of Rheology (1978-present)* 53(3):617-629.

181. Lu Y, An L, Wang S-Q, & Wang Z-G (2014) Origin of Stress Overshoot during Startup Shear of Entangled Polymer Melts. *ACS Macro Letters* 3:569-573.

182. Gutsche C, Kremer F, Kruger M, Rauscher M, Weeber R, & Harting J (2008) Colloids dragged through a polymer solution: Experiment, theory, and simulation. *J Chem Phys* 129(8).

183. Wissenburg P, Odijk T, Cirkel P, & Mandel M (1995) Multimolecular aggregation of mononucleosomal DNA in concentrated isotropic solutions. *Macromolecules* 28(7):2315-2328.

184. Semmrich C, Larsen RJ, & Bausch AR (2008) Nonlinear mechanics of entangled F-actin solutions. *Soft Matter* 4(8):1675-1680.

185. Watanabe H (1999) Viscoelasticity and dynamics of entangled polymers. *Progress in Polymer Science* 24(9):1253-1403.

186. Gutsche C, Kremer F, Krüger M, Rauscher M, Weeber R, & Harting J (2008) Colloids dragged through a polymer solution: Experiment, theory, and simulation. *The Journal of chemical physics* 129(8):084902.